

1

CAMPINAS STATE UNIVERSITY

2

DOCTORAL THESIS

3

4 **Search of Z and Higgs boson decaying into $\Upsilon + \gamma$**
5 **in pp collisions at CMS/LHC**

6

7 *Author:*

Felipe Torres da Silva de Araujo

Supervisor:

Dr. José Augusto Chinellato

Co-Supervisor:

Dr. Alberto Franco de Sá Santoro

8

*A thesis submitted in fulfillment of the requirements
for the degree of Doctor of Physics*

9

in the

10

Graduate Program of
"Gleb Wataghin" Institute of Physics

11

12

13

August 22, 2020

14 “Sometimes science is a lot more art than science. A lot of people don’t get that.”

15

Rick Sanchez

16 “Então, que seja doce. Repito todas as manhãs, ao abrir as janelas para deixar entrar o sol ou o
17 cinza dos dias, bem assim, que seja doce. Quando há sol, e esse sol bate na minha cara amassada do
18 sono ou da insônia, contemplando as partículas de poeira soltas no ar, feito um pequeno universo;
19 repito sete vezes para dar sorte: que seja doce que seja doce que seja doce e assim por diante. Mas,
20 se alguém me perguntasse o que deverá ser doce, talvez não saiba responder. Tudo é tão vago como
21 se fosse nada.”

22

Caio Fernando Abreu

23 CAMPINAS STATE UNIVERSITY

24 *Abstract*

25 "Gleb Wataghin" Institute of Physics

26 Doctor of Physics

27 **Search of Z and Higgs boson decaying into $\Upsilon + \gamma$ in pp collisions at CMS/LHC**

28 by Felipe Torres da Silva de Araujo

29 Searches for Standard Model Higgs and Z bosons decaying to a $\Upsilon(1S, 2S, 3S)$ and a photon, with
30 subsequent decay of the $\Upsilon(1S, 2S, 3S)$ to $\mu^+ \mu^-$ are presented. The analyses is performed using
31 data recorded by CMS detector from proton-proton collisions at center-of-mass energy of 13 TeV
32 corresponding to an integrated luminosity of 35.86 fb^{-1} . We put a limit, 95% confidence level, on
33 $H \rightarrow \Upsilon(1S, 2S, 3S) + \gamma$ decay branching fraction at $(6.8, 7.1, 6.0) \times 10^{-4}$ and on $Z \rightarrow \Upsilon(1S, 2S, 3S) +$
34 γ decay branching fraction at $(2.6, 2.3, 1.3) \times 10^{-6}$. Contributions to operation, maintenance and
35 R&D of Resistive Plate Chambers (RPC) of CMS are also presented. **EXPANDIR**

DRAFT

36

Acknowledgements

37 I would like to thank:

- 38 • the Campinas State University for providing the institutional support for this study;
- 39 • the Rio de Janeiro State University for the cooperation with Campinas State University in
40 their high-energy physics program. This was a key factor for this study;
- 41 • the National Council for Scientific and Technological Development (CNPq) for the financial
42 support for this work;
- 43 • the European Laboratory for Particle Physics (CERN) for the construction and operation of
44 the Large Hadron Collider (LHC);
- 45 • the Compact Muon Solenoid (CMS) collaboration for the construction, operation and provi-
46 sion of the instrumental means for this study.

DRAFT

47 Contents

| | | |
|----|--|-----|
| 48 | Abstract | iii |
| 49 | Acknowledgements | v |
| 50 | 1 Introduction | 1 |
| 51 | 2 Standard Model and Rare Z and Higgs decays to quarkonia | 3 |
| 52 | 2.1 Standard Model and Local Gauge Invariance | 3 |
| 53 | 2.2 SM and Higgs results | 5 |
| 54 | 2.3 Rare Z and Higgs decays to quarkonia | 5 |
| 55 | 2.4 Recent results | 11 |
| 56 | 3 Experimental Setup | 13 |
| 57 | 3.1 Tracker | 13 |
| 58 | 3.2 Electromagnetic Calorimeter | 13 |
| 59 | 3.3 Hadronic Calorimeter | 13 |
| 60 | 3.4 Muon System | 14 |
| 61 | 3.4.1 DT | 14 |
| 62 | 3.4.2 CSC | 14 |
| 63 | 3.4.3 RPC | 14 |
| 64 | 3.4.4 GEN | 14 |
| 65 | 3.5 Trigger and Data Acquisition | 14 |
| 66 | 3.6 Simulation, reconstruction and computing | 14 |
| 67 | 3.7 Particle Flow Algorithm | 15 |
| 68 | 4 Physics Analysis | 17 |
| 69 | 4.1 Datasets and simulated events | 17 |
| 70 | 4.1.1 Data samples | 17 |
| 71 | 4.1.2 Simulated datasets | 17 |
| 72 | 4.2 Contribution of the $\Upsilon(nS)$ polarisation | 19 |
| 73 | 4.3 Kinematical studies using MC generator | 20 |
| 74 | 4.4 Event selection | 24 |
| 75 | 4.5 Trigger and physics object selection (Group I) | 24 |
| 76 | 4.5.1 Trigger | 24 |
| 77 | 4.5.2 Muon Identification | 24 |
| 78 | 4.5.3 Photon Identification | 26 |
| 79 | 4.5.4 Kinematical distributions | 26 |
| 80 | 4.6 Kinematical selection (Group II) | 36 |
| 81 | 4.7 Event categorization and yields | 44 |
| 82 | 4.7.1 R9 reweighting | 44 |
| 83 | 4.7.2 Event counting and yields | 44 |
| 84 | 4.8 Background modeling | 46 |
| 85 | 4.9 Signal modeling | 53 |

| | | |
|-----|--|-----------|
| 86 | 4.10 Systematic uncertainties | 59 |
| 87 | 4.10.1 Uncertainties on the predicted yields | 59 |
| 88 | 4.10.2 Uncertainties that affect the signal fits | 60 |
| 89 | 4.11 Modeling Cross checks | 63 |
| 90 | 5 Results and conclusion | 69 |
| 91 | 5.1 The CL_s formalism for upper limits setting at CMS | 69 |
| 92 | 5.2 Branching fraction upper limits | 71 |
| 93 | 6 CMS Resistive Plate Chambers - RPC | 75 |
| 94 | 6.1 Resistive Plate Chambers | 75 |
| 95 | 6.1.1 Principles and operation modes | 75 |
| 96 | 6.2 CMS Resistive Plate Chambers | 77 |
| 97 | 6.2.1 Performance | 79 |
| 98 | 6.3 Contribution to the CMS RPC project | 82 |
| 99 | 6.3.1 RPC Operation - Shifts and Data Certification | 82 |
| 100 | 6.4 RPC Online Software | 83 |
| 101 | 6.4.1 iRPC R&D | 84 |
| 102 | 6.4.2 LS2 and the RPC Standard Maintenance | 90 |
| 103 | HV maintenance | 90 |
| 104 | LV and control maintenance | 91 |
| 105 | Detector commissioning | 92 |
| 106 | Bibliography | 95 |

List of Figures

| | | | |
|-----|-----|---|----|
| 107 | 2.1 | Elementary particles of the Standard Model, with their masses charges and spin. Those particles can be divided in two classes: boson (the interaction/force carriers) and the fermions, which are divided in three generations. Source: [1]. | 4 |
| 111 | 2.2 | SM x-sec!!!! Summary of the cross section measurements of Standard Model processes at CMS. Source: [8]. | 6 |
| 113 | 2.6 | Expandir! Signal strength modifiers for the production, μ^i , and for the decay, μ^f , modes on the left and the right panel, respectively. The thick (thin) black lines report the 1σ (2σ) confidence intervals. The thick blue and red lines report the statistical and systematic components of the 1σ confidence intervals. The assumptions used in this fit are described in the text. Source: [10]. | 9 |
| 118 | 2.8 | Example of leading order diagrams for the indirect (top) and direct (bottom) production mechanisms. In the diagrams, the h can also be understood as a Z boson. | 10 |
| 120 | 2.9 | Expected relative variation of the branching ratio for the $H \rightarrow \Upsilon(nS) + \gamma$ to k_b , where $k_b = g(Hb\bar{b})/g(Hb\bar{b})_{SM}$ is the ratio for the observed and expected Yukawa coupling oh $Hb\bar{b}$. Source: [12] | 11 |
| 123 | 4.1 | Distributions of $\cos\theta$ of $\Upsilon \rightarrow \mu\mu$ and $\gamma^* \rightarrow \mu\mu$ The orange distribution is the $Z \rightarrow \Upsilon(1S, 2S, 3S) + \gamma$ sample before reweighting (Unpolarized); the blue and gray distributions are $Z \rightarrow \Upsilon(1S, 2S, 3S)$ sample after reweighting, for the Transverse and Longitudinal Polarization. | 20 |
| 127 | 4.2 | Generator level distributions of main variables for $Z \rightarrow \Upsilon(1S, 2S, 3S) + \gamma$: Transverse momenta of the leading/trailing p_T muon and the photon, pseudorapidity (η) and ϕ of the muons and the photon, distances ΔR between the two muons and between the muons and the photon. All the distributions shown in the figure are normalized to the unity of area. | 22 |
| 132 | 4.3 | Generator level distributions of main variables for $H \rightarrow \Upsilon(1S, 2S, 3S) + \gamma$: Transverse momenta of the leading/trailing p_T muon and the photon, pseudorapidity (η) and ϕ of the muons and the photon, distances ΔR between the two muons and between the muons and the photon. All the distributions shown in the figure are normalized to the unity of area. | 23 |
| 137 | 4.4 | The p_T muon distributions from data and signal events for Z decaying in $\Upsilon(1S, 2S, 3S) + \gamma$ after Group I of selection cuts, where on left are presenting the trailing muons and on right are the leading muons. The plots are normalized to the unit of area. | 27 |
| 140 | 4.5 | The η muon distributions from data and signal events of Z decaying in $\Upsilon(1S, 2S, 3S) + \gamma$ after Group I of selection cuts, where on left are presenting the trailing muons and on right are the leading muons. The plots are normalized to the unit of area. | 27 |
| 143 | 4.6 | The ϕ muon distributions from data and signal events of Z decaying in $\Upsilon(1S, 2S, 3S) + \gamma$ after Group I of selection cuts, where on left are presenting the trailing muons and on right are the leading muons. The plots are normalized to the unit of area. | 27 |
| 146 | 4.7 | The p_T photon distributions from data and signal events for Z decaying in $\Upsilon(1S, 2S, 3S) + \gamma$ Group I of selection cuts. The plots normalized to the unit of area. | 28 |

| | | | |
|-----|------|---|----|
| 148 | 4.8 | The η photon distributions from data and signal events of Z decaying in $\Upsilon(1S, 2S, 3S) + \gamma$ after Group I of selection cuts. The plot is normalized to the unit of area. | 28 |
| 149 | 4.9 | The ϕ photon distributions from data and signal events of Z decaying in $\Upsilon(1S, 2S, 3S) + \gamma$ after Group I of selection cuts. The plot is normalized to the unit of area. | 28 |
| 150 | 4.10 | The p_T distributions for the reconstructed $\Upsilon(1S, 2S, 3S)$ in the left and for Z in the right from data and signal events for Z decaying in $\Upsilon(1S, 2S, 3S) + \gamma$ after Group I of selection cuts. The plots are normalized to the unit of area. | 29 |
| 151 | 4.11 | The η distributions for $\Upsilon(1S, 2S, 3S)$ in the left and for Z in the right from data and signal events for Z decaying in $\Upsilon(1S, 2S, 3S) + \gamma$ after Group I of selection cuts. The plots are normalized to the unit of area. | 29 |
| 152 | 4.12 | The ϕ distributions for $\Upsilon(1S, 2S, 3S)$ in the left and for Z in the right from data and signal events for Z decaying in $\Upsilon(1S, 2S, 3S) + \gamma$ after Group I of selection cuts. The plots are normalized to the unit of area. | 29 |
| 153 | 4.13 | The ΔR distributions between the photon and the leading muon (left) and the trailing muon (right) for for Z decaying in $\Upsilon(1S, 2S, 3S) + \gamma$ from data and signal events after Group I of selection cuts. The plots are normalized to the unit of area. | 30 |
| 154 | 4.14 | Left: The ΔR distributions between reconstructed dimuon ($\mu\mu$) system and the photon. Right: absolute value of the $\Delta\phi$ between the leading muon and the photon for for Z decaying in $\Upsilon(1S, 2S, 3S) + \gamma$ from data and signal events after Group I of selection cuts. The plots are normalized to the unit of area. | 30 |
| 155 | 4.15 | The ratio for the transverse momentum of the reconstructed Upsilon and the reconstructed Z mass ($p_T^{\mu\mu}/M_{\mu\mu\gamma}$ - left) and the ratio for the transverse energy of the reconstructed Photon and the reconstructed Z mass ($E_T^{\mu\mu}/M_{\mu\mu\gamma}$ - right) distribution for Z decaying in $\Upsilon(1S, 2S, 3S) + \gamma$ from data and signal events after Group I of selection cuts. The plots are normalized to the unit of area. | 30 |
| 156 | 4.16 | The dimuon mass distribution of the reconstructed $\Upsilon(1S, 2S, 3S)$ from data and signal events for Z decaying after Group I of selection cuts. The plot is normalized to the number of events. "Signal" stands for the $Z \rightarrow \Upsilon(1S, 2S, 3S) + \gamma$ sample (scaled by a factor of $\times 100$) and "Background" corresponds to the peaking background ($Z \rightarrow \mu\mu\gamma_{FSR}$) sample (scaled by a factor of x3). | 31 |
| 157 | 4.17 | The p_T muon distributions from data and signal events for Higgs decaying in $\Upsilon(1S, 2S, 3S) + \gamma$ after Group I of selection cuts, where on left are presenting the trailing muons and on right are the leading muons. The plots are normalized to the unit of area. | 31 |
| 158 | 4.18 | The η muon distributions from data and signal events of Higgs decaying in $\Upsilon(1S, 2S, 3S) + \gamma$ after Group I of selection cuts, where on left are presenting the trailing muons and on right are the leading muons. The plots are normalized to the unit of area. | 31 |
| 159 | 4.19 | The ϕ muon distributions from data and signal events of Higgs decaying in $\Upsilon(1S, 2S, 3S) + \gamma$ after Group I of selection cuts, where on left are presenting the trailing muons and on right are the leading muons. The plots are normalized to the unit of area. | 31 |
| 160 | 4.20 | The p_T photon distributions from data and signal events for Higgs decaying in $\Upsilon(1S, 2S, 3S) + \gamma$ Group I of selection cuts. The plot is normalized to the unit of area. | 32 |
| 161 | 4.21 | The η photon distributions from data and signal events of Higgs decaying in $\Upsilon(1S, 2S, 3S) + \gamma$ after Group I of selection cuts. The plot is normalized to the unit of area. | 32 |
| 162 | 4.22 | The ϕ photon distributions from data and signal events of Higgs decaying in $\Upsilon(1S, 2S, 3S) + \gamma$ after Group I of selection cuts. The plot is normalized to the unit of area. | 33 |
| 163 | 4.23 | The p_T distributions for $\Upsilon(1S, 2S, 3S)$ in the left and for Higgs in the right from data and signal events for Higgs decaying in $\Upsilon(1S, 2S, 3S) + \gamma$ after Group I of selection cuts. The plots are normalized to the unit of area. | 33 |

| | | |
|-----|--|----|
| 197 | 4.24 The η distributions for $\Upsilon(1S, 2S, 3S)$ in the left and for Higgs in the right from data and signal events for Higgs decaying in $\Upsilon(1S, 2S, 3S) + \gamma$ after Group I of selection cuts. The plots are normalized to the unit of area. | 33 |
| 198 | | |
| 199 | | |
| 200 | 4.25 The ϕ distributions for $\Upsilon(1S, 2S, 3S)$ in the left and for Higgs in the right from data and signal events for Higgs decaying in $\Upsilon(1S, 2S, 3S) + \gamma$ after Group I of selection cuts. The plots are normalized to the unit of area. | 34 |
| 201 | | |
| 202 | | |
| 203 | 4.26 The ΔR distributions between the photon and the leading muon (left) and the trailing muon (right) for Higgs decaying in $\Upsilon(1S, 2S, 3S) + \gamma$ from data and signal events after Group I of selection cuts. The plots are normalized to the unit of area. | 34 |
| 204 | | |
| 205 | | |
| 206 | 4.27 Left: The ΔR distributions between reconstructed dimuon ($\mu\mu$) system and the photon. Right: absolute value of the $\Delta\phi$ between the leading muon and the photon for for Higgs decaying in $\Upsilon(1S, 2S, 3S) + \gamma$ from data and signal events after Group I of selection cuts. The plots are normalized to the unit of area. | 34 |
| 207 | | |
| 208 | | |
| 209 | | |
| 210 | 4.28 The ratio for the transverse momentum of the reconstructed Upsilon and the reconstructed Higgs mass ($p_T^{\mu\mu}/M_{\mu\mu\gamma}$ - left) and the ratio for the transverse energy of the reconstructed Photon and the reconstructed Higgs mass ($E_T^{\mu\mu}/M_{\mu\mu\gamma}$ - right) distribution for Higgs decaying in $\Upsilon(1S, 2S, 3S) + \gamma$ from data and signal events after Group I of selection cuts. The plots are normalized to the unit of area. | 35 |
| 211 | | |
| 212 | | |
| 213 | | |
| 214 | | |
| 215 | 4.29 The dimuon mass distribution of the reconstructed $\Upsilon(1S, 2S, 3S)$ from data and signal events for Higgs decaying after Group I of selection cuts. This plot is normalized to the expected number of events. The plot is normalized to the number of events. "Signal" stands for the $H \rightarrow \Upsilon(1S, 2S, 3S) + \gamma$ sample (scaled by a factor of $\times 60000$) and "Background" corresponds to the peaking background (Higgs Dalitz Decay) sample (scaled by a factor of $\times 400$). | 35 |
| 216 | | |
| 217 | | |
| 218 | | |
| 219 | | |
| 220 | | |
| 221 | 4.30 The p_T muon distributions from data and signal events for Z decaying in $\Upsilon(1S, 2S, 3S) + \gamma$ after Group I of selection cuts, where on left are presenting the trailing muons and on right are the leading muons. The plots are normalized to the number of events. Signal sample is scaled by a factor of $\times 100$ | 36 |
| 222 | | |
| 223 | | |
| 224 | | |
| 225 | 4.31 The η muon distributions from data and signal events of Z decaying in $\Upsilon(1S, 2S, 3S) + \gamma$ after Group I of selection cuts, where on left are presenting the trailing muons and on right are the leading muons. The plots are normalized to the number of events. Signal sample is scaled by a factor of $\times 100$ | 37 |
| 226 | | |
| 227 | | |
| 228 | | |
| 229 | 4.32 The ϕ muon distributions from data and signal events of Z decaying in $\Upsilon(1S, 2S, 3S) + \gamma$ after Group I of selection cuts, where on left are presenting the trailing muons and on right are the leading muons. The plots are normalized to the number of events. Signal sample is scaled by a factor of $\times 100$ | 37 |
| 230 | | |
| 231 | | |
| 232 | | |
| 233 | 4.33 The p_T photon distributions from data and signal events for Z decaying in $\Upsilon(1S, 2S, 3S) + \gamma$ all (Group I+II) selection cuts. The plot is normalized to the number of events. Signal sample is scaled by a factor of $\times 100$ | 37 |
| 234 | | |
| 235 | | |
| 236 | 4.34 The η photon distributions from data and signal events of Z decaying in $\Upsilon(1S, 2S, 3S) + \gamma$ after all (Group I+II) selection cuts. The plot is normalized to the number of events. Signal sample is scaled by a factor of $\times 100$ | 38 |
| 237 | | |
| 238 | | |
| 239 | 4.35 The ϕ photon distributions from data and signal events of Z decaying in $\Upsilon(1S, 2S, 3S) + \gamma$ after all (Group I+II) selection cuts. The plot is normalized to the number of events. Signal sample is scaled by a factor of $\times 100$ | 38 |
| 240 | | |
| 241 | | |
| 242 | 4.36 The p_T distributions for $\Upsilon(1S, 2S, 3S)$ in the left and for Z in the right from data and signal events for Z decaying in $\Upsilon(1S, 2S, 3S) + \gamma$ after all (Group I+II) selection cuts. The plots are normalized to the number of events. Signal sample is scaled by a factor of $\times 100$ | 38 |
| 243 | | |
| 244 | | |
| 245 | | |

| | | |
|-----|--|----|
| 246 | 4.37 The η distributions for $\Upsilon(1S, 2S, 3S)$ in the left and for Z in the right from data and signal events for Z decaying in $\Upsilon(1S, 2S, 3S) + \gamma$ after all (Group I+II) selection cuts. The plots are normalized to the number of events. Signal sample is scaled by a factor of $\times 100$) | 39 |
| 250 | 4.38 The ϕ distributions for $\Upsilon(1S, 2S, 3S)$ in the left and for Z in the right from data and signal events for Z decaying in $\Upsilon(1S, 2S, 3S) + \gamma$ after all (Group I+II) selection cuts. The plots are normalized to the number of events. Signal sample is scaled by a factor of $\times 100$) | 39 |
| 254 | 4.39 The ΔR distributions between the photon and the leading muon (left) and the trailing muon (right) for $\Upsilon(1S, 2S, 3S)$ from data and signal events for Z decaying after all (Group I+II) selection cuts. The plots are normalized to the number of events. Signal sample is scaled by a factor of $\times 100$) | 39 |
| 258 | 4.40 The ratio for the transverse momentum of the reconstructed Upsilon and the reconstructed Z mass ($p_T^{\mu\mu}/M_{\mu\mu\gamma}$ - left) and the ratio for the transverse energy of the reconstructed Photon and the reconstructed Z mass ($E_T^{\mu\mu}/M_{\mu\mu\gamma}$ - right) distribution for $\Upsilon(1S, 2S, 3S)$ from data and signal events for Z decaying after all (Group I+II) selection cuts. The plots are normalized to the number of events. Signal sample is scaled by a factor of $\times 100$) | 40 |
| 262 | 4.41 The p_T muon distributions from data and signal events for Higgs decaying in $\Upsilon(1S, 2S, 3S) + \gamma$ after Group I of selection cuts, where on left are presenting the trailing muons and on right are the leading muons. The plots are normalized to the number of events. Signal sample is scaled by a factor of $\times 600000$) | 40 |
| 266 | 4.42 The η muon distributions from data and signal events of Higgs decaying in $\Upsilon(1S, 2S, 3S) + \gamma$ after Group I of selection cuts, where on left are presenting the trailing muons and on right are the leading muons. The plots are normalized to the number of events. Signal sample is scaled by a factor of $\times 600000$) | 40 |
| 270 | 4.43 The ϕ muon distributions from data and signal events of Higgs decaying in $\Upsilon(1S, 2S, 3S) + \gamma$ after Group I of selection cuts, where on left are presenting the trailing muons and on right are the leading muons. The plots are normalized to the number of events. Signal sample is scaled by a factor of $\times 600000$) | 41 |
| 274 | 4.44 The p_T photon distributions from data and signal events for Higgs decaying in $\Upsilon(1S, 2S, 3S) + \gamma$ all (Group I+II) selection cuts. The plot is normalized to the number of events. Signal sample is scaled by a factor of $\times 600000$) | 41 |
| 278 | 4.45 The η photon distributions from data and signal events of Higgs decaying in $\Upsilon(1S, 2S, 3S) + \gamma$ after all (Group I+II) selection cuts. The plot is normalized to the number of events. Signal sample is scaled by a factor of $\times 600000$) | 41 |
| 282 | 4.46 The ϕ photon distributions from data and signal events of Higgs decaying in $\Upsilon(1S, 2S, 3S) + \gamma$ after all (Group I+II) selection cuts. The plot is normalized to the number of events. Signal sample is scaled by a factor of c) | 42 |
| 286 | 4.47 The p_T distributions for $\Upsilon(1S, 2S, 3S)$ in the left and for Higgs in the right from data and signal events for Higgs decaying in $\Upsilon(1S, 2S, 3S) + \gamma$ after all (Group I+II) selection cuts. The plots are normalized to the number of events. Signal sample is scaled by a factor of $\times 600000$) | 42 |
| 290 | 4.48 The η distributions for $\Upsilon(1S, 2S, 3S)$ in the left and for Higgs in the right from data and signal events for Higgs decaying in $\Upsilon(1S, 2S, 3S) + \gamma$ after all (Group I+II) selection cuts. The plots are normalized to the number of events. Signal sample is scaled by a factor of $\times 600000$) | 42 |
| 294 | 4.49 The ϕ distributions for $\Upsilon(1S, 2S, 3S)$ in the left and for Higgs in the right from data and signal events for Higgs decaying in $\Upsilon(1S, 2S, 3S) + \gamma$ after all (Group I+II) selection cuts. The plots are normalized to the number of events. Signal sample is scaled by a factor of $\times 600000$) | 43 |
| 298 | | |

| | | |
|-----|---|----|
| 297 | 4.50 The ΔR distributions between the photon and the leading muon (left) and the trailing muon (right) for $\Upsilon(1S, 2S, 3S)$ from data and signal events for Higgs decaying after all (Group I+II) selection cuts. The plots are normalized to the number of events. Signal sample is scaled by a factor of $\times 600000$ | 43 |
| 301 | 4.51 The ratio for the transverse momentum of the reconstructed Upsilon and the reconstructed Higgs mass ($p_T^{\mu\mu}/M_{\mu\mu\gamma}$ - left) and the ratio for the transverse energy of the reconstructed Photon and the reconstructed Higgs mass ($E_T^{\mu\mu}/M_{\mu\mu\gamma}$ - right) distribution for $\Upsilon(1S, 2S, 3S)$ from data and signal events for Higgs decaying after all (Group I+II) selection cuts. The plots are normalized to the number of events. Signal sample is scaled by a factor of $\times 600000$ | 43 |
| 305 | 4.52 Data and MC of the R9 variable, before and after the reweighting. Barrel (left) and Endcap (right). | 44 |
| 309 | 4.53 Peaking background for the $Z \rightarrow \Upsilon(1S, 2S, 3S) + \gamma$ analysis. $\mu\mu$ mass distribution (left) and $\mu\mu\gamma$ invariant mass distribution (right). From top to bottom categories: Inclusive, EB High R9, EB Low R9, EE. | 48 |
| 313 | 4.54 Υ control sample fit with Chebychev 1 st order for the background support and 3 gaussian for the three $\Upsilon(1S, 2S, 3S)$ peaks. | 49 |
| 317 | 4.55 $Z \rightarrow \Upsilon(1S, 2S, 3S) + \gamma$ Background Modeling: $\mu\mu$ distribution. Inclusive (top left); EB High R9 (top right), EB Low R9 (bottom left), EE (bottom right). The pdfs projections are plotted with respect to the overall best choice of the statistica test. | 51 |
| 321 | 4.56 $Z \rightarrow \Upsilon(1S, 2S, 3S) + \gamma$ Background Modeling: $\mu\mu\gamma$ distribution. Inclusive (top left); EB High R9 (top right), EB Low R9 (bottom left), EE (bottom right). The plotted <i>pdfs</i> corresponds to the best choice by the statistical test for each family. The signal region, from 80 GeV to 100 GeV was blinded. | 51 |
| 325 | 4.57 Peaking Background for the $H \rightarrow \Upsilon(1S, 2S, 3S) + \gamma$ analysis. $m_{\mu\mu}$ invariant mass distribution (left) and $m_{\mu\mu\gamma}$ invariant mass distribution (right). | 52 |
| 329 | 4.58 $H \rightarrow \Upsilon(1S, 2S, 3S) + \gamma$ Background Modeling: $m_{\mu\mu}$ distribution. The <i>pdfs</i> projections are plotted with respect to the overall best choice of the statistical test. | 52 |
| 333 | 4.59 $H \rightarrow \Upsilon(1S, 2S, 3S) + \gamma$ Background Modeling: $\mu\mu\gamma$ distribution. The plotted <i>pdfs</i> corresponds to the best choice by the statistical test for each family. The signal region, from 115 GeV to 135 GeV was blinded. | 52 |
| 337 | 4.60 Signal Modeling for the $Z \rightarrow \Upsilon(1S, 2S, 3S) + \gamma$ analysis for Inclusive category. $m_{\mu\mu}$ mass distribution (left) and $m_{\mu\mu\gamma}$ mass distribution (right). From top to bottom: $\Upsilon(1S)$, $\Upsilon(2S)$, $\Upsilon(3S)$ | 54 |
| 341 | 4.61 Signal Modeling for the $Z \rightarrow \Upsilon(1S, 2S, 3S) + \gamma$ analysis for EB High R9 category. $m_{\mu\mu}$ mass distribution (left) and $m_{\mu\mu\gamma}$ mass distribution (right). From top to bottom: $\Upsilon(1S)$, $\Upsilon(2S)$, $\Upsilon(3S)$ | 55 |
| 345 | 4.62 Signal Modeling for the $Z \rightarrow \Upsilon(1S, 2S, 3S) + \gamma$ analysis for EB Low R9 category. $m_{\mu\mu}$ mass distribution (left) and $m_{\mu\mu\gamma}$ mass distribution (right). From top to bottom: $\Upsilon(1S)$, $\Upsilon(2S)$, $\Upsilon(3S)$ | 56 |
| 349 | 4.63 Signal Modeling for the $Z \rightarrow \Upsilon(1S, 2S, 3S) + \gamma$ analysis for EE category. $m_{\mu\mu}$ mass distribution (left) and $m_{\mu\mu\gamma}$ mass distribution (right). From top to bottom: $\Upsilon(1S)$, $\Upsilon(2S)$, $\Upsilon(3S)$ | 57 |
| 353 | 4.64 Signal Modeling for the $H \rightarrow \Upsilon(1S, 2S, 3S) + \gamma$. $m_{\mu\mu}$ mass distribution (left) and $m_{\mu\mu\gamma}$ mass distribution (right). From top to bottom: $\Upsilon(1S)$, $\Upsilon(2S)$, $\Upsilon(3S)$ | 58 |
| 357 | 4.65 Examples of the toy datasets fit ($M_{\mu\mu}$), for the Z decay analysis, after the toy dataset refit, for 1S, 2S and 3S (left to right), with μ_{true} equals to 20, 50, 100, 1000 (top to bottom). The red lines corresponds to the background model (B), the green lines to signal model (S), the blue lines to the total (S+B) and the dots is the toy dataset. | 63 |

| | |
|--|----|
| 346 4.66 Examples of the toy datasets fit ($M_{\mu\mu\gamma}$), for the Z decay analysis, after the toy dataset 347 refit, for 1S, 2S and 3S (left to right), with μ_{true} equals to 20, 50, 100, 1000 (top to 348 bottom). The red lines corresponds to the background model (B), the green lines to 349 signal model (S), the blue lines to the total (S+B) and the dots is the toy dataset. | 64 |
| 350 4.67 Examples of the toy datasets fit ($M_{\mu\mu}$), for the Higgs decay analysis, after the toy dataset 351 refit, for 1S, 2S and 3S (left to right), with μ_{true} equals to 100000, 200000, 352 300000, 1000000 (top to bottom). The red lines corresponds to the background model 353 (B), the green lines to signal model (S), the blue lines to the total (S+B) and the 354 dots is the toy dataset. | 65 |
| 355 4.68 Examples of the toy datasets fit ($M_{\mu\mu\gamma}$), for the Higgs decay analysis, after the toy dataset 356 refit, for 1S, 2S and 3S (left to right), with μ_{true} equals to 100000, 200000, 357 300000, 1000000 (top to bottom). The red lines corresponds to the background model 358 (B), the green lines to signal model (S), the blue lines to the total (S+B) and the 359 dots is the toy dataset. | 66 |
| 360 4.69 Distribution of pulls ($\frac{\mu_{fit} - \mu_{true}}{\sigma_{fit}}$), for the Z decay analysis, after the toy dataset refit, 361 for 1S, 2S and 3S (left to right), with μ_{true} equals to 20, 50, 100, 1000 (top to bottom). | 67 |
| 362 4.70 Distribution of pulls ($\frac{\mu_{fit} - \mu_{true}}{\sigma_{fit}}$), for the Higgs decay analysis, after the toy dataset 363 refit, for 1S, 2S and 3S (left to right), with μ_{true} equals to 100000, 200000, 300000, 364 1000000 (top to bottom). | 68 |
| 365 5.1 Example of $f(\tilde{q}_\mu \mu, \hat{\theta}_\mu^{\text{obs}})$ $f(\tilde{q}_\mu \mu = 0, \hat{\theta}_{\mu=0}^{\text{obs}})$ distributions generated with toy MC. 366 Source: [82]. | 71 |
| 367 5.2 Example of $f(\tilde{q}_\mu \mu, \hat{\theta}_\mu^{\text{obs}})$ $f(\tilde{q}_\mu \mu = 0, \hat{\theta}_{\mu=0}^{\text{obs}})$ distributions generated with toy MC. In 368 the figure, q must be read as \tilde{q} . The green area shows the p_{s+b} defined in 5.7, while 369 the yellow one shows p_b defined in 5.8. Source: [79]. | 72 |
| 370 6.1 The Avalanche production process inside a RPC gap. (Top) The initial process and 371 the secondary electron/ion generation. (Bottom) The overall charge distribution of 372 an Avalanche between the electrodes. Source: [86]. | 76 |
| 373 6.2 Streamer formation process. The distorted electric field around the high positive 374 charge concentration enhances the ionization process, initiating secondary avalanches. 375 Source: [86]. | 77 |
| 376 6.3 RPC chamber on installed on station RE+4 of CMS Endcap. Source: [89]. | 78 |
| 377 6.4 R- ϕ (left) and R-Z (right) projections of the barrel Muon System. | 79 |
| 378 6.5 R-Z projections of the endcap Muon System (positive Z side). This is the same 379 configuration for the 36 ϕ sectors. | 80 |
| 380 6.6 RPC efficiencies (per chamber) over Run2 Integrated Luminosity for Barrel (left) and 381 Endcap (right). Red lines indicates technical stops (TS) while grey ones indicates 382 Year-End-Technical stops (YETS). The drop in the efficiency around 110 pb^{-1} is 383 related to a known operation mistake. Source: [100]. | 81 |
| 384 6.7 RPC cluster size (CLS - per chamber) over Run2 Integrated Luminosity for Barrel 385 (left) and Endcap (right). Red lines indicates technical stops (TS) while grey ones 386 indicates Year-End-Technical stops (YETS). The drop in the cluster size around 110 387 pb^{-1} is related to a known operation mistake. Source: [100]. | 81 |
| 388 6.8 Ohmic current history of W+0, RE+1, RE+4 and RE-4. The blank regions, from 389 time to time, corresponds to technical stops (TS), when the detector is off. Source: [100]. | 82 |
| 390 6.9 (a) Luminosity delivered by the LHC, recorded one by CMS and the certified (vali- 391 dated), from the 22nd of April, 2016 to the 27th of October, 2016. (b) Efficiency of 392 the certification process for each subsystem, from the 22nd of April, 2016 to the 27th 393 of October, 2016. Total CMS efficiency is above 90%. Source: [101] | 83 |
| 394 6.10 Upgrade of the RPC online software. | 84 |

| | | |
|-----|---|----|
| 395 | 6.11 Example of the updated screens, using Trigger Supervisor 5 | 84 |
| 396 | 6.12 η projection of the Muon System subdetectors. In purple, is labeled the iRPCS to | |
| 397 | be installed during the CMS upgrade. | 85 |
| 398 | 6.13 FEB configured 8 channels modes. Group should be understood as wire pad. Left: | |
| 399 | Logical diagram for OR2. Right: Logical diagram for AND2. | 86 |
| 400 | 6.14 FEB configured 2 channels modes. Left: Logical diagram for OR8. Group should be | |
| 401 | understood as wire pad. Right: Logical diagram for OR4AND2. | 87 |
| 402 | 6.15 Left: Setup mounted for commissioning. Two MWPC chamber on the top (chambers | |
| 403 | A and B) and two (chambers C and D) on the bottom with a RPC R&D in the | |
| 404 | middle. Right: Rack with all the services for the operation of these chambers. | 88 |
| 405 | 6.16 Coincidence rate of two chambers with respect to an arbitrary distance between | |
| 406 | the two top planes. Measured in 10 minutes, for 2 logical combinations (OR8 and | |
| 407 | OR4AND2). Applied high voltage: 2.65 kV. Threshold: 7 pC. Active area: readout | |
| 408 | of 160 mm x 160 mm per chamber. | 89 |
| 409 | 6.17 Individual rates (chambers A, B, C and D) and coincidence rates for two chambers | |
| 410 | (A AND B, C AND D), for without γ source (blue), a shielded γ source (orange) and | |
| 411 | an unshielded γ source (green). Source sitting on top of chamber A. Applied high | |
| 412 | voltage: 2.65 kV. Threshold: 7 pC. Active area: readout of 160 mm x 320 mm per | |
| 413 | chamber. Logical combination: AND2 | 89 |
| 414 | 6.18 Left: Proposed adapter the chamber patch panel which make it possible to replace | |
| 415 | a tripolar by a jupiter HV connector. Right: Try out of the proposed HV connector | |
| 416 | replacement. | 91 |
| 417 | 6.19 RPC Front-end board (FEB) used in the barrel chambers. | 92 |
| 418 | 6.20 RPC FEB Commissioning Analyzer. | 93 |

DRAFT

List of Tables

| | | | |
|-----|------|---|----|
| 420 | 2.1 | Relative strength (with respect to the strong force) and effective range of action for the four fundamentals interactions. | 3 |
| 421 | 2.2 | Summary of cross section and branching ratio for $H/Z \rightarrow \Upsilon(1S, 2S, 3S) + \gamma \rightarrow \mu^+ \mu^- + \gamma$ analysis. The effective cross-section will be discussed in section 4.1.2. | 7 |
| 422 | 2.3 | Observed upper limits, by the ATLAS experiment, on the branching fractions for the Higgs and Z decays (last result). Detailed comparisons with the results obtained in this study will be presented in chapter 5. | 12 |
| 423 | 2.4 | Observed upper limits, by CMS, on the branching fractions for the Higgs and Z decays. The number are compatible with the ones obtained by ATLAS. The results presented for different polarization scenarios of the J/Ψ | 12 |
| 430 | 4.1 | Datasets simulated (MC) for 2016 conditions. Assuming that $\sigma(pp \rightarrow H)$, taking into consideration all the simulated Higgs production modes, is 55.13 pb [51] and $\sigma(pp \rightarrow Z \rightarrow \mu\mu)$ is 57094.5 pb, including the next-to-next-to-leading order (NNLO) QCD contributions, and the next-to-leading order (NLO) electroweak corrections from fewz 3.1 [52] calculated using the NLO PDF set NNPDF3.0, with the phase space selection in invariant mass of the dimuon system of $m_{\mu\mu} > 50$ GeV. For the Higgs Dalitz σ , we consider only the gluon fusion contribution ($\sigma_{ggF} = 48.6$ pb) [51]. The Higgs Dalitz Decay BR_{SM} and the $Z \rightarrow \mu\mu\gamma_{FSR}$ were obtained with MCFM 6.6 [53] (as in the CMS search for Higgs Dalitz Decay in at $\sqrt{s} = 8$ TeV [54]) and with MADGRAPH 5 _MC@NLO, respectively. The $BR_{\Upsilon(1S, 2S, 3S) \rightarrow \mu\mu}^{PDG} = (2.48, 1.93, 2.18) \times 10^{-2}$ is quoted from Particle Data Group report (PDG) [2]. The "Effective σ " for the signal samples is $\sigma(pp \rightarrow Z(H)) \times BR_{SM} \times BR_{\Upsilon(nS) \rightarrow \mu\mu}^{PDG}$ | 19 |
| 442 | 4.2 | Summary of the impact of reweighted of polarization contribution using several scenarios. | 20 |
| 443 | 4.3 | Conditions for a muon to pass the strict tracker requirements. | 25 |
| 445 | 4.4 | Number of events for the Z decay, before and after the full selection, per categorization scenarios. | 45 |
| 447 | 4.5 | Number of events for the H decay, before and after the full selection. | 45 |
| 448 | 4.6 | Modeling for each background source and mass component. | 46 |
| 449 | 4.7 | Modeling for each signal source and mass component. | 53 |
| 451 | 4.8 | A summary table of systematic uncertainties in the Z boson decaying in $\Upsilon(1S, 2S, 3S) + \gamma$, affecting the final yields of the MC samples. | 61 |
| 452 | 4.9 | A summary table of systematic uncertainties in the Higgs boson decaying in $\Upsilon(1S, 2S, 3S) + \gamma$, affecting the final yields of the MC samples. | 62 |
| 454 | 4.10 | A summary table of systematic uncertainties in the Z (H) decaying in $\Upsilon(1S, 2S, 3S) + \gamma$, affecting the signal fits. | 62 |
| 456 | 5.1 | Summary table for the limits on branching ratio of $Z \rightarrow \Upsilon(1S, 2S, 3S)\gamma$ and $H \rightarrow \Upsilon(1S, 2S, 3S)\gamma$ decays. | 73 |
| 458 | 5.2 | Summary table for the limits on branching ratio of $Z \rightarrow \Upsilon(1S, 2S, 3S)\gamma$, for the two possible categorization scenarios. | 73 |

DRAFT

460 1 Introduction

- 461 INTRODUÇÃO
- 462 MOTIVAÇÃO PARA A ANÁLISE, RESUMO DO MÉTODO E RESULTADOS.
- 463 USAR UM PAPER DE CMS MUON PERFORMANCE PARA DIZER PORQUE
- 464 TRABALHAR COM DETECTORES DE MUONS

DRAFT

⁴⁶⁵ 2 Standard Model and Rare Z and ⁴⁶⁶ Higgs decays to quarkonia

⁴⁶⁷ 2.1 Standard Model and Local Gauge Invariance

⁴⁶⁸ Physics understands the matter and how it interacts in terms of two components: four fundamental forces and elementary particles. From the weakest to the strongest, the fundamental forces are: gravitational, weak, electromagnetic and strong. All share common characteristics like, being mediated by particles ¹, being relevant within some effective range and have a associate a charge-like quantity (i.e. intrinsic characteristic of the object) that defines whether or not, particles might be subjected to a specific interaction.

⁴⁷⁴ Along with the fundamental interactions, the Standard Model (or simply *SM*) defines every existing matter in the Universe as a set of fundamental quantum objects, with properties that define their interaction. Those objects are said to be fundamental since, in the context of the SM, they are the smallest possible components of matter. We shall refer to them as fundamental particles. There four of those mediating particles (force carriers), gluon (g - for the strong interaction), photon (γ - for the electromagnetic interaction), Z and W (for weak interaction), all of them being vector bosons (spin 1). Besides the interaction mediators, described at Table 2.1, the fundamental particles are divided in two groups (*quarks* and *leptons*), with three generations, each. These are not force carriers, but elementary particles, endowed with charge-like characteristics that allow them to by exchange the vector bosons. Those are the building blocks of Matter in our Universe.

⁴⁸⁴ Figure 2.1 summarizes their properties. Table 2.1 presents the relative strength and effective range, for each one of the four fundamental interactions. The gravitational force is not study subject of the Standard Model.

Table 2.1: Relative strength (with respect to the strong force) and effective range of action for the four fundamentals interactions.

| | Mediator | Relative Strength | Effective Range |
|-----------------|----------------|-------------------|-----------------|
| Gravitational | Graviton | 10^{-41} | ∞ |
| Weak | W and Z bosons | 10^{-16} | 10^{-18} m |
| Electromagnetic | Photon | 10^{-3} | ∞ |
| Strong | gluons | 1 | 10^{-15} m |

⁴⁸⁷ There are six quark, up and down (u and d - first generation), charm and strange (c and s - second generation), top and bottom (t and b - first generation), in increasing invariant mass order of the generations. Since they interact thought all the three fundamental forces of the SM, they are said to possess electrical charge, flavour and color. Their generational counterparts, the leptons, don't interact via strong interaction, that is why they are said to have only flavours and electric

¹There is no evidence of the existence of the Graviton (force carrier associated to the gravitational force), even though, it is theorized by models that wish to comprehend gravity in a quantum perspective.

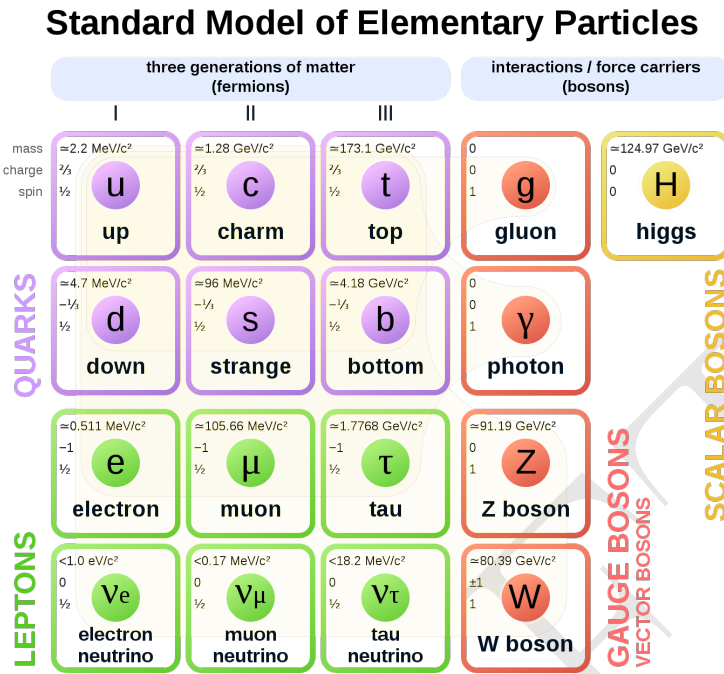


Figure 2.1: Elementary particles of the Standard Model, with their masses charges and spin. Those particles can be divided in two classes: boson (the interaction/force carriers) and the fermions, which are divided in three generations. Source: [1].

492 charge. The leptons are electron and electron neutrino (e and ν_e - first generation), muon and muon
 493 neutrino (μ and ν_μ - second generation) and tau and tau neutrino (τ and ν_τ - third generation).
 494 The neutrinos, within the SM, are massless, even though, experimental measurements have shown
 495 that they actually have mass [2]. Neutrinos are also electrically neutral, meaning that they only
 496 interact through weak interactions.

497 Figure 2.1 also presents the Higgs Boson (H) which is part of the SM and shall be discussed later.
 498 Within the Standard Model, the theoretical basis that describe the fundamental interactions are
 499 derived from a common principle: the local gauge invariance. According to Salam and Ward [3]:

500 "Our basic postulate is that it should be possible to generate strong, weak and electro-
 501 magnetic interaction terms [...], by making local gauge transformations on the kinetic-
 502 energy terms in the free Lagrangian for all particles."

503 Taking the Quantum Electrodynamics (QED) as an example: the quantum field theory that de-
 504 scribes the x

505 The fundamental theories that compose the Standard Model are all derived from a fundamental
 506 principle call

507 The electromagnetic force, in the context of fundamental interactions, is described by a gauge theory
 508 called quantum electrodynamics.

509 **Electroweak**

510 2.2 SM and Higgs results

511 The Standard Model have been proven extremely successful in describing what it is proposed to do.
 512 The discovery of the two highest invariant mass particles of the SM, the top quark [4, 5], by the CDF
 513 and 0 collaboration, at FERMILAB, and the Higgs Boson [6, 7], by CMS and ATLAS, at CERN,
 514 fill the two missing pieces of the SM puzzle, presented at Figure 2.1. In general, SM measurements
 515 presents very good agreement between theory and experiment, even when the Higgs boson is taken
 516 into account, once its mass has been established, the subsequent results tend to be found restricted
 517 within the expectations and constrained by the statistics and experimental sensitivity.

518 In this section, we shall briefly review some of the most relevant SM results from LHC, with special
 519 focus to Z and Higgs boson, subjects of the study.

520 **Higgs**

521 **discovery Production modes Decay modes**

522 **Yukawa coupling**

523 **Higgs results at CMS**

524 2.3 Rare Z and Higgs decays to quarkonia

525 The rare decays of the Higgs boson [6, 7] to a quarkonium state and a photon provide a unique
 526 sensitivity to the magnitude of the Yukawa couplings of the Higgs boson to quarks [12–14]. These
 527 couplings are difficult to access on hadronic collisions through direct decay of Higgs in quark-
 528 antiquark, due to the immense background from QCD [15].

529 Among the channels available to explore Yukawa’s couplings of light quarks [13, 14] are those with
 530 heavy-quarkonia. The rare modes of decay of the Z boson have attracted attention focused on
 531 establishing its sensitivity to New Physics [16], being configured as an alternative environment to
 532 investigate the Yukawa couplings of the Higgs boson.

533 Also, the exclusive rare decays of vector bosons (Z , W) provide a favorable environment for testing
 534 the factorization of QCD, thus allowing an approach in a context where the power of corrections
 535 are definitely under control. The main focus of this kind of analysis are the hadronic radioactive
 536 decays, $Z \rightarrow M\gamma$, where M can be a pseudoscalar or a vector meson ($J/\psi, \phi, \Upsilon_n$).

537 They offer the perfect way to explore some of the leading order properties of the light-cone distri-
 538 bution amplitudes (LCDAs) [17] of several mesons, but they present a difficulty, considering that
 539 in the LHC energy scale the branching ratio of these processes is very small. There are theoretical
 540 predictions [18, 19] that point out a branching ratio for several decay channels in the Standard
 541 Model, as shown in the Table 2.2.

542 Recent studies on exclusive Higgs boson decays [20–22] in final states containing a simple vector
 543 meson and a photon have caused interest in these physics topics. It was proposed to use these decays
 544 as a possible way to explore non-standard Yukawa couplings of the Higgs boson. Such measures are
 545 quite challenging in the LHC environment. The observation of hadronic decays of vector bosons
 546 provides could provide a new frontier for the nature of heavy quarkonia production in hadronic
 547 collisions.

548 Along the same lines, the simple exploration of rare SM decays, even in scenarios where anomalous
 549 couplings are, in principle, ruled out by direct measurements [23], as in the case of this analysis
 550 ($H \rightarrow \Upsilon(nS) + \gamma$), are still important as a stress test of the SM and as reference for future

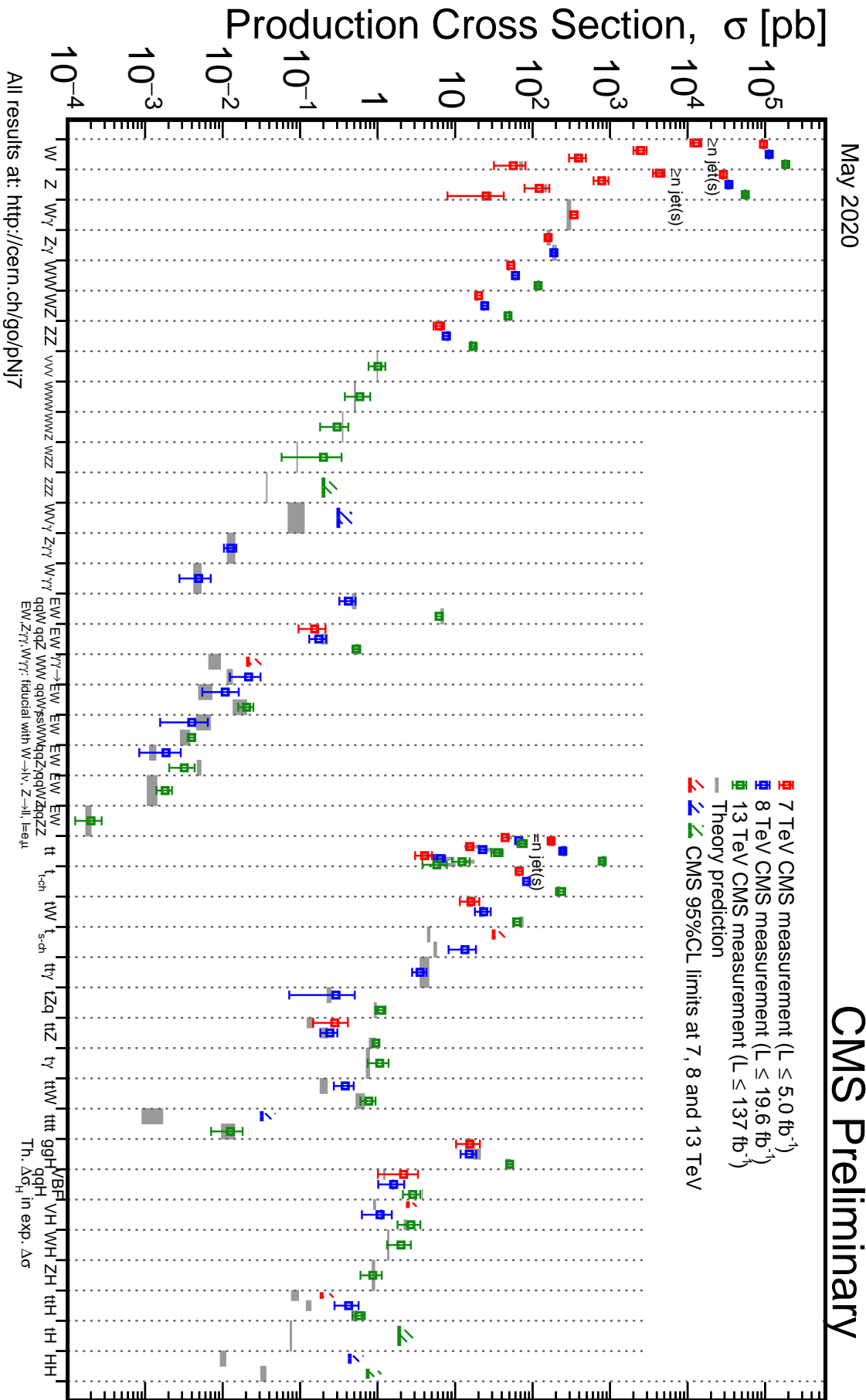
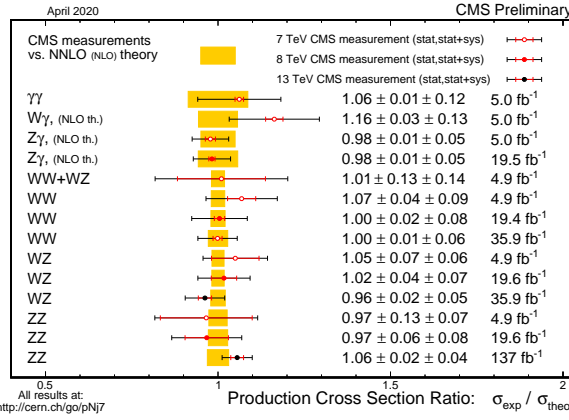
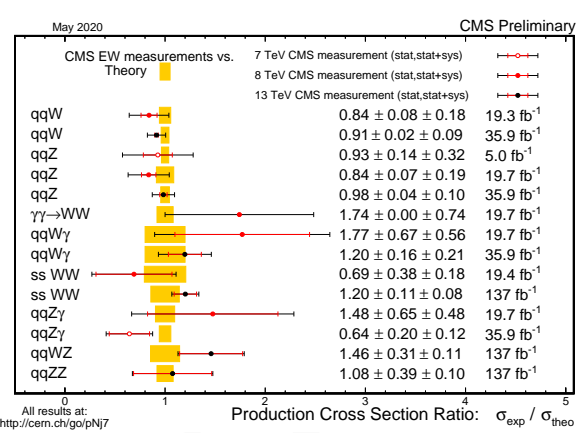


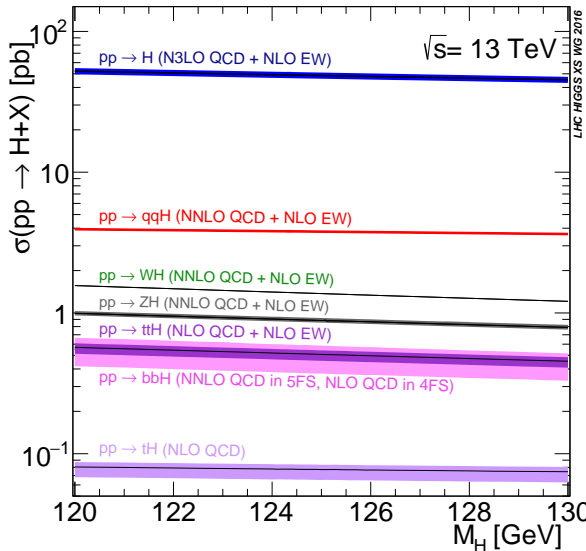
Figure 2.2: **SM x-sec!!!!** Summary of the cross section measurements of Standard Model processes at CMS. Source: [8].



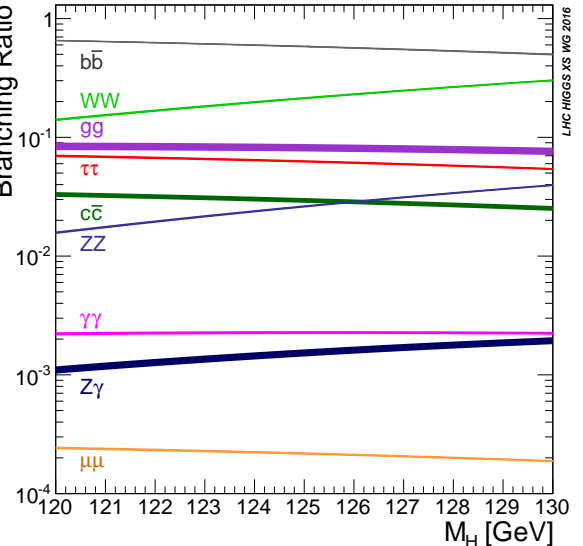
(a) **Exapadir!** Di-boson cross section ratio comparison to theory: Theory predictions updated to latest NNLO calculations where available compared to predictions in the CMS papers and preliminary physics analysis summaries. Source: [8].



(b) **Exapadir!** Summary of the cross sections of pure Electroweak (EWK) interactions among the gauge bosons presented as a ratio compared to theory. Source: [8].



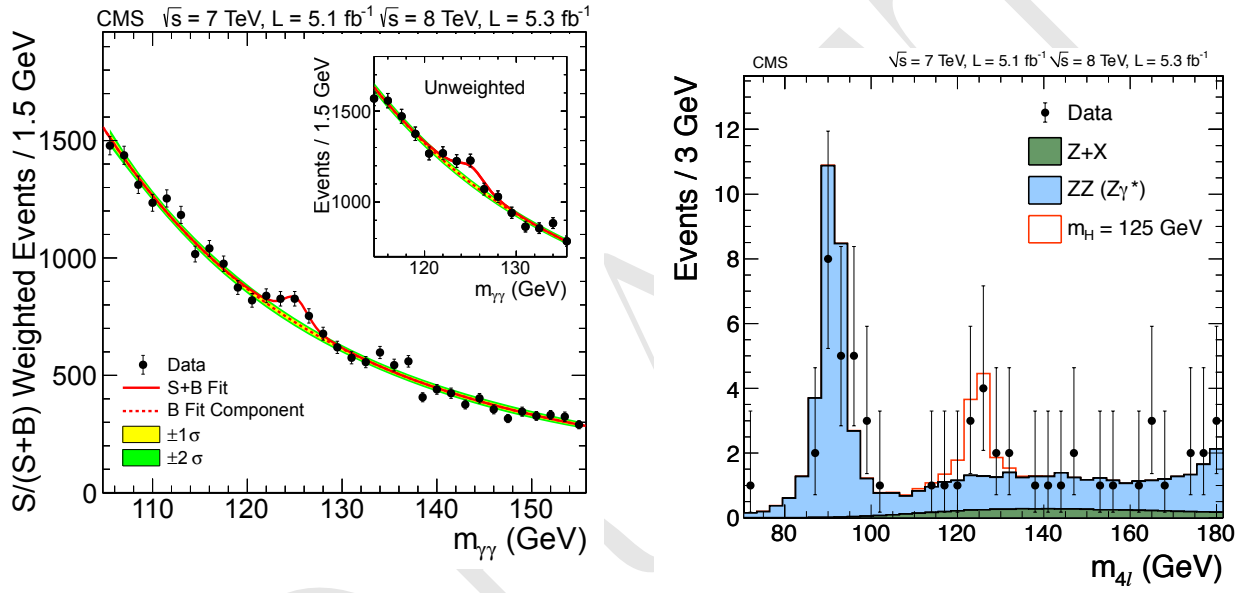
(a) **Exapadir!** Standard Model Higgs boson production cross sections at $\sqrt{s} = 13$ TeV as a function of Higgs boson mass. The tH production cross section accounts for t -channel and s -channel only (no tWH production). Source: [9].



(b) **Exapadir!** Standard Model Higgs boson decay branching ratios for each decays channel. Source: [9].

Table 2.2: Summary of cross section and branching ratio for $H/Z \rightarrow \Upsilon(1S, 2S, 3S) + \gamma \rightarrow \mu^+ \mu^- + \gamma$ analysis. The effective cross-section will be discussed in section 4.1.2.

| Physics Processes | Branching Ratio (BR_{SM}): |
|---------------------------------------|--------------------------------|
| $H \rightarrow \Upsilon(1S) + \gamma$ | 5.22×10^{-9} |
| $H \rightarrow \Upsilon(2S) + \gamma$ | 1.42×10^{-9} |
| $H \rightarrow \Upsilon(3S) + \gamma$ | 9.10×10^{-10} |
| $Z \rightarrow \Upsilon(1S) + \gamma$ | 4.88×10^{-8} |
| $Z \rightarrow \Upsilon(2S) + \gamma$ | 2.44×10^{-8} |
| $Z \rightarrow \Upsilon(3S) + \gamma$ | 1.88×10^{-8} |



(a) **Exapandir!** The diphoton invariant-mass distribution for the 7 and 8 TeV datasets (points), with each event weighted by the predicted $S/(S + B)$ ratio of its event class. The solid and dotted lines give the results of the signal-plus-background and background-only fit, respectively. The light and dark bands represent the ± 1 and ± 2 standard deviation uncertainties respectively on the background estimate. The inset shows the corresponding unweighted invariant-mass distribution around $m_{\gamma\gamma} = 125$ GeV. Source: [6].

(b) **Exapandir!** Distribution of the observed four-lepton invariant mass from the combined 7 and 8 TeV data for the $H \rightarrow ZZ \rightarrow 4\ell$ analysis (points). The prediction for the expected $Z+X$ and $ZZ(Z\gamma^*)$ background are shown by the dark and light histogram, respectively. The open histogram gives the expected distribution for a Higgs boson of mass 125 GeV. Source: [6].

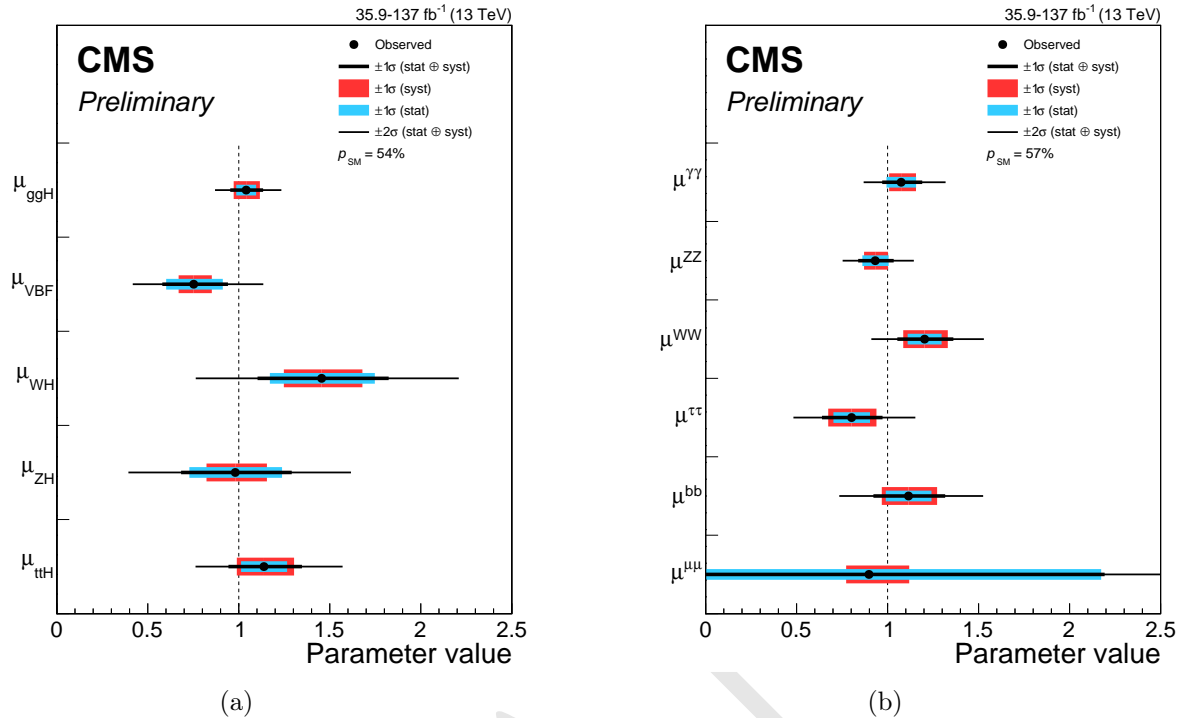


Figure 2.6: **Expandir!** Signal strength modifiers for the production, μ^i , and for the decay, μ^f , modes on the left and the right panel, respectively. The thick (thin) black lines report the 1σ (2σ) confidence intervals. The thick blue and red lines report the statistical and systematic components of the 1σ confidence intervals. The assumptions used in this fit are described in the text. Source: [10].

551 measurements. Specially the later one, when you consider that the small predicted cross sections
 552 from Table 2.2, most probably, would imply that an observation of this decay would be unlikely
 553 even in the HL-LHC [24].

554 This measurement is sensitive to the direct and indirect production (Figure 2.8). The *direct* process
 555 consists in the decay of boson (Higgs or Z) to a quark anti-quark pair, in which, one of the quarks
 556 radiates a photon and the pair hadronizes to a meson (a $\Upsilon(nS)$, for this study), while in *indirect*
 557 process, the decay happens to a $\gamma\gamma^*(Z)$, with the subsequent decay of the $\gamma^*(Z)$ to a quark anti-
 558 quark that hadronizes.

559 Clearly, only the direct process is sensible to the Yukawa coupling of the boson with the quarks,
 560 but, since both processes are indistinguishable in their final state, the in direct process needs to be
 561 taken into account. In this study, a dimuon final state is used to tag the $\Upsilon(nS)$.

562 Even though there is different theoretical predictions for the cross section of this process and its
 563 twin brother ($H \rightarrow J/\Psi + \gamma$), each one taking into account different levels of complexity, the 2013
 564 paper [12], from G. Bodwin, F. Petriello, S. Stoynev and M. Velasco, summarizes very well and in
 565 a simpler manner, the most relevant phenomenological results on these decays. For the decay to
 566 $J/\Psi + \gamma$, the quantum interference with the indirect amplitude, enhances the directed production,
 567 leading to a larger, and potentially observable, cross section. This is not true for the $\Upsilon(nS) + \gamma$
 568 decay, since the interference is destructive, diminishing the cross sections.

569 Another interesting aspect of this study is that, for both $Hc\bar{c}$ and $Hb\bar{b}$ direct coupling measurements
 570 are not sensible to the sign of the Yukawa coupling, while the presence of the indirect process in
 571 the $H \rightarrow M + \gamma$ (M standing for J/Ψ or $\Upsilon(nS)$) decays resolve this ambiguity.

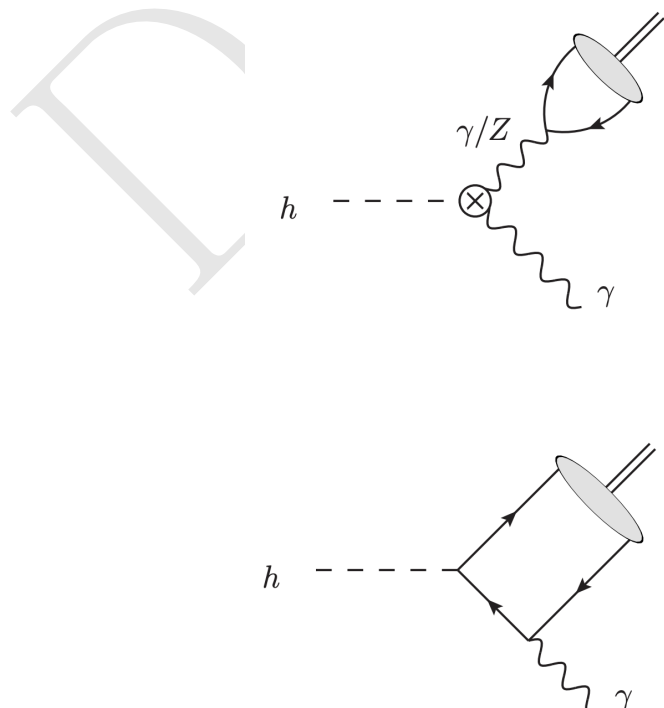
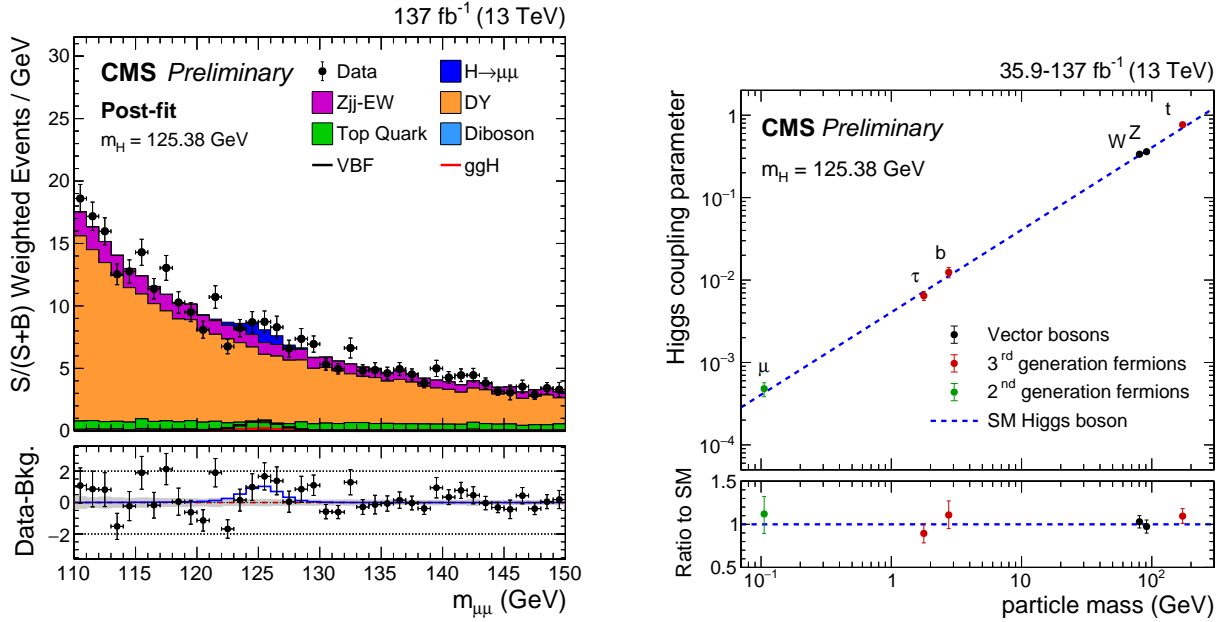


Figure 2.8: Example of leading order diagrams for the indirect (top) and direct (bottom) production mechanisms. In the diagrams, the h can also be understood as a Z boson.

Finally, since the $\Upsilon(nS) + \gamma$ decay has a much smaller cross section, because of the destructive quantum interference between direct and indirect production mechanisms, a small deviation in the $Hb\bar{b}$ Yukawa coupling, can lead a large increase in the expected branching ratio, making this channel sensible any non-Standard Model process that might interfere in this final state. This becomes clear when we look to Figure 2.9.

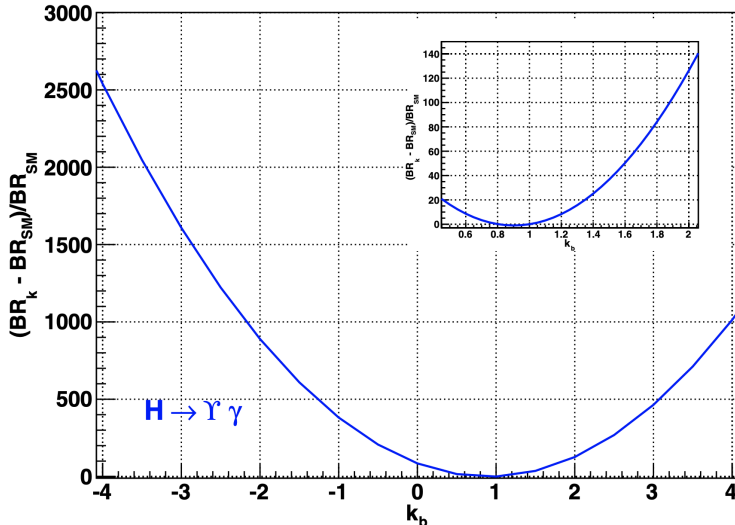


Figure 2.9: Expected relative variation of the branching ratio for the $H \rightarrow \Upsilon(nS) + \gamma$ to k_b , where $k_b = g(Hb\bar{b})/g(Hb\bar{b})_{SM}$ is the ratio for the observed and expected Yukawa coupling oh $Hb\bar{b}$. Source: [12]

2.4 Recent results

The ATLAS experiment [25] already have two results on this decays [26, 27]. The first one corresponds to data taken from 2015, while the former one, corresponds to data from 2016 (the same data taking period to which this study refers).

The what concerns the most updated result, the study corresponded to 36.1 fb^{-1} at $\sqrt{s} = 13 \text{ TeV}$ and no significant excess was found by the experiment. Upper limits for the were obtained, assuming the Standard Model branching fractions predictions, at 95% confidence level, according to table 2.3.

It is worth it to mention that the ATLAS papers present a broader analysis, including the decays to $J/\Psi + \gamma$ and $\Psi(2S) + \gamma$.

CMS [28] also have a result on $J/\Psi + \gamma$ and $\Psi(2S) + \gamma$ decay channel, of the Higgs and Z boson [29]. The observed upper limit on the branching fraction for these decays are presented in table 2.4.

No result on the Z and Higgs decays to $\Upsilon(nS) + \gamma$ have been published by CMS, yet.

The results presented here, are a subset of a broader topic related to the rare decays of Standard Model (SM) boson, involving quarkonia. Sticking only to CMS results, we can cite:

- Search for Higgs and Z boson decays to J/ψ or Υ pairs in proton-proton collisions at $\sqrt{s} = 13 \text{ TeV}$ [30].
- Observation of the $Z \rightarrow \psi\ell^+\ell^-$ decay in pp collisions at $\sqrt{s} = 13 \text{ TeV}$ [31]. This one specifically, is the first observation a such decay, involving a Z boson.
- Search for decays of the 125 GeV Higgs boson into a Z boson and a ρ or ϕ meson [32].

Table 2.3: Observed upper limits, by the ATLAS experiment, on the branching fractions for the Higgs and Z decays (last result). Detailed comparisons with the results obtained in this study will be presented in chapter 5.

| Decay | $\mathcal{B}F$ at 95% CL |
|---------------------------------------|--------------------------|
| $H \rightarrow J/\Psi + \gamma$ | $< 4.5 \times 10^{-4}$ |
| $H \rightarrow \Psi(2S) + \gamma$ | $< 2.0 \times 10^{-3}$ |
| $H \rightarrow \Upsilon(1S) + \gamma$ | $< 4.9 \times 10^{-4}$ |
| $H \rightarrow \Upsilon(2S) + \gamma$ | $< 5.9 \times 10^{-4}$ |
| $H \rightarrow \Upsilon(3S) + \gamma$ | $< 5.7 \times 10^{-4}$ |
| <hr/> | |
| $Z \rightarrow J/\Psi + \gamma$ | $< 2.3 \times 10^{-6}$ |
| $Z \rightarrow \Psi(2S) + \gamma$ | $< 4.5 \times 10^{-6}$ |
| $Z \rightarrow \Upsilon(1S) + \gamma$ | $< 2.8 \times 10^{-6}$ |
| $Z \rightarrow \Upsilon(2S) + \gamma$ | $< 1.7 \times 10^{-6}$ |
| $Z \rightarrow \Upsilon(3S) + \gamma$ | $< 4.8 \times 10^{-6}$ |

Table 2.4: Observed upper limits, by CMS, on the branching fractions for the Higgs and Z decays. The numbers are compatible with the ones obtained by ATLAS. The results presented for different polarization scenarios of the J/Ψ .

| Channel | Polarization | $\mathcal{B}F$ at 95% CL |
|---------------------------------|--------------|--------------------------|
| $Z \rightarrow J/\Psi + \gamma$ | Unpolarized | $< 1.4 \times 10^{-6}$ |
| | Transverse | $< 1.5 \times 10^{-6}$ |
| | Longitudinal | $< 1.2 \times 10^{-6}$ |
| $H \rightarrow J/\Psi + \gamma$ | Transverse | $< 7.6 \times 10^{-4}$ |

597 **verificar resultados se outros foram publicados.**

⁵⁹⁸ 3 Experimental Setup

⁵⁹⁹ The central feature of the CMS apparatus is a superconducting solenoid of 6 m internal diameter,
⁶⁰⁰ providing a magnetic field of 3.8 T. Within the solenoid volume are a silicon pixel and strip tracker,
⁶⁰¹ a lead tungstate crystal electromagnetic calorimeter (ECAL), and a brass and scintillator hadron
⁶⁰² calorimeter (HCAL), each composed of a barrel and two endcap sections. Forward calorimeters ex-
⁶⁰³ tend the pseudorapidity coverage provided by the barrel and endcap detectors. Muons are detected
⁶⁰⁴ in gas-ionization chambers embedded in the steel flux-return yoke outside the solenoid.

⁶⁰⁵ A detailed description of the CMS detector, together with a definition of the coordinate system
⁶⁰⁶ used and the relevant kinematic variables, can be found in [33].

⁶⁰⁷ **falar do sistema de coordenadas e definir η**

⁶⁰⁸ 3.1 Tracker

⁶⁰⁹ **FAZER!**

⁶¹⁰ The silicon tracker measures charged particles within the pseudorapidity range $|\eta| < 2.5$. It consists
⁶¹¹ of 1440 silicon pixel and 15 148 silicon strip detector modules. For non-isolated particles of $1 <$
⁶¹² $p_T < 10 \text{ GeV}$ and $|\eta| < 1.4$, the track resolutions are typically 1.5% in p_T and 25–90 (45–150) μm
⁶¹³ in the transverse (longitudinal) impact parameter [34]

⁶¹⁴ 3.2 Electromagnetic Calorimeter

⁶¹⁵ **FAZER!**

⁶¹⁶ The ECAL consists of 75 848 lead tungstate crystals, which provide coverage in pseudorapidity
⁶¹⁷ $|\eta| < 1.48$ in a barrel region (EB) and $1.48 < |\eta| < 3.0$ in two endcap regions (EE). Preshower
⁶¹⁸ detectors consisting of two planes of silicon sensors interleaved with a total of $3X_0$ of lead are
⁶¹⁹ located in front of each EE detector [35]. In the barrel section of the ECAL, an energy resolution of
⁶²⁰ about 1% is achieved for unconverted or late-converting photons that have energies in the range of
⁶²¹ tens of GeV. The remaining barrel photons have a resolution of about 1.3% up to a pseudorapidity
⁶²² of $|\eta| = 1$, rising to about 2.5% at $|\eta| = 1.4$. In the endcaps, the resolution of unconverted or late-
⁶²³ converting photons is about 2.5%, while the remaining endcap photons have a resolution between
⁶²⁴ 3 and 4% [36]. When combining information from the entire detector, the jet energy resolution
⁶²⁵ amounts typically to 15% at 10 GeV, 8% at 100 GeV, and 4% at 1 TeV, to be compared to about
⁶²⁶ 40%, 12%, and 5% obtained when the ECAL and HCAL calorimeters alone are used.

⁶²⁷ 3.3 Hadronic Calorimeter

⁶²⁸ **FAZER!**

629 3.4 Muon System

630 FAZER!

631 Muons are measured in the pseudorapidity range $|\eta| < 2.4$, with detection planes made using three
632 technologies: drift tubes, cathode strip chambers, and resistive plate chambers. The single muon
633 trigger efficiency exceeds 90% over the full η range, and the efficiency to reconstruct and identify
634 muons is greater than 96%. Matching muons to tracks measured in the silicon tracker results in
635 a relative transverse momentum resolution, for muons with p_T up to 100 GeV, of 1% in the barrel
636 and 3% in the endcaps. The p_T resolution in the barrel is better than 7% for muons with p_T up to
637 1 TeV [37].

638 3.4.1 DT

639 FAZER!

640 3.4.2 CSC

641 FAZER!

642 3.4.3 RPC

643 Due to the particularities of the study, especially the contributions given to the RPC project of
644 CMS, chapter 6 is devoted exclusively to this sub-detector.

645 3.4.4 GEN

646 FAZER!

647 3.5 Trigger and Data Acquisition

648 FAZER!

649 A two-tiered trigger system [38]. The first level (L1), composed of custom hardware processors, uses
650 information from the calorimeters and muon detectors to select events at a rate of around 100 kHz
651 within a time interval of less than $4\ \mu\text{s}$. The second level, known as the high-level trigger (HLT),
652 consists of a farm of processors running a version of the full event reconstruction software optimized
653 for fast processing, and reduces the event rate to around 1 kHz before data storage.

654 3.6 Simulation, reconstruction and computing

655 FAZER!

656 **3.7 Particle Flow Algorithm**

657 **FAZER!**

DRAFT

DRAFT

658 4 Physics Analysis

659 **DEFINIR A ANALISE**

660 **EXPLICAR O PROCESSO E EXEMPLOS DE GRAFICO**

661 **EXPLICAR A ESTRATEGIA**

662 4.1 Datasets and simulated events

663 4.1.1 Data samples

664 The data sample used in this analysis consists of the 2016 13 TeV run with 25 ns bunch separation
 665 recorded by CMS. This data sample is composed only by events that were certified from all CMS
 666 subsystems and reconstruction specialist as good for physics analysis.

667 This data sample corresponds to 35.86 fb^{-1} of integrated luminosity [39].

668 4.1.2 Simulated datasets

669 Data simulation at CMS is done by the use of Monte Carlo (from here on, simply called MC)
 670 simulations generates pseudo-random events, constrained by the physics of the related process to
 671 which we are interested, including the effect of the produced particles interacting with the detector.
 672 The simulation starts with the **hard-scattering** process, at parton (constituents of the proton)
 673 level, done usually, by matrix element generators, which impose to the incoming and outgoing
 674 partons, the dynamics of the simulated process, according to some pre-defined theoretical model.
 675 Along the hard interaction simulation, the **fragmentation** process takes place. Since the the matrix
 676 element generator provide information on the parton level, it is necessary to extract the momentum
 677 distribution of the parton as a function of the Q^2 (transferred momentum) of the process. To do
 678 so, MC generators use the PDFs (parton distribution functions) to sample those values, accordingly.
 679 The matrix element formalism also allows the simulation of the process, taking into account, different
 680 orders of perturbations, like NLO (next-to-leading-order), NNLO (next-to-next-to-leading-order),
 681 and so on.

682 After the hard-scattering, the **showering** process simulates the radiation emission by gluons and
 683 quarks in the initial and final states. Along the hard interaction, the other proton constituents
 684 may also interact through soft interaction. This part of the simulation is called **multiple parton**
 685 **interaction** (MPI). The last components of the simulation is the **hadronization** and the **decay**
 686 **of heavy hadrons and leptons**. The former one, imposes the QCD confinement to low energy
 687 quarks and gluons ¹, while the latter one, implements specific models to decays heavy hadrons and
 688 leptons, like B hadrons and taus.

¹QCD forbids coloured objects to exist in non-asymptotic states. They must decays to more complex systems, until they form stable colorless states.

689 Usually, different generators are used to simulate a process. Each specialized in one or more steps.

690 A summary of the signal and background MC samples used is presented in Table 4.1. These
 691 simulated data are comparable with the proton-proton collision using 2016 data conditions and the
 692 **pileup**² events are added to the simulated event in this step. The pileup events distribution used is
 693 modeled as a Poisson pdf (probability distribution function) with mean of 23 events, as recommended
 694 by CMS. Detector response in the MC samples is simulated using a detailed description of the CMS
 695 detector, based on GEANT4 [40].

696 The signal MC samples are simulated for the Higgs bosons decaying to $\Upsilon(nS)(\rightarrow \mu\mu) + \gamma$ channels
 697 with POWHEG v2.0 [41–43], at next-to-leading order (NLO) of Feynman graphs computation, for
 698 the following production modes: gluon-gluon fusion (ggF), vector boson fusion (VBF), associated
 699 production (VH) and associated top production (ttH), with cross-section summarized at table 4.1.
 700 A extensive review of these production modes can be found at [44]. The PYTHIA 8 generator [45,
 701 46] is used for hadronization and fragmentation with underlying event tune CUETP8M1 [47]. The
 702 parton distribution functions (pdf) NNPDF3.0 [48] are used.

703 For Z decaying to $\Upsilon(nS)(\rightarrow \mu\mu) + \gamma$ channels, the signal samples are simulated with MADGRAPH 5
 704 _MC@NLO 2.6.0 matrix element generator [49] at next leading order and the PYTHIA 8 generator [45,
 705 46] for hadronization and fragmentation with underlying event tune CUETP8M1 [47].

706 The Drell-Yan process, $pp \rightarrow Z \rightarrow \mu\mu\gamma_{FSR}$, results in the same final state as the signal. This
 707 process exhibits a peak in the three-body invariant mass, $m_{\mu\mu\gamma}$, at the Z boson mass, m_Z , and it is
 708 a resonant background for this channel, therefore referred to as a Peaking Background.

709 It is taken into account when deriving the upper limit on the branching fraction for $Z \rightarrow \Upsilon(nS) +$
 710 $\gamma \rightarrow \mu\mu + \gamma$. The MADGRAPH 5 _MC@NLO 2.6.0 matrix element generator [49] at leading order,
 711 interfaced with PYTHIA 8.226 for parton showering and hadronization with tune CUETP8M1 [47],
 712 is used to generate a sample of these resonant background events. The photons in these events are
 713 all produced as final-state radiation from the $Z \rightarrow \mu\mu$ decay and therefore the $m_{\mu\mu\gamma}$ distribution
 714 peaks at the Z boson mass and there is no continuum contribution.

715 Similarly, the Higgs boson Dalitz decay [50], $H \rightarrow \gamma^*\gamma \rightarrow \mu\mu + \gamma$, is a Peaking Background
 716 (resonant) to $H \rightarrow \Upsilon(nS) \rightarrow \mu\mu + \gamma$. It is simulated at NLO with MADGRAPH 5 _MC@NLO
 717 2.6.0 matrix element generator [49] at next-to-leading order and the PYTHIA 8 generator [45, 46] for
 718 hadronization and fragmentation with underlying event tune CUETP8M1 [47]. This Higgs Dalitz
 719 Decay sample, was generated only for the ggF production mode, but its cross-section was rescaled
 720 to the full Higgs cross-section. This process will present a small contribuition of selected events, so
 721 this approximation should be sufficient for the Higgs Peaking Background modeling.

722 There are also background processes that do not give resonance peaks in the three-body invariant
 723 mass spectrum. They are modeled from data, as it will be explained latter in more details.

724 The number of simulated events is is rescaled by the Effective σ , from table 4.1, in order to match
 725 $35.86 fb^{-1}$ of integrated luminosity, from the recorded data. Being $N = \sigma\mathcal{L}$, N in the number of

²Each LHC collision recorded by CMS, is composed not by a single pp interaction, but by a bunch of protons crossing. In this case, a hard interaction is actually surrounded by many soft interaction between adjacent protons. The extra activity produced in these interactions, and caught by the detector, is called **pileup** and has its signal mixed with the hard one. Since, during the data taking, the number of pileup interactions varies according to the instantaneous luminosity, the MC are mixed some soft interaction only sample, called Minimum Bias. The number of mixed soft interaction (pileup events) is governed by a Poisson distribution with a pre-defined mean. The MC samples are then reweighted to match the same distribution of primary vertexes for the corresponding Data. Systematics related to this procedure will be discussed later.

Table 4.1: Datasets simulated (MC) for 2016 conditions. Assuming that $\sigma(pp \rightarrow H)$, taking into consideration all the simulated Higgs production modes, is 55.13 pb [51] and $\sigma(pp \rightarrow Z \rightarrow \mu\mu)$ is 57094.5 pb , including the next-to-next-to-leading order (NNLO) QCD contributions, and the next-to-leading order (NLO) electroweak corrections from fewz 3.1 [52] calculated using the NLO PDF set NNPDF3.0, with the phase space selection in invariant mass of the dimuon system of $m_{\mu\mu} > 50 \text{ GeV}$. For the Higgs Dalitz σ , we consider only the gluon fusion contribution ($\sigma_{ggF} = 48.6 \text{ pb}$) [51]. The Higgs Dalitz Decay BR_{SM} and the $Z \rightarrow \mu\mu\gamma_{FSR}$ were obtained with MCFM 6.6 [53] (as in the CMS search for Higgs Dalitz Decay in at $\sqrt{s} = 8 \text{ TeV}$ [54]) and with MADGRAPH 5 _MC@NLO, respectively. The $BR_{\Upsilon(1S,2S,3S) \rightarrow \mu\mu}^{PDG} = (2.48, 1.93, 2.18) \times 10^{-2}$ is quoted from Particle Data Group report (PDG) [2]. The "Effective σ " for the signal samples is $\sigma(pp \rightarrow Z(H)) \times BR_{SM} \times BR_{\Upsilon(nS) \rightarrow \mu\mu}^{PDG}$.

| Physics Processes | Branching Ratio (BR_{SM}) | Effective σ (in pb) | Generator | Sample Type |
|---------------------------------------|-------------------------------|----------------------------|------------|--------------------|
| $H \rightarrow \Upsilon(1S) + \gamma$ | 5.22×10^{-9} | 7.14×10^{-9} | POWHEG 2.0 | Signal |
| $H \rightarrow \Upsilon(2S) + \gamma$ | 1.42×10^{-9} | 1.51×10^{-9} | POWHEG 2.0 | Signal |
| $H \rightarrow \Upsilon(3S) + \gamma$ | 9.10×10^{-10} | 1.10×10^{-9} | POWHEG 2.0 | Signal |
| $Z \rightarrow \Upsilon(1S) + \gamma$ | 4.88×10^{-8} | 6.80×10^{-5} | MADGRAPH 5 | Signal |
| $Z \rightarrow \Upsilon(2S) + \gamma$ | 2.44×10^{-8} | 2.69×10^{-5} | MADGRAPH 5 | Signal |
| $Z \rightarrow \Upsilon(3S) + \gamma$ | 1.88×10^{-8} | 2.34×10^{-5} | MADGRAPH 5 | Signal |
| H Dalitz Decay | 3.83×10^{-5} | 2.13×10^{-3} | MADGRAPH 5 | Peaking Background |
| $Z \rightarrow \mu\mu\gamma_{FSR}$ | — | 7.93×10^{-2} | MADGRAPH 5 | Peaking Background |

726 events for a process, σ is the cross-section and \mathcal{L} is the integrated luminosity, the reweighting factor,
727 for a simulated sample is:

$$w_{MC} = \frac{\sigma \mathcal{L}}{N_{sim}}, \quad (4.1)$$

728 where N_{sim} is the number of simulated events for a specific process.

729 The simulated sample are also corrected by the data pile-up distribution, since the pileup distribu-
730 tion of MC is different from the pileup distribution of data. The way to correct the MC is to assign
731 a weight to each bin of the MC pileup distribution, with respect to the data. The rescaling is defined
732 as the ratio between normalized Pile-up (PU) distribution for Data and MC.

$$w_{PU}(n) = \frac{P_{PU}^{Data}(n)}{P_{PU}^{Sim}(n)}, \quad (4.2)$$

733 where n is the number of interaction per bunch crossing (pile-up).

734 4.2 Contribution of the $\Upsilon(nS)$ polarisation

735 Measurements of quarkonium polarization observables may yield information about quarkonium
736 production mechanisms that are not available from the study of unpolarized cross sections alone.
737 The three polarization states of a $J = 1$ quarkonium can be specified in terms of a particular
738 coordinate system in the rest frame of the quarkonium. This coordinate system is often called the
739 "spin-quantization frame".

740 In a hadron collider, $\Upsilon(1S, 2S, 3S)$ are reconstructed through their electromagnetic decays into a
741 lepton pair. The information about the polarization of the quarkonium state is encoded in the

angular distribution of the leptons. This angular distribution is usually described in the quarkonium rest frame with respect to a particular spin-quantization frame [55]. The polarization of the $\Upsilon(1S, 2S, 3S)$ is not simulated for signal MC sample and we only apply a reweighting scale factor to each event and so we can emulate the polarization effects [56]. Figure 4.1 present the distributions of $\cos \Theta$ of $\Upsilon \rightarrow \mu\mu$, where Θ is the angle between the positive muon and the Υ in the Z (Higgs) rest-frame. At Table 4.2 we show the the analytical functions used to describe the extremes scenarios (Unpolarized, Transverse Polarization and Longitudinal Polarization) reweighting, presented in this analysis.

It is worth stating that, for the Higgs decay, on the Transverse Polarization is considered. For the Z decay, because of its spin nature, the Unpolarized scenario is used as the nominal one, and the effects of the two other extremes (Transverse Polarization and Longitudinal Polarization) are quoted as systematics.

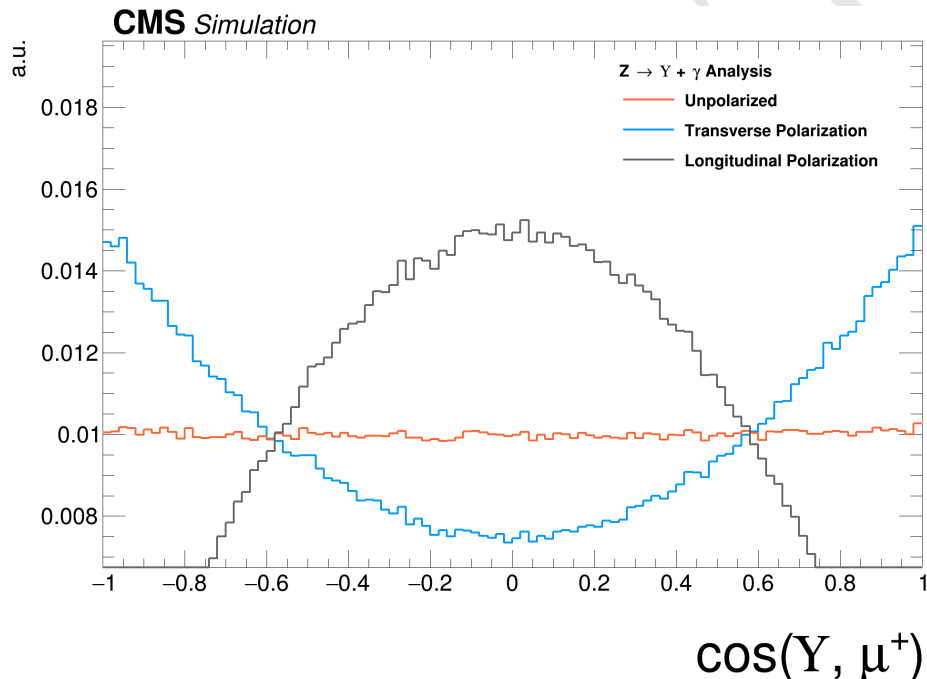


Figure 4.1: Distributions of $\cos \theta$ of $\Upsilon \rightarrow \mu\mu$ and $\gamma^* \rightarrow \mu\mu$. The orange distribution is the $Z \rightarrow \Upsilon(1S, 2S, 3S) + \gamma$ sample before reweighting (Unpolarized); the blue and gray distributions are $Z \rightarrow \Upsilon(1S, 2S, 3S)$ sample after reweighting, for the Transverse and Longitudinal Polarization.

Table 4.2: Summary of the impact of reweighted of polarization contribution using several scenarios.

| J_Z | Polarisation Scenario | Analytic Description |
|---------|-----------------------|------------------------------------|
| ± 1 | Transverse | $3/4 \times (1 + (\cos \Theta)^2)$ |
| 0 | Longitudinal | $3/2 \times (1 - (\cos \Theta)^2)$ |

4.3 Kinematical studies using MC generator

Using the PYTHIA 8.226 generator, the Monte Carlo signals are produced for Higgs (Z) boson events decaying in ($\Upsilon(1S, 2S, 3S)$) + γ , which are highly boosted. Observing the kinematic generator level distributions in Figure 4.2 for Z boson and Figure 4.3 for Higgs boson, we could conclude that the high- E_T (transverse energy, with respect to the beam line) photon will be back-to-back to the Υ particles being possible to apply an isolation selection to identify a photon in this kinematic topology.

760 Also, we can observe those transverse momenta of the leading/trailing p_T (transverse momemtum,
761 with respect to the beam line) muon ³ and the photon and distances $\Delta R = \sqrt{\Delta\eta^2 + \Delta\phi^2}$ between
762 the two muons and between the muons and the photon are a good variable that can be used to
763 discriminate the contribution between signal and background events. The leading muon transverse
764 momentum can be greater than 45(30) GeV and trailing muon is greater than 10(20) GeV in Higgs(Z)
765 decay. ΔR distributions of the two muons and between the muons and the photon in the both cases
766 show that the two muons are very close and the photon is back-to-back in relation of dimuon system.
767 Another feature of this kinematic topology is that the production vertex between muons produced
768 in Υ decaying events and the high- E_T photon is very well defined.

DRAFT

³In this study we define leading muon and the muon, decaying from the Υ , with highest p_T . Trailing muon is the one with the second hight p_T .

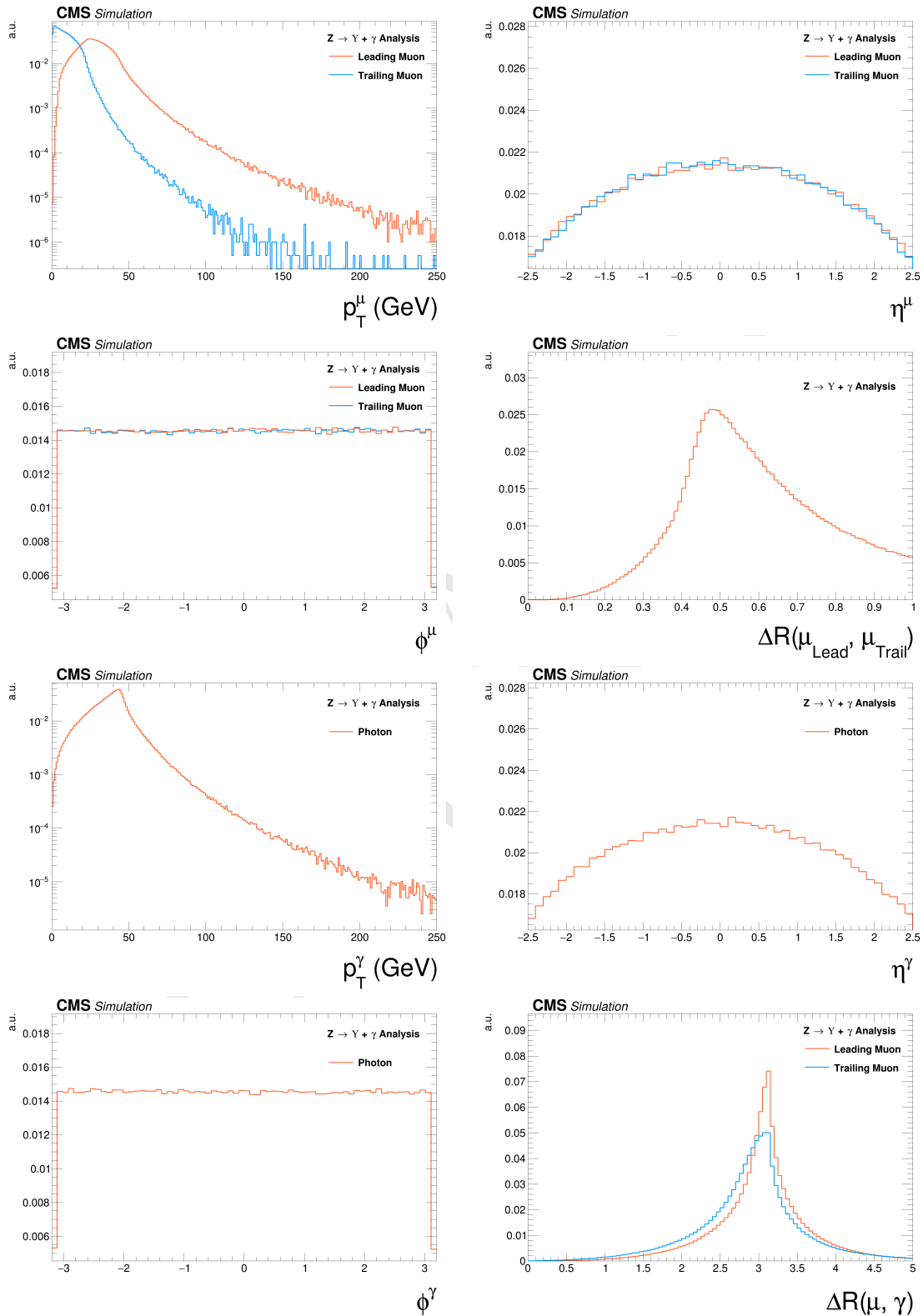


Figure 4.2: Generator level distributions of main variables for $Z \rightarrow \Upsilon(1S, 2S, 3S) + \gamma$: Transverse momenta of the leading/trailing p_T muon and the photon, pseudorapidity (η) and ϕ of the muons and the photon, distances ΔR between the two muons and between the muons and the photon. All the distributions shown in the figure are normalized to the unity of area.

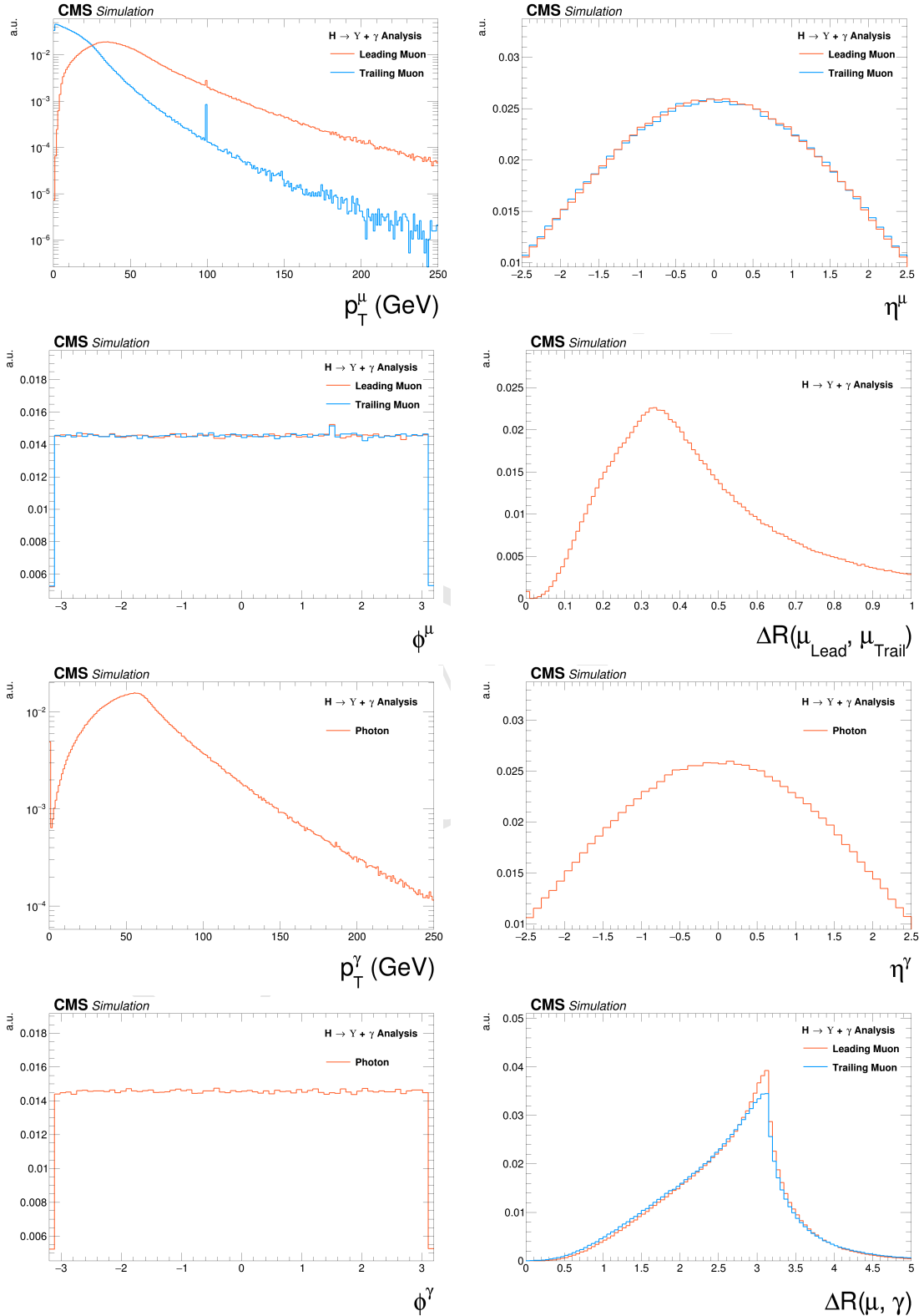


Figure 4.3: Generator level distributions of main variables for $H \rightarrow \Upsilon(1S, 2S, 3S) + \gamma$: Transverse momenta of the leading/trailing p_T muon and the photon, pseudorapidity (η) and ϕ of the muons and the photon, distances ΔR between the two muons and between the muons and the photon. All the distributions shown in the figure are normalized to the unity of area.

769 4.4 Event selection

770 The event selection is divided in two steps. At first, a set of cuts related to trigger and physics object
 771 (muons and photons) selection is applied. High level physics objects at CMS are reconstructed based
 772 of the Particle Flow (PF) algorithm [57]. This selection is called, within this analysis, Group I.

773 For the events that pass the Group I selection, another set of cuts is applied, this time focusing on
 774 kinematical (phase space) event selection, in order to enhance the signal to background ratio. This
 775 later set is called, within this analysis, Group II. After full selection, three exclusive categories are
 776 defined, based on the photon's η region and its energy spread shape within the ECAL cells (R9).

777 After the full selection, a background and signal modeling process is applied, based on the invariant
 778 mass distributions, which will be explained in the next section.

779 4.5 Trigger and physics object selection (Group I)

780 4.5.1 Trigger

781 In this study, the same trigger requirements are applied to both data and simulated samples. For
 782 the first trigger level (L1), events are selected if they present at least one muon with transverse
 783 momentum greater than 5 GeV and an isolated ⁴ photon or electron with transverse momentum
 784 greater than 18 GeV (at L1, there is no differentiation between photons and electrons). At the
 785 software level of the trigger system (HLT), the events are required to have at least one muon with
 786 transverse momentum greater than 17 GeV and a photon with transverse momentum greater than
 787 30 GeV.

788 In order to compensate any difference in the trigger performance between simulated and data sam-
 789 ples, for every selected MC a proper scale factor is applied, based on the the p_T of the reconstructed
 790 muon and photon. These scale factor computed by the ratio between efficiency of the trigger for
 791 the Data sample over the efficiency for a MC sample. These efficiencies are calculated with the
 792 tag-and-probe method, exploring the the resonance of a final state composted by two muon and
 793 one photon in the vicinity of the Z boson invariant mass. To this final state, a selections was
 794 applied to ensure that the photon comes from a Final State Radiation process, allowing us to use
 795 the tag-and-probe method.

796 Considering the similarity of this analysis with the $H/Z \rightarrow J/\psi + \gamma$ analysis [29], not only in therm
 797 of data samples, but also for triggering and physics object selection, the same scale factors were
 798 applied. More details are given in the same paper.

799 4.5.2 Muon Identification

800 Ahead of any selection, a standard CMS "Ghost Cleaning" procedure is applied to all reconstructed
 801 muons in order to avoid that a single physical muon is reconstructed as two or more. For this
 802 procedure, reconstructed muons sharing 50% or more segments in the system are arbitrated.

803 After the cleaning, a muon is chosen when it passes a a two step identification: the **Loose ID** and
 804 the **Tight ID**. Below the muon identification procedure is summarized .

⁴The concept of isolation will be detailed later, but in summary, it means a object which has very small activity (above a certain threshold of energy/momentum) around it. In hadron-hadron collider, isolation is a characteristics of hard interactions.

805 For the Loose ID, each muon is required to:

- 806 • have transverse momentum greater than 5 GeV, in order to cope with Particle Flow require-
807 ments;
- 808 • be within the muon system acceptance: $|\eta| < 2.4$;
- 809 • to have a three dimensional impact parameter uncertainty smaller than 4;
- 810 • to have transverse distance smaller than 0.5 cm ($d_{xy} < 0.5$), with respect to the primary
811 vertex (PV);
- 812 • to have longitudinal distance greater than 1.0 cm ($d_z < 1$), with respect to the primary vertex
813 (PV).

814 Muons reconstructed only in the muon system, without a correspondence with the tracker, are
815 rejected. The last three requirements of the Loose ID are imposed in order to suppress muons from
816 in-flight decays.

817 The primary vertex itself, is determined as the reconstructed vertex with the biggest sum of p_T^2 in
818 the event. This sum is performed, considering all the charged PF candidates clustered by the jet
819 finding algorithms [58, 59] and the MET, which is defined as the p_T vector sum of all the charged
820 and neutral PF candidates associated to that vertex.

821 For the Tight ID, muons with transverse momentum $p_T < 200$ GeV, are required to have been
822 reconstructed with the Particle Flow (PF) algorithm. If they have $p_T > 200$ GeV, they should re-
823 constructed with the Particle Flow (PF) algorithm or satisfy the strict tracker requirements (defined
824 in table 4.3).

Table 4.3: Conditions for a muon to pass the strict tracker requirements.

| Requirement | Technical definition |
|----------------------------------|--|
| Muon station matching | Muon is matched to segments in at least two stations in the muon system |
| Good p_T measurement | $\frac{p_T}{\sigma_{p_T}} < 0.3$ |
| Vertex compatibility ($x - y$) | $d_{xy} < 2$ mm |
| Vertex compatibility (z) | $d_z < 5$ mm |
| Pixel hits | At least one pixel hit |
| Tracker hits | Hits in at least six tracker layers |

825 To mitigate spurious signal in the detector that would mimic a muon, the leading muon (the one
826 with highest p_T) is required to be isolated within a cone of radius $\Delta R = \sqrt{\Delta\eta^2 + \Delta\phi^2} < 0.3$ in
827 the $\eta - \phi$ plane. The isolation is evaluated in terms of $\mathcal{I}^\mu < 0.35$, defined as:

$$\mathcal{I}^\mu \equiv \left(\sum p_T^{\text{charged}} + \max \left[0, \sum p_T^{\text{neutral}} + \sum p_T^\gamma - p_T^{\text{PU}}(\mu) \right] \right) / p_T^\mu. \quad (4.3)$$

828 The $\sum p_T^{\text{charged}}$ is the scalar sum of the transverse momenta of charged hadrons originating from the
829 chosen primary vertex of the event. The $\sum p_T^{\text{neutral}}$ and $\sum p_T^\gamma$ are the scalar sums of the transverse
830 momenta for neutral hadrons and photons, respectively. Since the isolation variable is particularly
831 sensitive to energy deposits from pileup interactions, a $p_T^{\text{PU}}(\mu)$ contribution is subtracted, where
832 $p_T^{\text{PU}}(\mu) \equiv 0.5 \times \sum_i p_T^{\text{PU},i}$, where i runs over the momenta of the charged hadron PF candidates
833 not originating from the primary vertex, and the factor of 0.5 corrects for the different fraction of
834 charged and neutral particles in the cone.

835 One should keep in mind that this muon identification is the same as the one used by the $H \rightarrow$
 836 $ZZ^* \rightarrow 4l$ [60]. This was done in order to keep in phase with other Higgs analysis inside the
 837 collaboration. After the muon identification, an appropriate scale factor is applied to the MC
 838 events based on the leading muon p_T and η , in order to correct any possible discrepancy between
 839 data and simulated samples. The scale factors were taken from the $H \rightarrow ZZ^* \rightarrow 4l$ analysis.

840 In order to cope with trigger requirements, the leading muon should have $p_T > 20$ GeV and the
 841 trailing muon $p_T > 4$ GeV.

842 4.5.3 Photon Identification

843 For the photon identification and selection, standard CMS . The Multivariate (MVA) Photon iden-
 844 tification is used with a working point of 90%, together with a electron veto procedure, to avoid
 845 misidentification of electrons as photons. Kinematically, the photons are requested to have trans-
 846 verse energy, with respect to the beam line, $E_T > 33$ GeV and reconstructed within the CMS
 847 acceptance for photons $|\eta_{SC}| < 2.5^5$, excluding the Electromagnetic Calorimeter (ECAL) Barrel-
 848 Endcap intersections.

849 The threshold of 33 GeV for the photon transverse energy is driven by the trigger requirements.
 850 The selecte photon, per event, is the one with highest E_T .

851 4.5.4 Kinematical distributions

852 The selection described so far, is called Group I. The plots shown below are related to selected
 853 events after this set.

854 Figures 4.4 to 4.9 presents the p_T , η and ϕ distributions for the leading muon, trailing muon and
 855 the photon, for the Z decaying in $\Upsilon(1S, 2S, 3S) + \gamma$.

856 Figures 4.10 to 4.12 presents the p_T , η and ϕ distributions for reconstructed $\Upsilon(nS)$ ($\mu\mu$ system)
 857 and the reconstructed boson ($\mu\mu\gamma$ system).

858 Figures 4.13 to 4.16 presents the $\Delta R = \sqrt{\Delta\eta^2 + \Delta\phi^2}$ between the photon and the muons, the
 859 ΔR distributions between reconstructed dimuon ($\mu\mu$) system and the photon, the absolute value
 860 of the $\Delta\phi$ between the leading muon and the photon, the ratio for the transverse momentum of
 861 the reconstructed Upsilon and the reconstructed Z mass ($p_T^{\mu\mu}/M_{\mu\mu\gamma}$), the ratio for the transverse
 862 energy of the reconstructed Photon and the reconstructed Z mass ($E_T^{\mu\mu}/M_{\mu\mu\gamma}$) and dimuon mass
 863 distribution of the reconstructed $\Upsilon(nS)$.

864 Figures 4.17 to 4.29 present the same variables, but for the Higgs decaying in $\Upsilon(1S, 2S, 3S) + \gamma$
 865 channel.

⁵SC stands for Super Cluster of the reconstructed photon. It is the set of cell in the Electromagnetic Calorimeter used for the photon observation.

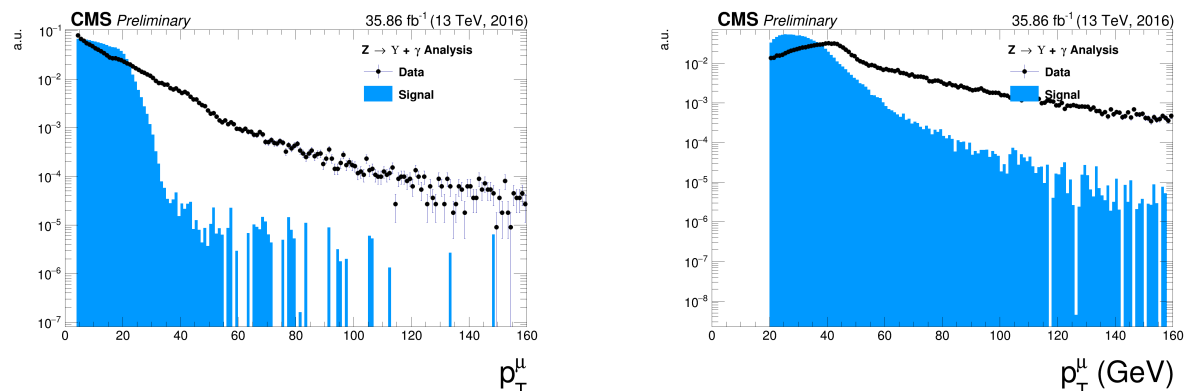


Figure 4.4: The p_T muon distributions from data and signal events for Z decaying in $\Upsilon(1S, 2S, 3S) + \gamma$ after Group I of selection cuts, where on left are presenting the trailing muons and on right are the leading muons. The plots are normalized to the unit of area.

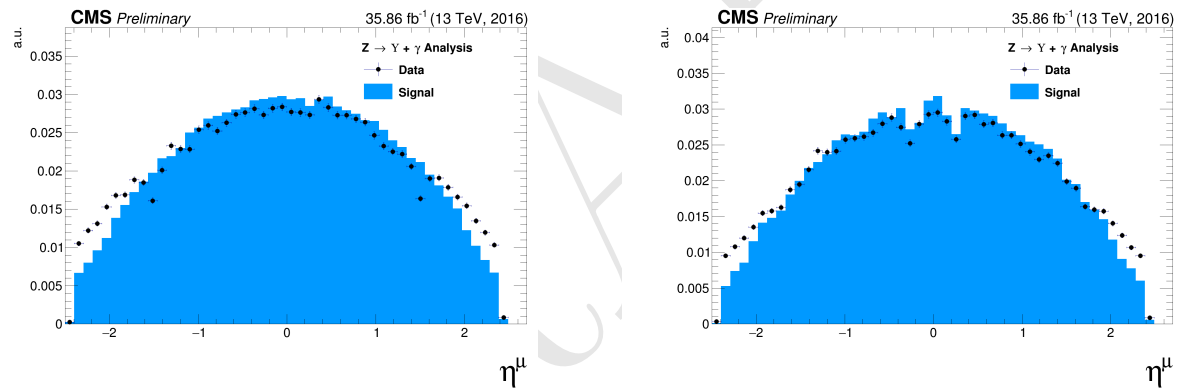


Figure 4.5: The η muon distributions from data and signal events of Z decaying in $\Upsilon(1S, 2S, 3S) + \gamma$ after Group I of selection cuts, where on left are presenting the trailing muons and on right are the leading muons. The plots are normalized to the unit of area.

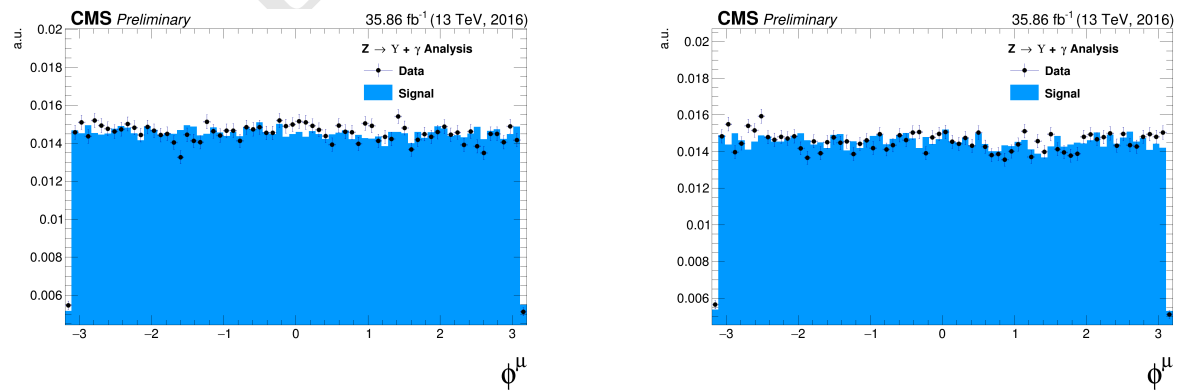


Figure 4.6: The ϕ muon distributions from data and signal events of Z decaying in $\Upsilon(1S, 2S, 3S) + \gamma$ after Group I of selection cuts, where on left are presenting the trailing muons and on right are the leading muons. The plots are normalized to the unit of area.

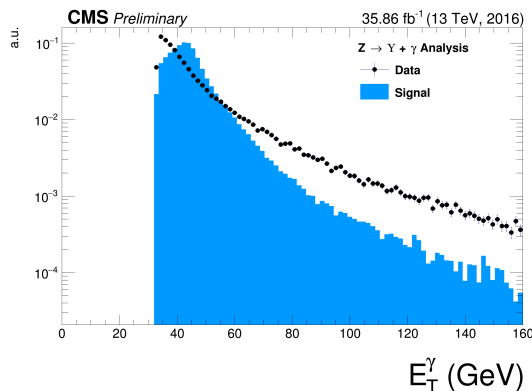


Figure 4.7: The p_T photon distributions from data and signal events for Z decaying in $\Upsilon(1S, 2S, 3S) + \gamma$ Group I of selection cuts. The plots normalized to the unit of area.

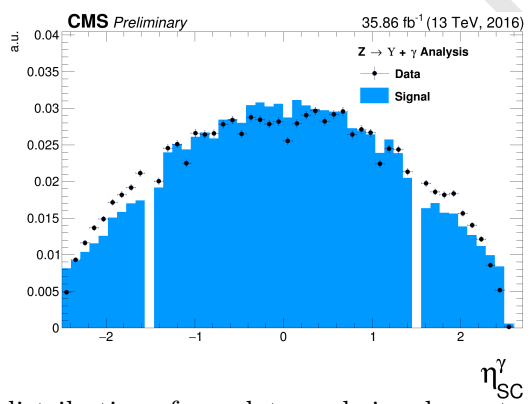


Figure 4.8: The η photon distributions from data and signal events of Z decaying in $\Upsilon(1S, 2S, 3S) + \gamma$ after Group I of selection cuts. The plot is normalized to the unit of area.

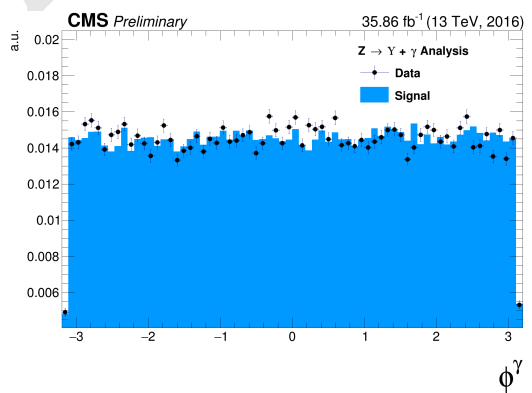


Figure 4.9: The ϕ photon distributions from data and signal events of Z decaying in $\Upsilon(1S, 2S, 3S) + \gamma$ after Group I of selection cuts. The plot is normalized to the unit of area.

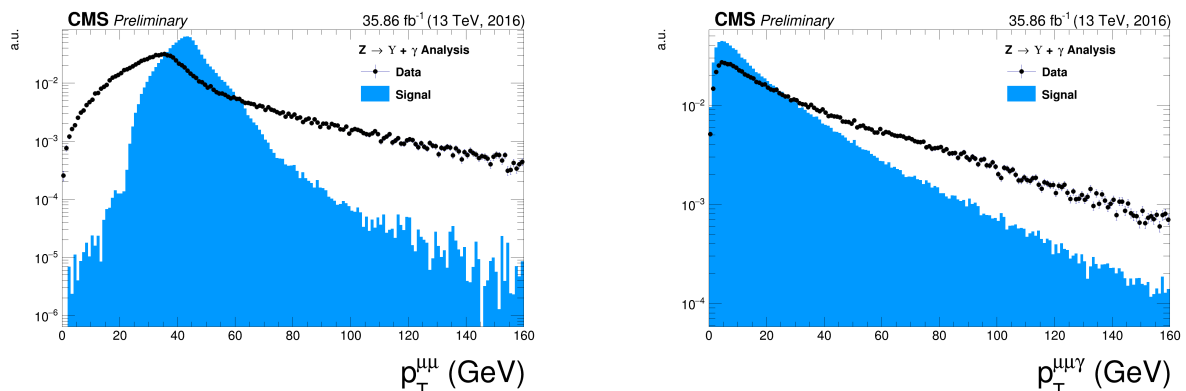


Figure 4.10: The p_T distributions for the reconstructed $\Upsilon(1S, 2S, 3S)$ in the left and for Z in the right from data and signal events for Z decaying in $\Upsilon(1S, 2S, 3S) + \gamma$ after Group I of selection cuts. The plots are normalized to the unit of area.

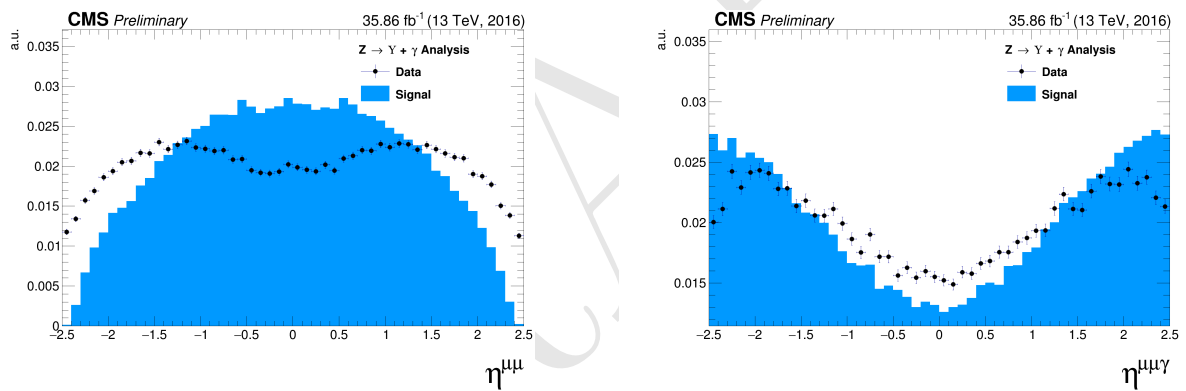


Figure 4.11: The η distributions for $\Upsilon(1S, 2S, 3S)$ in the left and for Z in the right from data and signal events for Z decaying in $\Upsilon(1S, 2S, 3S) + \gamma$ after Group I of selection cuts. The plots are normalized to the unit of area.

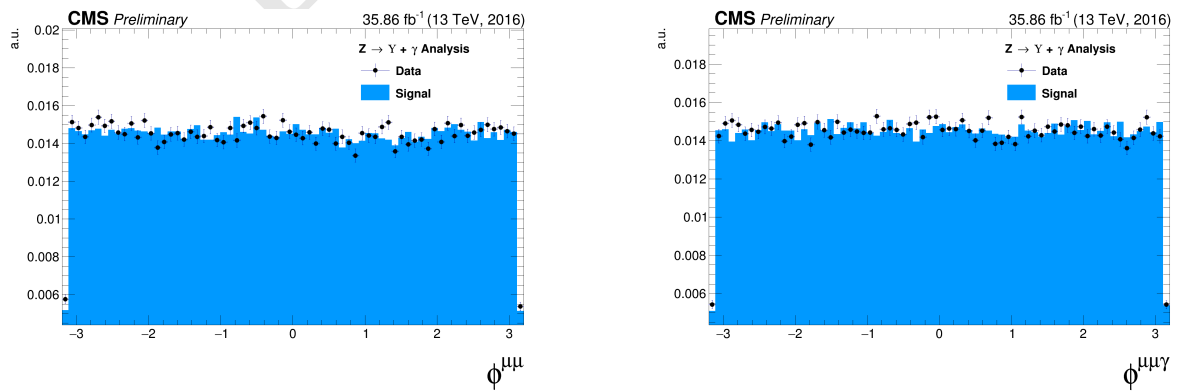


Figure 4.12: The ϕ distributions for $\Upsilon(1S, 2S, 3S)$ in the left and for Z in the right from data and signal events for Z decaying in $\Upsilon(1S, 2S, 3S) + \gamma$ after Group I of selection cuts. The plots are normalized to the unit of area.

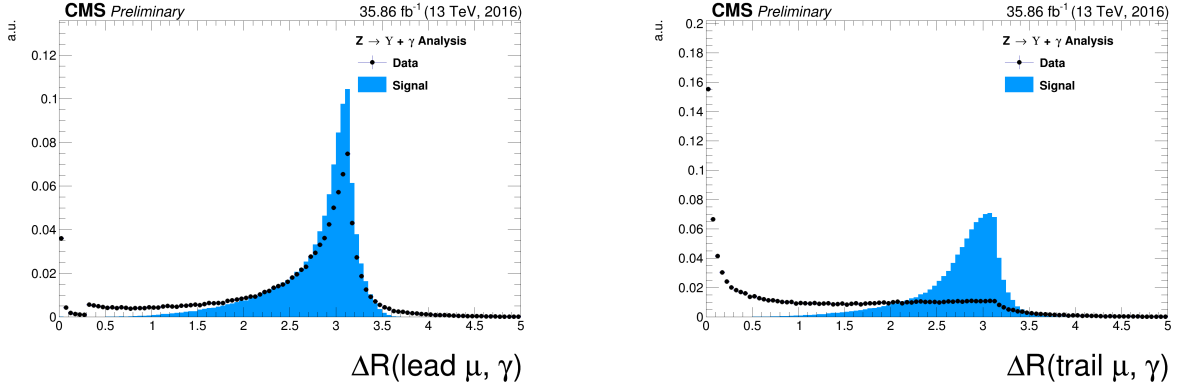


Figure 4.13: The ΔR distributions between the photon and the leading muon (left) and the trailing muon (right) for for Z decaying in $\Upsilon(1S, 2S, 3S) + \gamma$ from data and signal events after Group I of selection cuts. The plots are normalized to the unit of area.

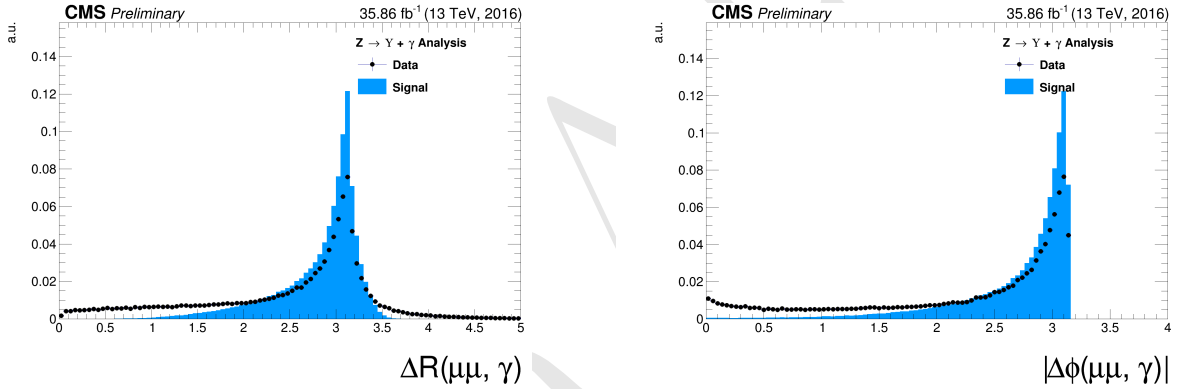


Figure 4.14: Left: The ΔR distributions between reconstructed dimuon ($\mu\mu$) system and the photon. Right: absolute value of the $\Delta\phi$ between the leading muon and the photon for for Z decaying in $\Upsilon(1S, 2S, 3S) + \gamma$ from data and signal events after Group I of selection cuts. The plots are normalized to the unit of area.

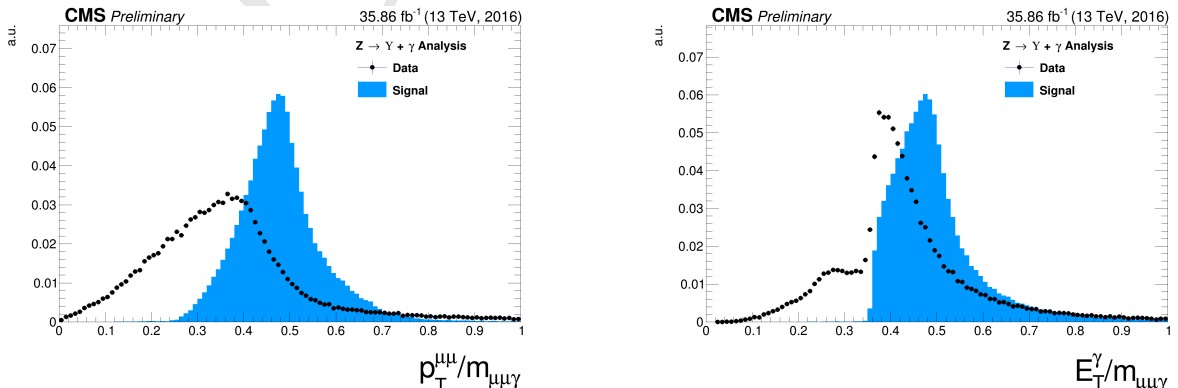


Figure 4.15: The ratio for the transverse momentum of the reconstructed Upsilon and the reconstructed Z mass ($p_T^{\mu\mu}/M_{\mu\mu\gamma}$ - left) and the ratio for the transverse energy of the reconstructed Photon and the reconstructed Z mass ($E_T^\gamma/M_{\mu\mu\gamma}$ - right) distribution for Z decaying in $\Upsilon(1S, 2S, 3S) + \gamma$ from data and signal events after Group I of selection cuts. The plots are normalized to the unit of area.

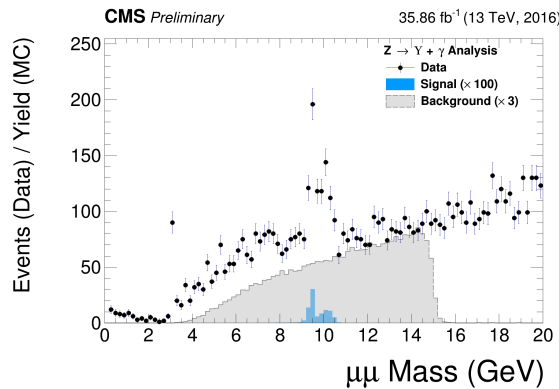


Figure 4.16: The dimuon mass distribution of the reconstructed $\Upsilon(1S, 2S, 3S)$ from data and signal events for Z decaying after Group I of selection cuts. The plot is normalized to the number of events. "Signal" stands for the $Z \rightarrow \Upsilon(1S, 2S, 3S) + \gamma$ sample (scaled by a factor of $\times 100$) and "Background" corresponds to the peaking background ($Z \rightarrow \mu\mu\gamma_{FSR}$) sample (scaled by a factor of $\times 3$).

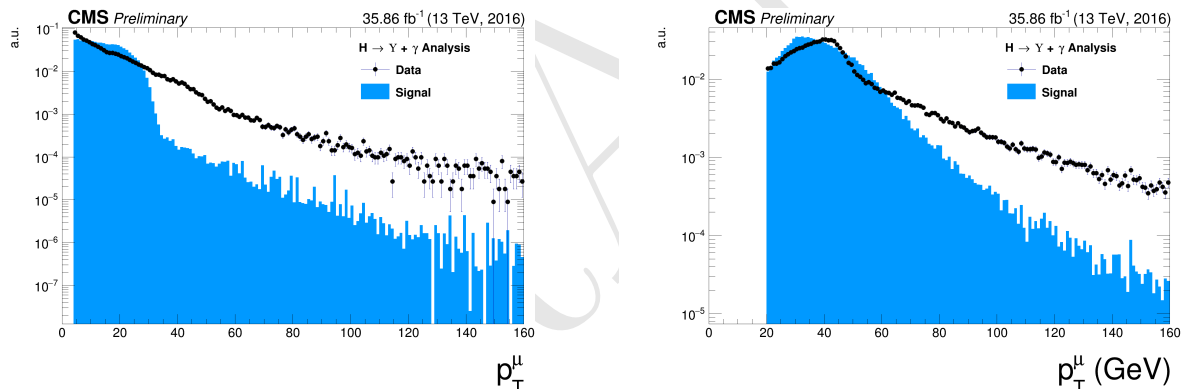


Figure 4.17: The p_T muon distributions from data and signal events for Higgs decaying in $\Upsilon(1S, 2S, 3S) + \gamma$ after Group I of selection cuts, where on left are presenting the trailing muons and on right are the leading muons. The plots are normalized to the unit of area.

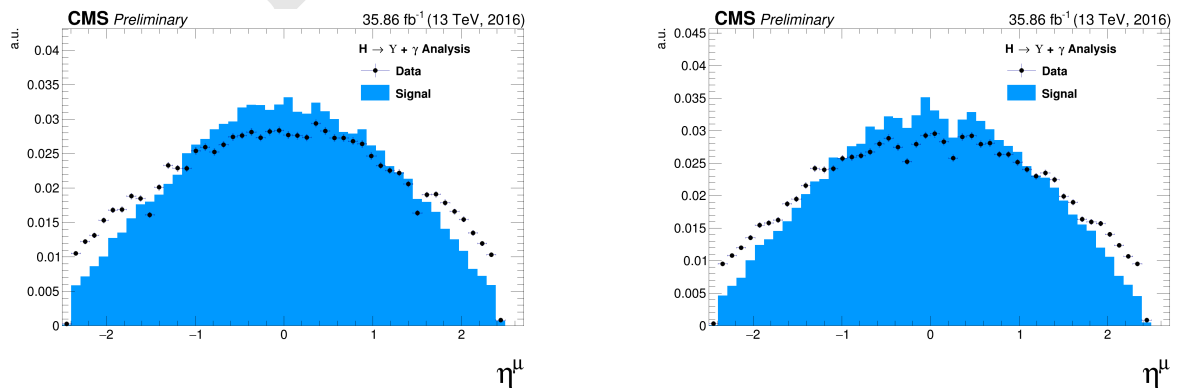


Figure 4.18: The η muon distributions from data and signal events of Higgs decaying in $\Upsilon(1S, 2S, 3S) + \gamma$ after Group I of selection cuts, where on left are presenting the trailing muons and on right are the leading muons. The plots are normalized to the unit of area.

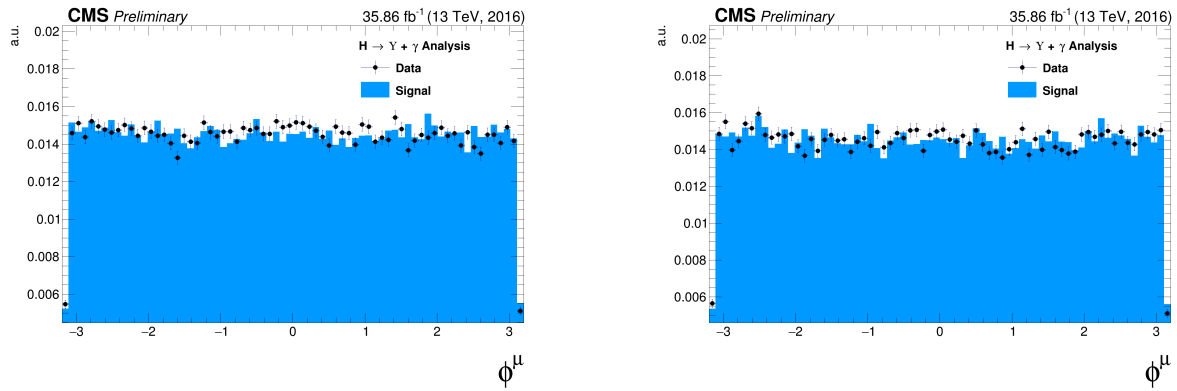


Figure 4.19: The ϕ muon distributions from data and signal events of Higgs decaying in $\Upsilon(1S, 2S, 3S) + \gamma$ after Group I of selection cuts, where on left are presenting the trailing muons and on right are the leading muons. The plots are normalized to the unit of area.

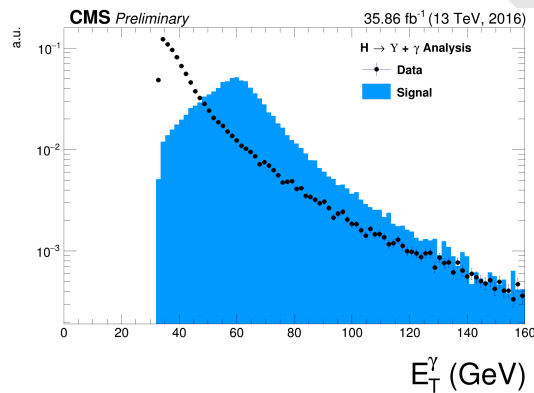


Figure 4.20: The p_T photon distributions from data and signal events for Higgs decaying in $\Upsilon(1S, 2S, 3S) + \gamma$ Group I of selection cuts. The plot is normalized to the unit of area.

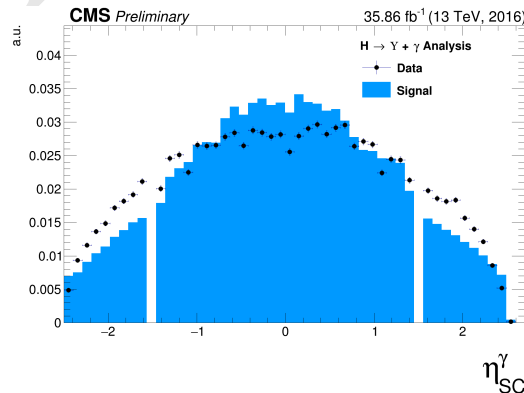


Figure 4.21: The η photon distributions from data and signal events of Higgs decaying in $\Upsilon(1S, 2S, 3S) + \gamma$ after Group I of selection cuts. The plot is normalized to the unit of area.

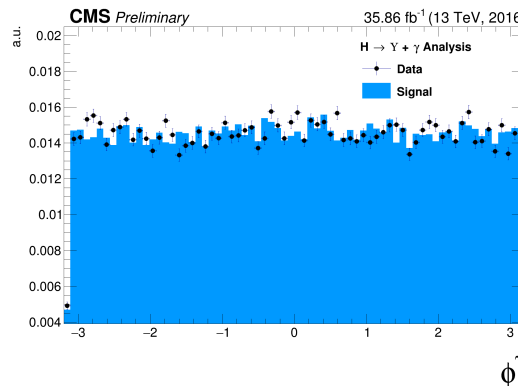


Figure 4.22: The ϕ photon distributions from data and signal events of Higgs decaying in $\Upsilon(1S, 2S, 3S) + \gamma$ after Group I of selection cuts. The plot is normalized to the unit of area.

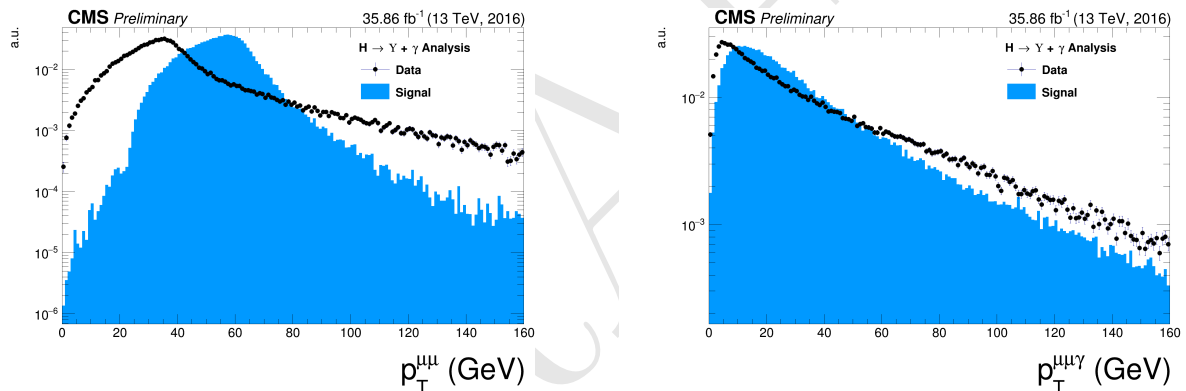


Figure 4.23: The p_T distributions for $\Upsilon(1S, 2S, 3S)$ in the left and for Higgs in the right from data and signal events for Higgs decaying in $\Upsilon(1S, 2S, 3S) + \gamma$ after Group I of selection cuts. The plots are normalized to the unit of area.

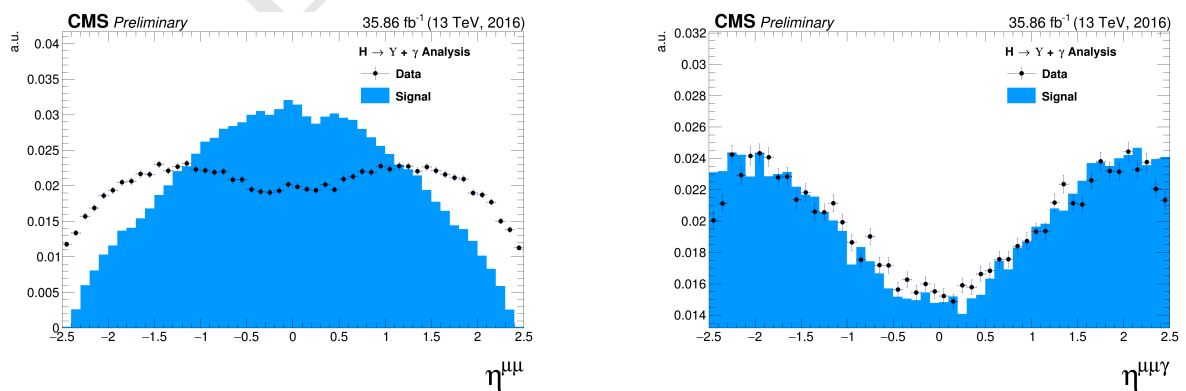


Figure 4.24: The η distributions for $\Upsilon(1S, 2S, 3S)$ in the left and for Higgs in the right from data and signal events for Higgs decaying in $\Upsilon(1S, 2S, 3S) + \gamma$ after Group I of selection cuts. The plots are normalized to the unit of area.

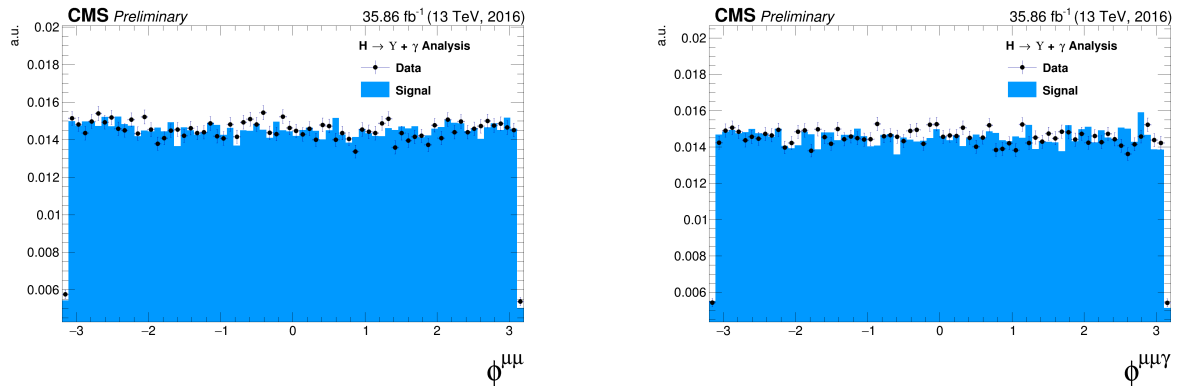


Figure 4.25: The ϕ distributions for $\Upsilon(1S, 2S, 3S)$ in the left and for Higgs in the right from data and signal events for Higgs decaying in $\Upsilon(1S, 2S, 3S) + \gamma$ after Group I of selection cuts. The plots are normalized to the unit of area.

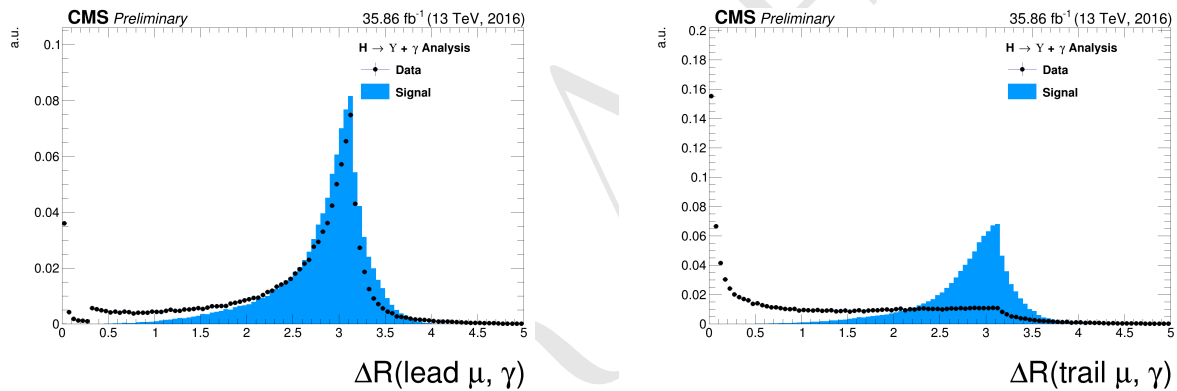


Figure 4.26: The ΔR distributions between the photon and the leading muon (left) and the trailing muon (right) for Higgs decaying in $\Upsilon(1S, 2S, 3S) + \gamma$ from data and signal events after Group I of selection cuts. The plots are normalized to the unit of area.

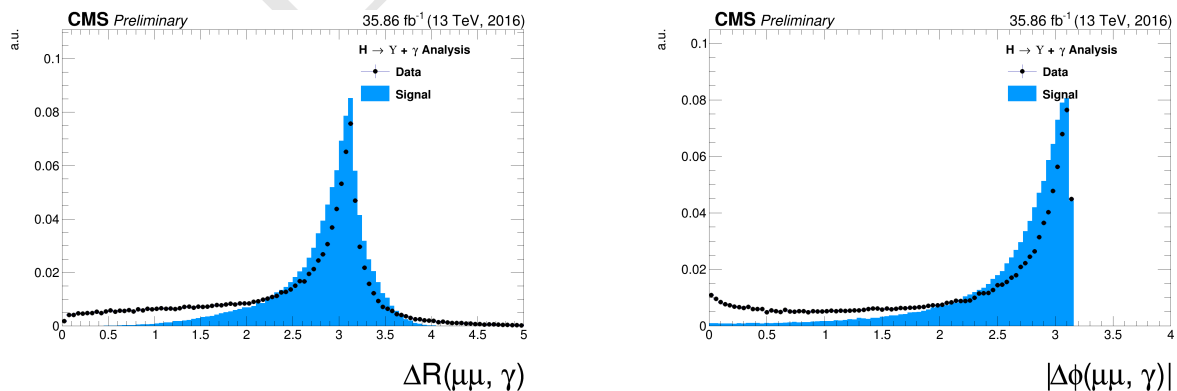


Figure 4.27: Left: The ΔR distributions between reconstructed dimuon ($\mu\mu$) system and the photon. Right: absolute value of the $\Delta\phi$ between the leading muon and the photon for Higgs decaying in $\Upsilon(1S, 2S, 3S) + \gamma$ from data and signal events after Group I of selection cuts. The plots are normalized to the unit of area.

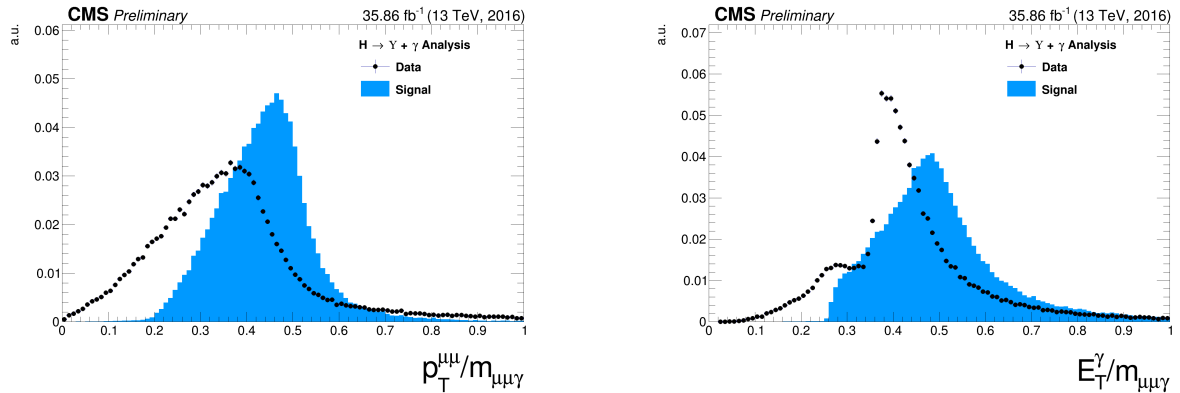


Figure 4.28: The ratio for the transverse momentum of the reconstructed Upsilon and the reconstructed Higgs mass ($p_T^{\mu\mu}/M_{\mu\mu\gamma}$ - left) and the ratio for the transverse energy of the reconstructed Photon and the reconstructed Higgs mass ($E_T^\gamma/M_{\mu\mu\gamma}$ - right) distribution for Higgs decaying in $\Upsilon(1S, 2S, 3S) + \gamma$ from data and signal events after Group I of selection cuts. The plots are normalized to the unit of area.

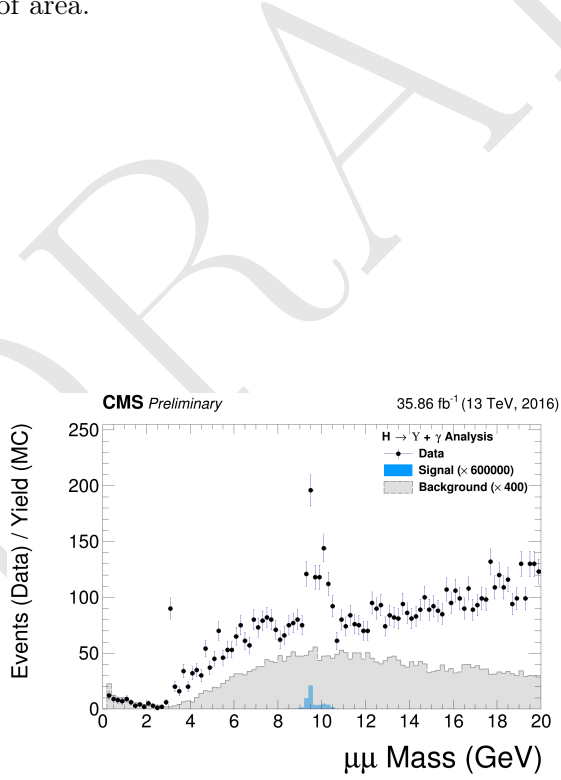


Figure 4.29: The dimuon mass distribution of the reconstructed $\Upsilon(1S, 2S, 3S)$ from data and signal events for Higgs decaying after Group I of selection cuts. This plot is normalized the expected number of events. The plot is normalized to the number of events. "Signal" stands for the $H \rightarrow \Upsilon(1S, 2S, 3S) + \gamma$ sample (scaled by a factor of $\times 60000$) and "Background" corresponds to the peaking background (Higgs Dalitz Decay) sample (scaled by a factor of $\times 400$).

4.6 Kinematical selection (Group II)

After all Trigger and Object Identification cuts, described in before (**Group I**), a set of kinematical cuts are applied in order to improve the signal to background relation. They are

- $\Delta R(\text{leading } \mu, \gamma) > 1$;
- $\Delta R(\text{trailing } \mu, \gamma) > 1$;
- $\Delta R(\mu\mu, \gamma) > 2$;
- $|\Delta\phi(\text{leading } \mu, \gamma)| > 1.5$;
- $8.4 \text{ GeV} < M_{\mu\mu} < 11.1 \text{ GeV}$;
- $E_T^\gamma/M_{\mu\mu\gamma} > 35/91.2$ for the Z decay or $35/125$ for the Higgs decay;
- $p_T^{\mu\mu}/M_{\mu\mu\gamma} > 35/91.2$ for the Z decay or $35/125$ for the Higgs decay.

The choice of these thresholds were based on the visual inspection of the distributions (besides the invariant mass distribution of the dimuon system $M_{\mu\mu}$, which needs to be defined around the $\nu(1S, 2S, 3S)$ mass) and to keep this analysis in phase with other similar analysis within CMS.

Below it is shown the same set of plot shown before, but this time, taking into account the full selection (**Group I+II**).

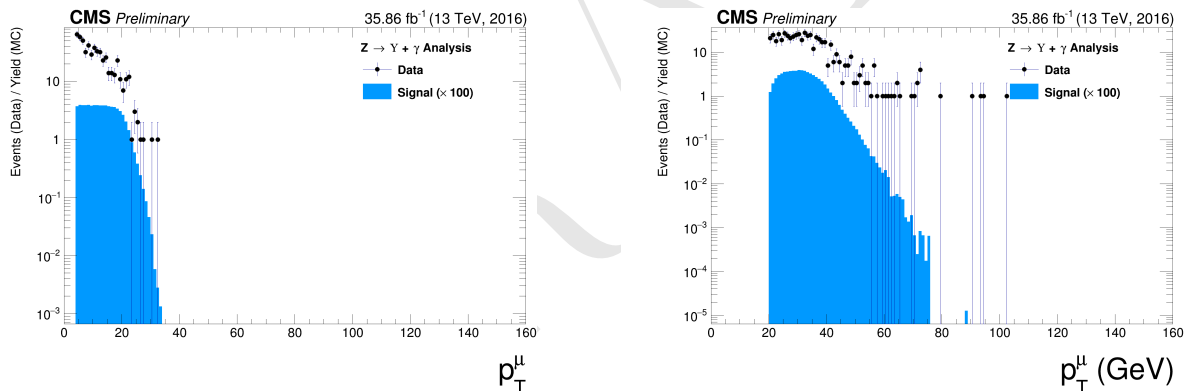


Figure 4.30: The p_T muon distributions from data and signal events for Z decaying in $\Upsilon(1S, 2S, 3S) + \gamma$ after Group I of selection cuts, where on left are presenting the trailing muons and on right are the leading muons. The plots are normalized to the number of events. Signal sample is scaled by a factor of $\times 100$.

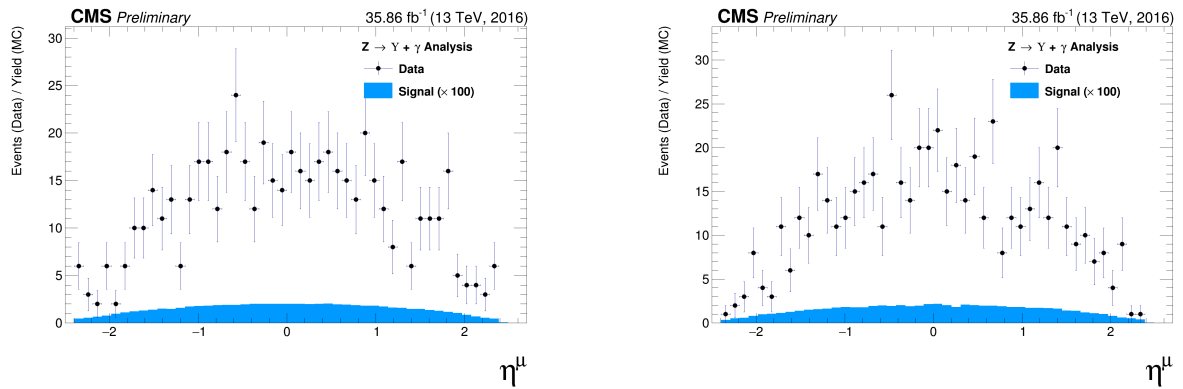


Figure 4.31: The η muon distributions from data and signal events of Z decaying in $\Upsilon(1S, 2S, 3S) + \gamma$ after Group I of selection cuts, where on left are presenting the trailing muons and on right are the leading muons. The plots are normalized to the number of events. Signal sample is scaled by a factor of $\times 100$.

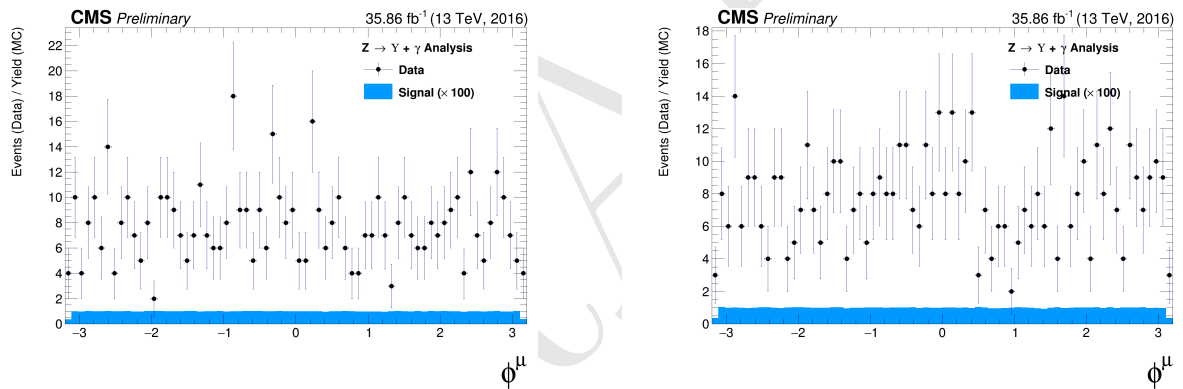


Figure 4.32: The ϕ muon distributions from data and signal events of Z decaying in $\Upsilon(1S, 2S, 3S) + \gamma$ after Group I of selection cuts, where on left are presenting the trailing muons and on right are the leading muons. The plots are normalized to the number of events. Signal sample is scaled by a factor of $\times 100$.

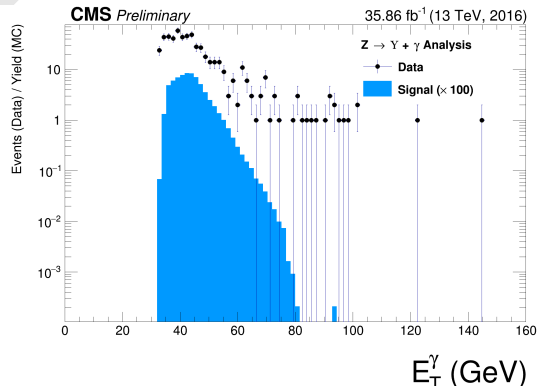


Figure 4.33: The p_T photon distributions from data and signal events for Z decaying in $\Upsilon(1S, 2S, 3S) + \gamma$ all (Group I+II) selection cuts. The plot is normalized to the number of events. Signal sample is scaled by a factor of $\times 100$.

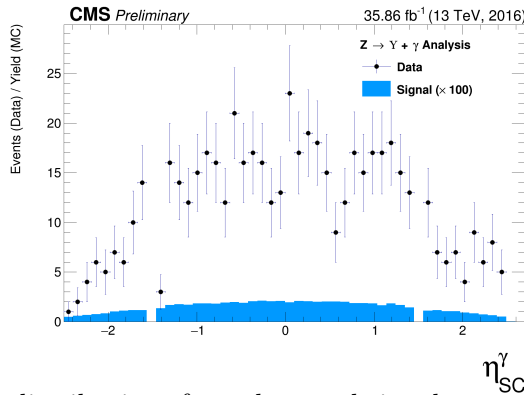


Figure 4.34: The η photon distributions from data and signal events of Z decaying in $\Upsilon(1S, 2S, 3S) + \gamma$ after all (Group I+II) selection cuts. The plot is normalized to the number of events. Signal sample is scaled by a factor of $\times 100$.

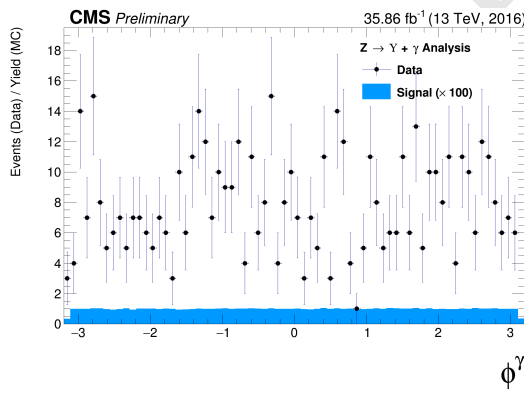


Figure 4.35: The ϕ photon distributions from data and signal events of Z decaying in $\Upsilon(1S, 2S, 3S) + \gamma$ after all (Group I+II) selection cuts. The plot is normalized to the number of events. Signal sample is scaled by a factor of $\times 100$.

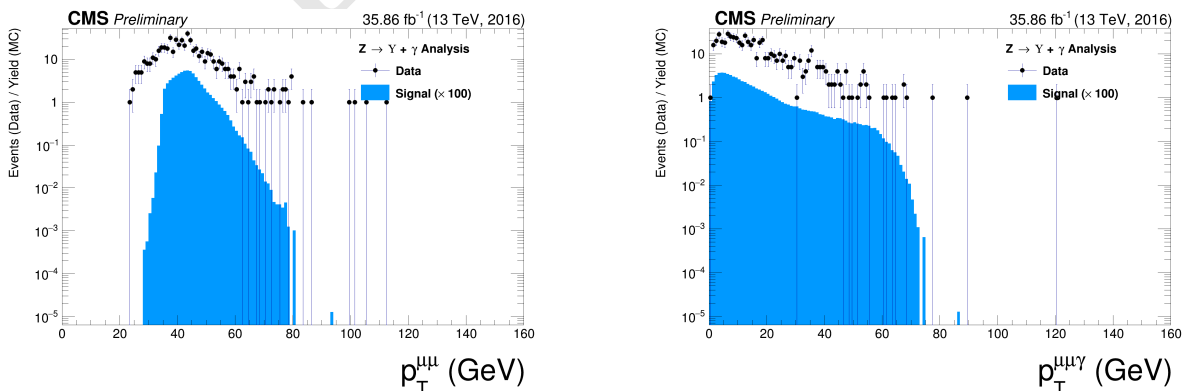


Figure 4.36: The p_T distributions for $\Upsilon(1S, 2S, 3S)$ in the left and for Z in the right from data and signal events for Z decaying in $\Upsilon(1S, 2S, 3S) + \gamma$ after all (Group I+II) selection cuts. The plots are normalized to the number of events. Signal sample is scaled by a factor of $\times 100$.

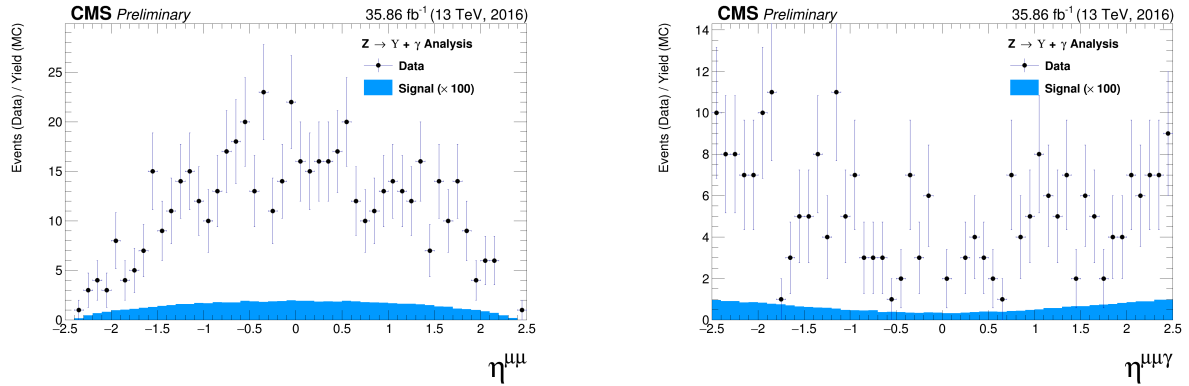


Figure 4.37: The η distributions for $\Upsilon(1S, 2S, 3S)$ in the left and for Z in the right from data and signal events for Z decaying in $\Upsilon(1S, 2S, 3S) + \gamma$ after all (Group I+II) selection cuts. The plots are normalized to the number of events. Signal sample is scaled by a factor of $\times 100$.

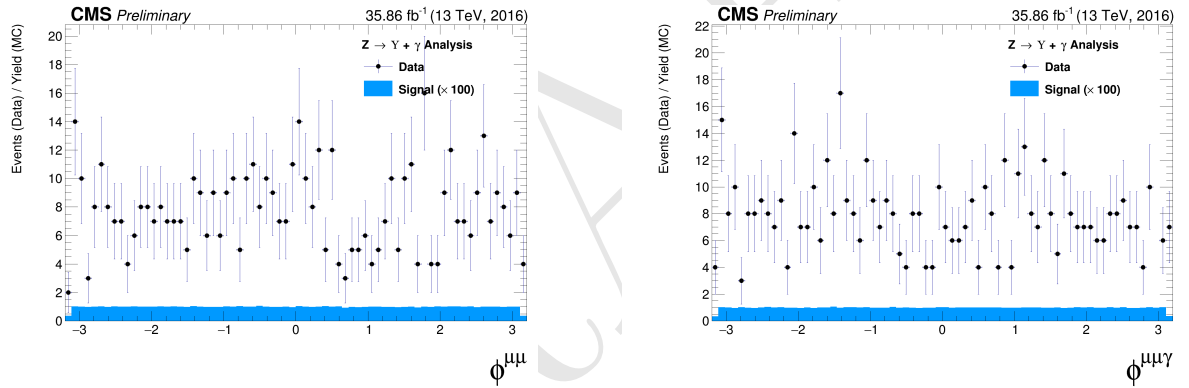


Figure 4.38: The ϕ distributions for $\Upsilon(1S, 2S, 3S)$ in the left and for Z in the right from data and signal events for Z decaying in $\Upsilon(1S, 2S, 3S) + \gamma$ after all (Group I+II) selection cuts. The plots are normalized to the number of events. Signal sample is scaled by a factor of $\times 100$.

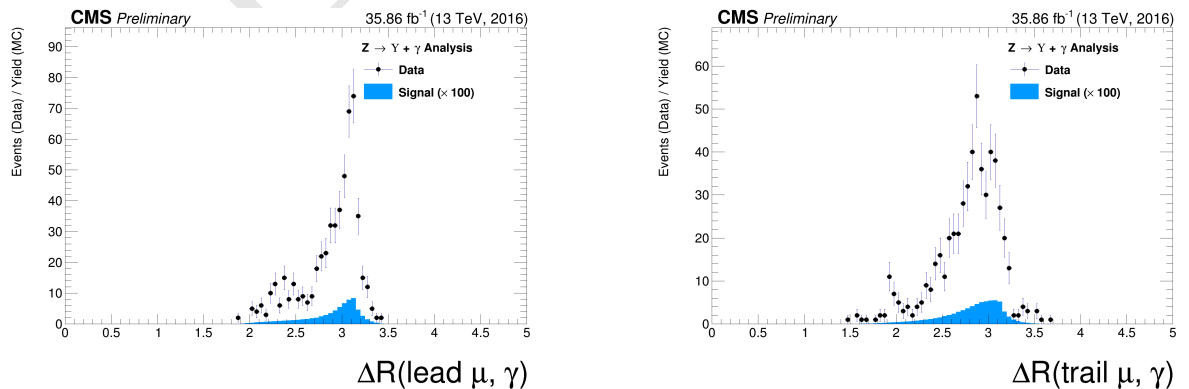


Figure 4.39: The ΔR distributions between the photon and the leading muon (left) and the trailing muon (right) for $\Upsilon(1S, 2S, 3S)$ from data and signal events for Z decaying after all (Group I+II) selection cuts. The plots are normalized to the number of events. Signal sample is scaled by a factor of $\times 100$.

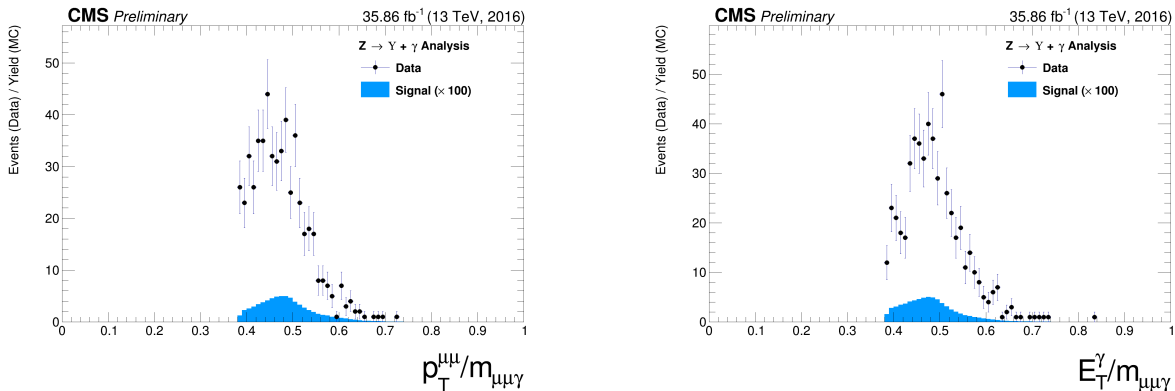


Figure 4.40: The ratio for the transverse momentum of the reconstructed Upsilon and the reconstructed Z mass ($p_T^{\mu\mu}/M_{\mu\mu\gamma}$ - left) and the ratio for the transverse energy of the reconstructed Photon and the reconstructed Z mass ($E_T^\gamma/M_{\mu\mu\gamma}$ - right) distribution for $\Upsilon(1S, 2S, 3S)$ from data and signal events for Z decaying after all (Group I+II) selection cuts. The plots are normalized to the number of events. Signal sample is scaled by a factor of $\times 100$.

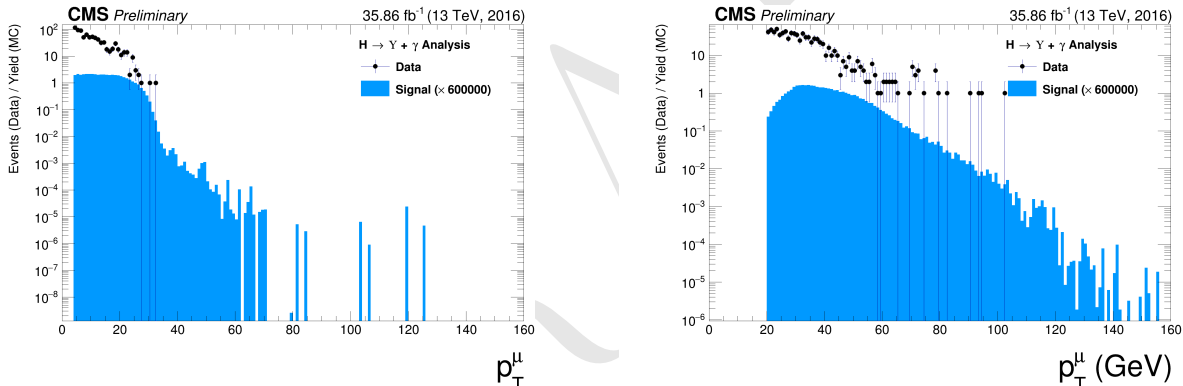


Figure 4.41: The p_T muon distributions from data and signal events for Higgs decaying in $\Upsilon(1S, 2S, 3S) + \gamma$ after Group I of selection cuts, where on left are presenting the trailing muons and on right are the leading muons. The plots are normalized to the number of events. Signal sample is scaled by a factor of $\times 600000$.

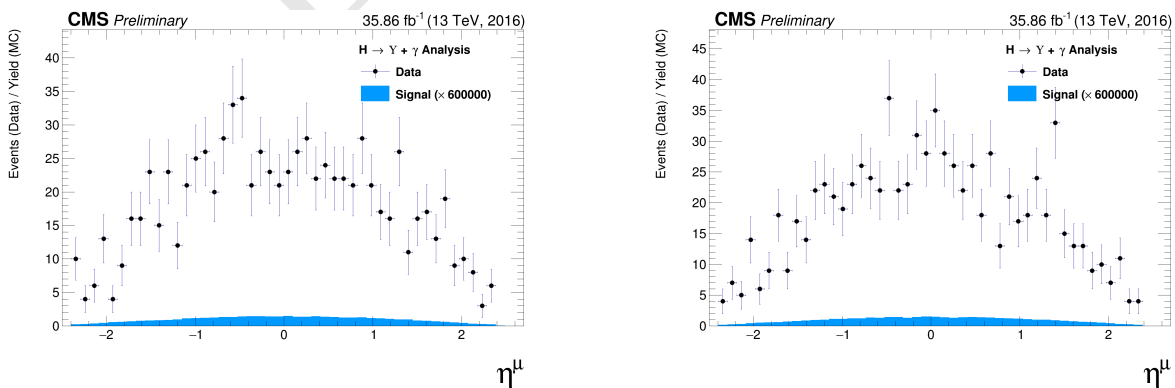


Figure 4.42: The η muon distributions from data and signal events of Higgs decaying in $\Upsilon(1S, 2S, 3S) + \gamma$ after Group I of selection cuts, where on left are presenting the trailing muons and on right are the leading muons. The plots are normalized to the number of events. Signal sample is scaled by a factor of $\times 600000$.

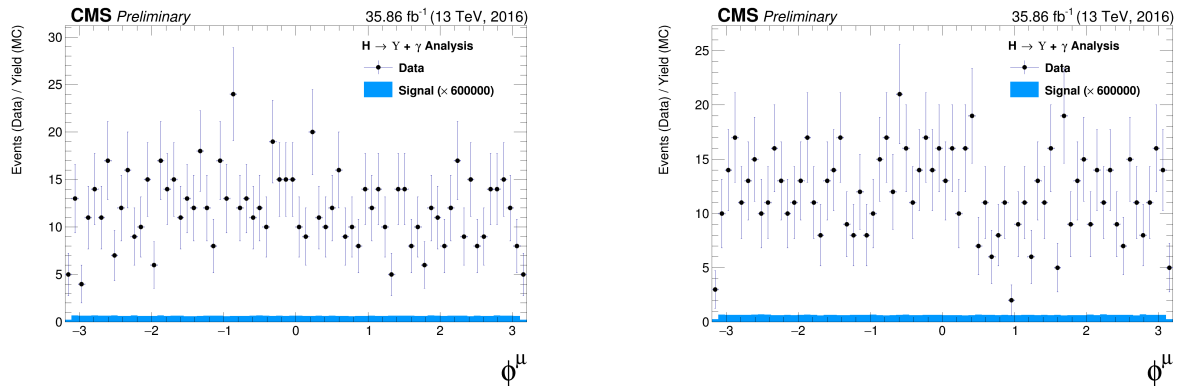


Figure 4.43: The ϕ muon distributions from data and signal events of Higgs decaying in $\Upsilon(1S, 2S, 3S) + \gamma$ after Group I of selection cuts, where on left are presenting the trailing muons and on right are the leading muons. The plots are normalized to the number of events. Signal sample is scaled by a factor of $\times 600000$.

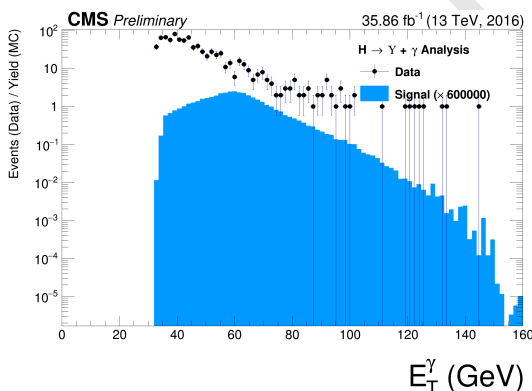


Figure 4.44: The p_T photon distributions from data and signal events for Higgs decaying in $\Upsilon(1S, 2S, 3S) + \gamma$ all (Group I+II) selection cuts. The plot is normalized to the number of events. Signal sample is scaled by a factor of $\times 600000$.

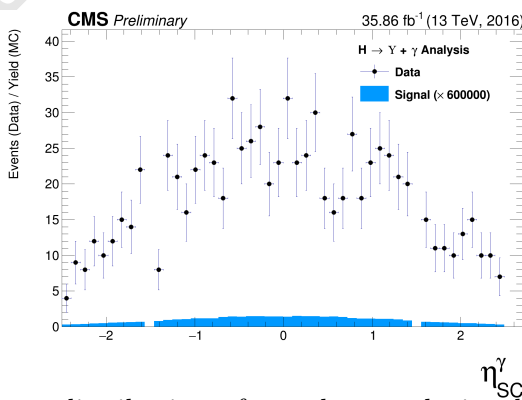


Figure 4.45: The η photon distributions from data and signal events of Higgs decaying in $\Upsilon(1S, 2S, 3S) + \gamma$ after all (Group I+II) selection cuts. The plot is normalized to the number of events. Signal sample is scaled by a factor of $\times 600000$.

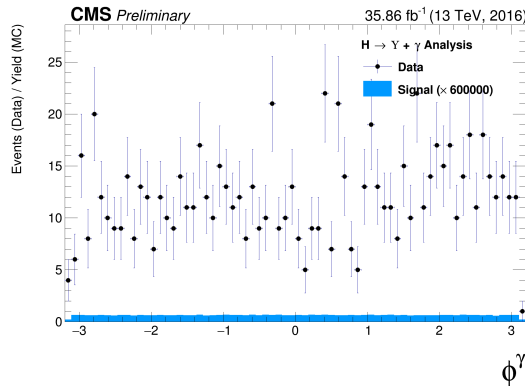


Figure 4.46: The ϕ photon distributions from data and signal events of Higgs decaying in $\Upsilon(1S, 2S, 3S) + \gamma$ after all (Group I+II) selection cuts. The plot is normalized to the number of events. Signal sample is scaled by a factor of c).

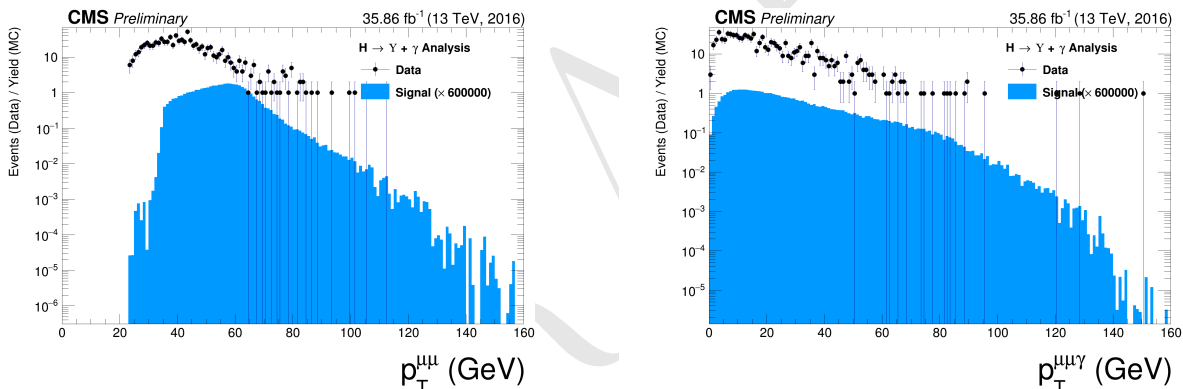


Figure 4.47: The p_T distributions for $\Upsilon(1S, 2S, 3S)$ in the left and for Higgs in the right from data and signal events for Higgs decaying in $\Upsilon(1S, 2S, 3S) + \gamma$ after all (Group I+II) selection cuts. The plots are normalized to the number of events. Signal sample is scaled by a factor of $\times 600000$.

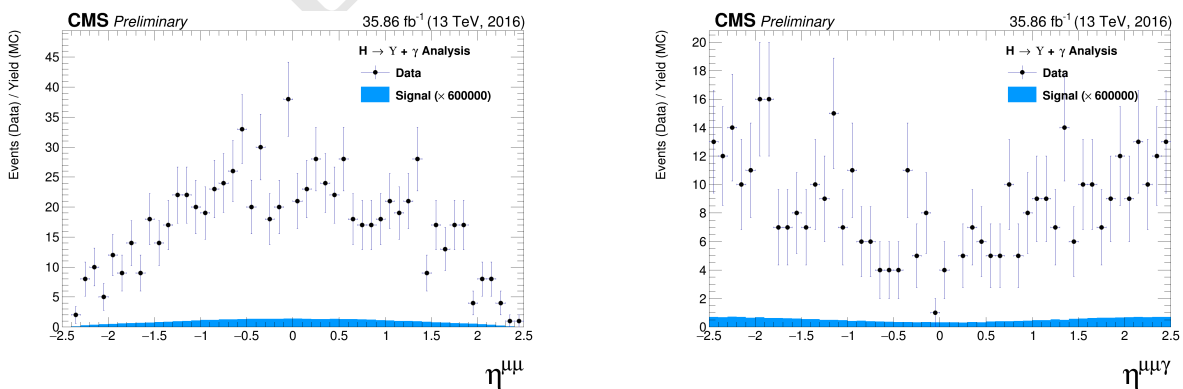


Figure 4.48: The η distributions for $\Upsilon(1S, 2S, 3S)$ in the left and for Higgs in the right from data and signal events for Higgs decaying in $\Upsilon(1S, 2S, 3S) + \gamma$ after all (Group I+II) selection cuts. The plots are normalized to the number of events. Signal sample is scaled by a factor of $\times 600000$.

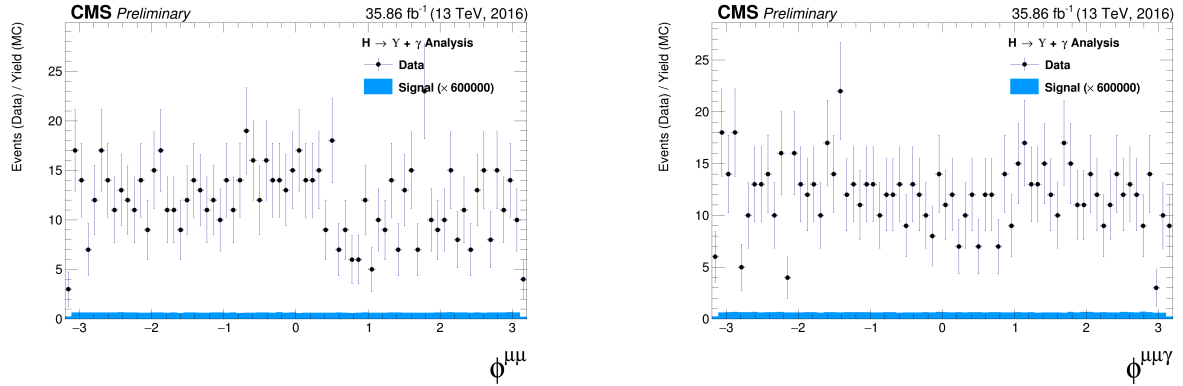


Figure 4.49: The ϕ distributions for $\Upsilon(1S, 2S, 3S)$ in the left and for Higgs in the right from data and signal events for Higgs decaying in $\Upsilon(1S, 2S, 3S) + \gamma$ after all (Group I+II) selection cuts. The plots are normalized to the number of events. Signal sample is scaled by a factor of $\times 600000$.

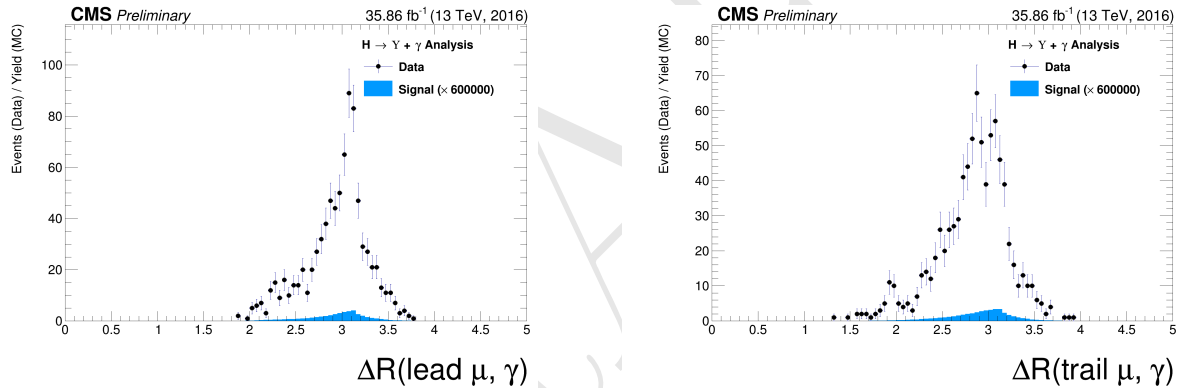


Figure 4.50: The ΔR distributions between the photon and the leading muon (left) and the trailing muon (right) for $\Upsilon(1S, 2S, 3S)$ from data and signal events for Higgs decaying after all (Group I+II) selection cuts. The plots are normalized to the number of events. Signal sample is scaled by a factor of $\times 600000$.

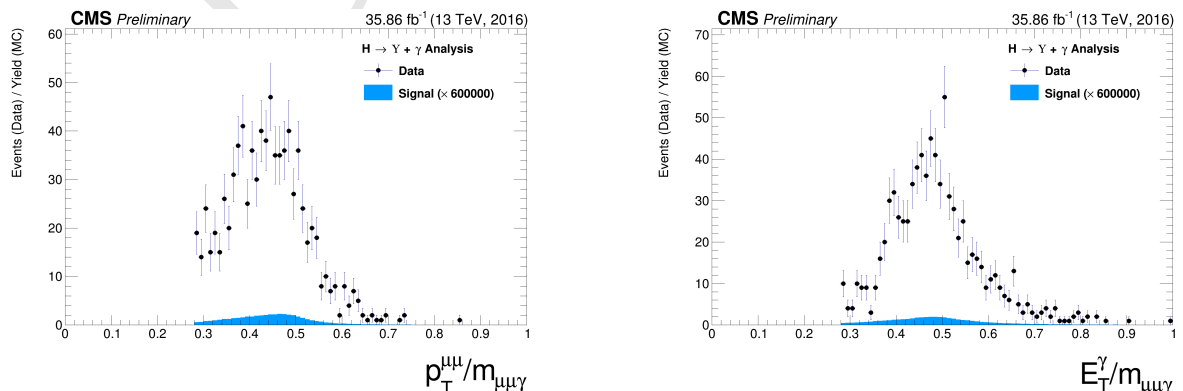


Figure 4.51: The ratio for the transverse momentum of the reconstructed Upsilon and the reconstructed Higgs mass ($p_T^{\mu\mu}/M_{\mu\mu\gamma}$ - left) and the ratio for the transverse energy of the reconstructed Photon and the reconstructed Higgs mass ($E_T^{\gamma\gamma}/M_{\mu\mu\gamma}$ - right) distribution for $\Upsilon(1S, 2S, 3S)$ from data and signal events for Higgs decaying after all (Group I+II) selection cuts. The plots are normalized to the number of events. Signal sample is scaled by a factor of $\times 600000$.

4.7 Event categorization and yields

In order to increase the sensibility of the analysis, a categorization procedure was applied. They are based on the η and R9 distribution of the reconstructed photon.

The photon R9 is a shower shape variable defined as the fraction of energy deposited in the 5x5 square surrounding the Super Cluster seed of the reconstructed photon. A photon that convert before reaching the ECAL tend to have lower values of R9, in comparison with unconverted photons. Converted photons have wider energy resolution and are more likely to be misidentified.

Selected events with the photon reconstructed inside the barrel and with $R9 > 0.94$ are categorized as "EB High R9"⁶, selected events with the photon reconstructed inside the barrel and with $R9 < 0.94$ are categorized as "EB Low R9" and selected events with the photon reconstructed inside the endcap, regardless of its R9 value, categorized as "EE". This categorization is done in view of increase the analysis sensitivity.

This categorization is implemented only for the Z decay. The Higgs does not present enough statistics to make it profitable, so only the inclusive one is used.

4.7.1 R9 reweighting

As spotted by the $H \rightarrow \gamma\gamma$ at $\sqrt{13}$ TeV analysis [61], there is a disagreement in the R9 distribution of photons in Data and MC. In order to mitigate this difference, a transformation factor is extracted and applied to the reconstructed photons before the categorization.

The same approach of the $H \rightarrow \gamma\gamma$ analysis is applied, in which the nominal photon selection of this analysis (see section 4.5.3) is used to select photons on Data and MC. Then the two distributions are remapped and the transformation factors are extracted.

Figure 4.52 show the R9 distribution before and after the reweighting, for the Barrel and the Endcap.

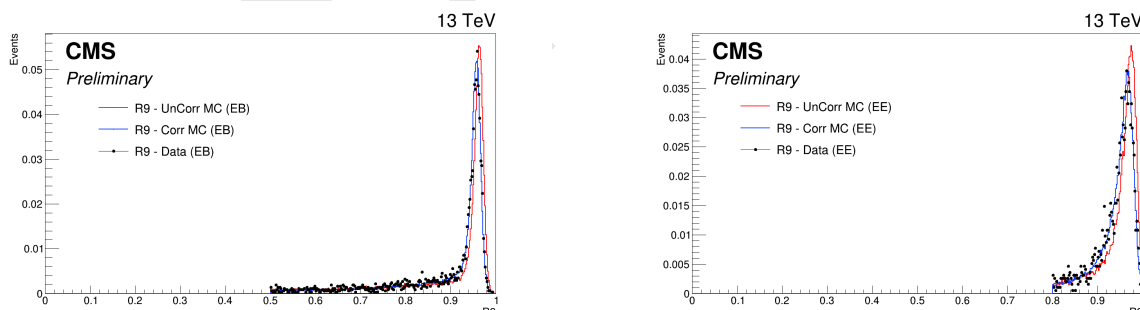


Figure 4.52: Data and MC of the R9 variable, before and after the reweighting. Barrel (left) and Endcap (right).

4.7.2 Event counting and yields

Tables 4.4 and 4.5 show the total number of events before and after the full selection. Two things are important to notice.

The signal selection efficiency is between 20% and 21% for all Υ states and categories.

⁶EB stands for Electromagnetic Barrel

Table 4.4: Number of events for the Z decay, before and after the full selection, per categorization scenarios.

| | Data | Signal | | | $Z \rightarrow \mu\mu\gamma_{FSR}$ |
|--------------------------|----------|---------------------------------------|---------------------------------------|---------------------------------------|------------------------------------|
| | | $Z \rightarrow \Upsilon(1S) + \gamma$ | $Z \rightarrow \Upsilon(2S) + \gamma$ | $Z \rightarrow \Upsilon(3S) + \gamma$ | |
| Total (before selection) | 169.84 M | 3.54 | 1.4 | 1.22 | 3.33×10^3 |
| Inclusive | 447 | 0.393 | 0.157 | 0.136 | 176 |
| EB High R9 | 197 | 0.172 | 0.0682 | 0.0597 | 78 |
| EB Low R9 | 146 | 0.129 | 0.0519 | 0.0448 | 58.5 |
| EE | 104 | 0.0916 | 0.0365 | 0.032 | 39.8 |

Table 4.5: Number of events for the H decay, before and after the full selection.

| | Data | Signal | | | $H \rightarrow \gamma\gamma^*$ |
|--------------------------|----------|---------------------------------------|---------------------------------------|---------------------------------------|--------------------------------|
| | | $H \rightarrow \Upsilon(1S) + \gamma$ | $H \rightarrow \Upsilon(2S) + \gamma$ | $H \rightarrow \Upsilon(3S) + \gamma$ | |
| Total (before selection) | 169.84 M | 0.000257 | 5.43×10^{-5} | 3.93×10^{-5} | 136 |
| Inclusive | 231 | 5.23×10^{-5} | 1.2×10^{-5} | 8.96×10^{-6} | 1.22 |

When one compares the fraction of selected peaking background, with respect to the selected data events for the Higgs decay ($1.22/231$), the fraction obtained ($\sim 0.3\%$) is irrelevant. On the other hand, the same fraction for the Z decay ($176/447$) is far from irrelevant ($\sim 39\%$)⁷. The same relation is not found in the $H/Z \rightarrow J/\psi + \gamma$ analysis [29], where both decays (Higgs and Z) show neglectable estimations of peaking background contribution to data. The very same behavior was found by ATLAS [26]. It can be explained by the relatively larger cross-section of the Z peaking background ($Z \rightarrow \mu\mu\gamma_{FSR}$), with respect to the Higgs peaking background (Higgs Dalitz Decay). For the J/ψ channel, it is not an issue since its cross-section is way larger than the peaking background. The figures 4.16 and 4.29 help to clarify these affirmations, for the Z and Higgs decay, respectively. One can easily see how clear the J/ψ peak is in both decays and how minor the Higgs Dalitz Decay contributions is to the Υ peak, with respect to the $Z \rightarrow \mu\mu\gamma_{FSR}$ contribution. It is important to keep in mind the different scaling of the peaking background distributions, $\times 3$ for the Z and $\times 100$ for the Higgs. The peaking background to the data due to $Z \rightarrow \Upsilon(1S, 2S, 3S) + \gamma$ channel is the main motivation to use a 2-dimensional modeling fitting of the signal and background events, in order to add one more layer of differentiation between many backgrounds contributions which will be detailed in the next section.

⁷It is worth to keep in mind that this is a estimation based on MC

4.8 Background modeling

The background modeling proposed for this analysis is a two dimensional unbinned maximum likelihood fit on the $\mu\mu$ and the $\mu\mu\gamma$ invariant mass distributions. It is considered and modeled, as briefly discussed in 4.1.2, three kinds of backgrounds:

- **Full Combinatorial:** any combination of two muon and one photon that pass all the object reconstruction and event selection criteria.
- **Υ Combinatorial:** a $\Upsilon(1S, 2S, 3S)$, that decays to a dimuon system, combined with a misidentified photon (misreconstructed, Pile-up photon, etc.), that pass all the object reconstruction, identification and event selection criteria.
- **Peaking background:** a Z (or Higgs) that decays straight to a $\mu\mu\gamma$, that pass all the object reconstruction and event selection criteria, without passing through any intermediate state. The main contributions considered for this background are $Z \rightarrow \mu\mu\gamma_{FSR}$ (a Z decaying to a dimuon system with one of the muons irradiating a photon) or a Higgs Dalitz Decay.

All of them will be modeled from data, with some inputs from the MC (simulated) samples, as explained below. For both invariant mass spectra ($\mu\mu$ and $\mu\mu\gamma$) the full combinatorial background is expected to behave like a non-peaking distribution. The same behavior is expected for the $\mu\mu\gamma$ mass distribution of the Υ Combinatorial background and for the $\mu\mu$ mass distribution of the peaking background.

On the other hand, the $\mu\mu$ distribution of the Υ Combinatorial background and the $\mu\mu\gamma$ mass distribution for the peaking background are expected to behave like a peaking distribution, centered around the $\Upsilon(1S, 2S, 3S)$ invariant mass (9.46 GeV, 10.02 GeV and 10.35 GeV) [2] and the Z boson invariant mass (91.2 GeV) [2], respectively . Table 4.6 summarizes the background modeling proposed for this analysis.

Table 4.6: Modeling for each background source and mass component.

| | $m_{\mu\mu}$ | $m_{\mu\mu\gamma}$ |
|--|---|---|
| Peaking background | Bernstein 1 st order | Crystal Ball (Higgs decay) Double Crystal Ball (Z decay) |
| Υ Combinatorial | 3 Gaussians (one for each Υ state) | |
| Full Combinatorial | Chebychev 1 st order | Polynomial |

For the $Z \rightarrow \Upsilon(1S, 2S, 3S) + \gamma$ analysis, the peaking background model parameters are extracted by performing a simultaneous 2-dimensional fit over the invariant masses, $m_{\mu\mu}$ and $m_{\mu\mu\gamma}$, of the simulated $Z \rightarrow \mu\mu\gamma_{FSR}$ MC sample of events that passes the selection described in Section 4.4, as in figure 4.53. Once the parameters are extracted, they are fixed and the *pdf* (Probability Distributions Function) of the 2-Dimensional modeling is stored, leaving only the normalization of the *pdf* as a parameter free to float (this will be determined from data).

In order to describe the 2-dimensional invariant mass distribution of the Peaking Background, as stated in Table 4.6, the $m_{\mu\mu}$ component is described by a Bernstein polynomial of 1st order [62], which is used here just a representation of a linear function. The $m_{\mu\mu\gamma}$ component is described by Double Crystal Ball function [63]. A Crystal Ball function is a *pdf* composed by a gaussian distribution and a power-law tail to the left, before certain threshold. The Crystal Ball function was named after the Crystal Ball Collaboration (first to use this *pdf*) and it is widely used in high-energy physics to describe mass distributions that incorporate FSR (final state radiation) effects, via the power-law tail. A Double Crystal Ball is a Crystal Ball function with the power-law tail on both sides.

961 A Crystal Ball function is define as:

$$CB(x; \alpha, n, \bar{x}, \sigma) = N \cdot \begin{cases} \exp\left(-\frac{(x-\bar{x})^2}{2\sigma^2}\right), & \text{for } \frac{x-\bar{x}}{\sigma} > -\alpha \\ A \cdot (B - \frac{x-\bar{x}}{\sigma})^{-n}, & \text{for } \frac{x-\bar{x}}{\sigma} \leq -\alpha \end{cases}, \quad (4.4)$$

962 where,

$$963 A = \left(\frac{n}{|\alpha|}\right)^n \cdot \exp\left(-\frac{|\alpha|^2}{2}\right),$$

$$964 B = \frac{n}{|\alpha|} - |\alpha|,$$

$$965 N = \frac{1}{\sigma(C+D)},$$

$$966 C = \frac{n}{|\alpha|} \cdot \frac{1}{n-1} \cdot \exp\left(-\frac{|\alpha|^2}{2}\right),$$

$$967 D = \sqrt{\frac{\pi}{2}} \left(1 + \operatorname{erf}\left(\frac{|\alpha|}{\sqrt{2}}\right)\right),$$

968 and erf is the error function.

969 For the three gaussian functions fits, which represent the three Υ states (1S, 2S and 3S) from the Υ
 970 Combinatorial background in the $m_{\mu\mu}$ component, we use a Υ control sample in order to extract the
 971 fit parameters, including the relative normalization between each Υ state. This sample is composed
 972 by dimuon candidates obtained from data, by selecting the events that passes the same trigger and
 973 dimuon selection of the nominal selection and with $p_T^{\mu\mu} > 35$ GeV (this cut is done in order to
 974 keep this selected dimuon candidates compatibles with the $p_T^{\mu\mu}/M_{\mu\mu\gamma}$ cut applied in the nominal
 975 selection). No selection or cuts in the photon are required.

976 This control sample is fitted with a Chebychev 1st order (linear polynomial) for the background
 977 support and 3 gaussian with the following constraints:

- 978 • the mean of each state should be the ones in the PDG [2], but allowed to shift by a float and
 979 common (the same for all states) value.
- 980 • the sigma should be based on the 1S fit of the MC. All other sigma should be the result of
 981 the 1S sigma times the state mass over the 1S mass ($\sigma_{2S,3S} = \frac{m_{2S,3S}}{m_{1S}} \sigma_{1S}$).

982 The idea behind this fit is that scale and resolution (mean and sigma, respectively, of the gaussians)
 983 over a sample without a photon selection should be the same as over a sample with photon selection,
 984 since these are detector only dependent effects. The fact that we exclude the photon from this control
 985 sample, improves the statistics and gives a better measurement of these variables.

986 The fit of the Υ control sample if shown in figure 4.54.

987 Once determined, the fit parameters are fixed, they are used to compose the 2-Dimensional *pdf*. The
 988 $m_{\mu\mu}$ component of the full combinatorial background is derived fully from the data fit (described
 989 below). In the same sense, the $m_{\mu\mu\gamma}$ component of the full combinatorial and the $\Upsilon(nS)$ Combi-
 990 torial backgrounds are also fully derived from the data, but following a more complex procedure:
 991 a composition with the *pdf* components described above, plus a statistical test, to avoid overfit-
 992 ting within a Discrete Profiling (or "Envelope Method"), as described in [64] and also implemented
 993 in [61].

994 The statistical test consists of, for each category, different orders of a set of polynomial *pdfs* families
 995 are tested: a sums of exponentials, sum of polynomials (in the Bernstein basis), a Laurent series
 996 and a sums of power-law functions.

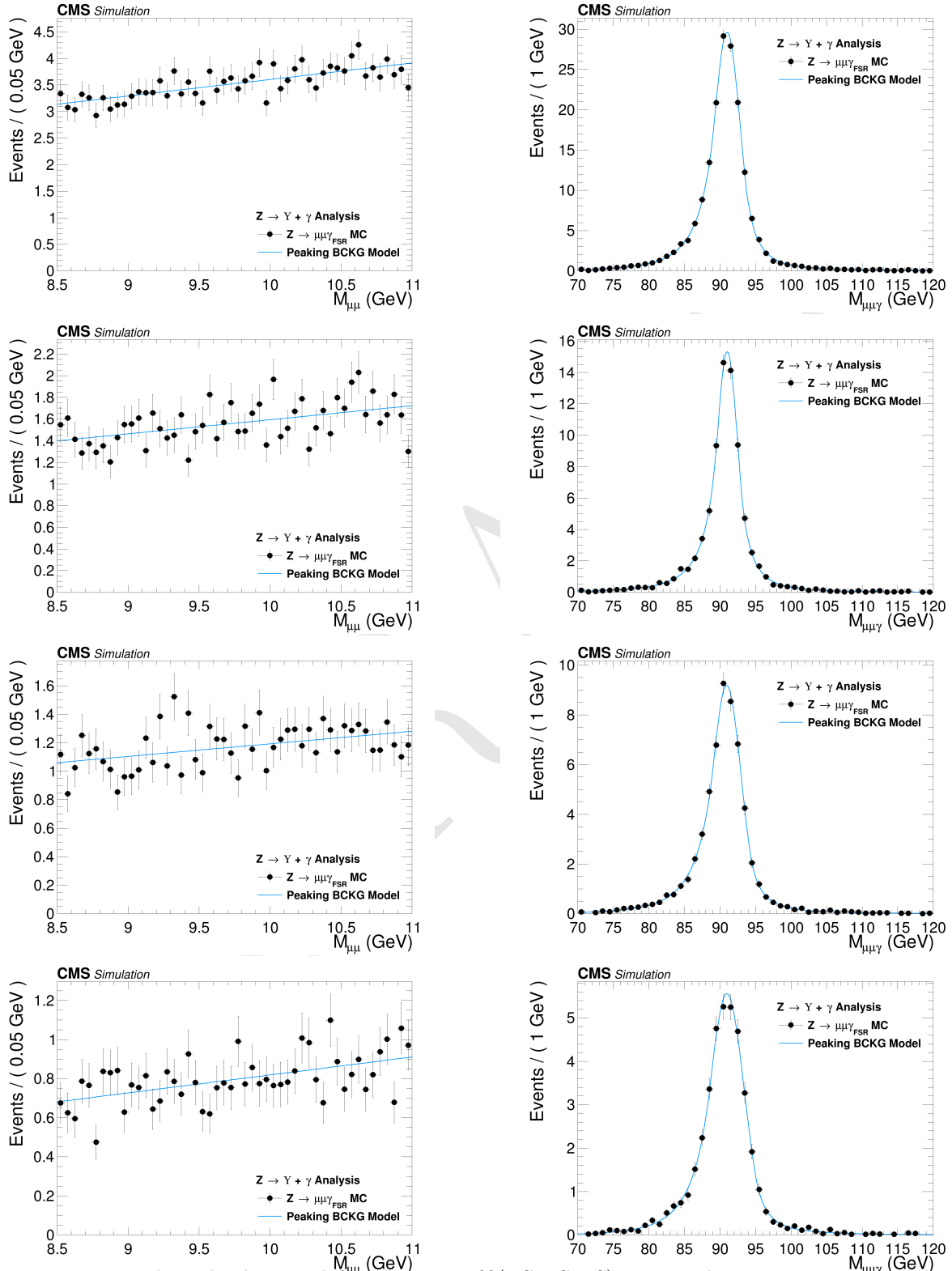


Figure 4.53: Peaking background for the $Z \rightarrow Y(1S, 2S, 3S) + \gamma$ analysis. $\mu\mu$ mass distribution (left) and $\mu\mu\gamma$ invariant mass distribution (right). From top to bottom categories: Inclusive, EB High R9, EB Low R9, EE.

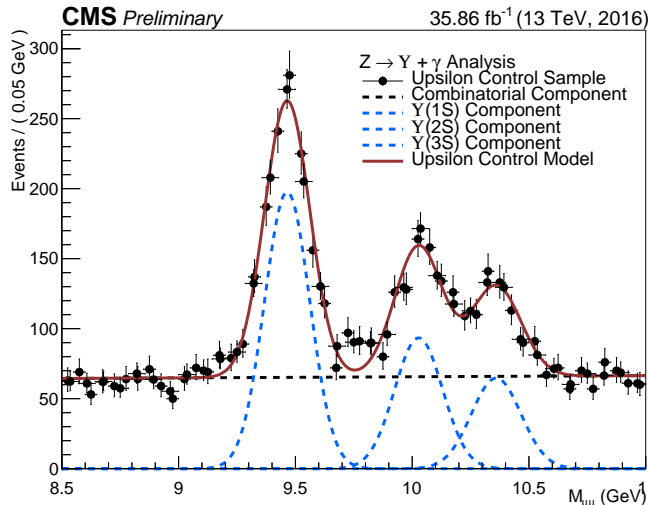


Figure 4.54: Υ control sample fit with Chebychev 1st order for the background support and 3 gaussian for the three $\Upsilon(1S, 2S, 3S)$ peaks.

- Sums of exponentials:

$$f_N(x) = \sum_{i=1}^N p_{2i} e^{p_{2i+1}x},$$

- Sums of polynomials (in the Bernstein basis):

$$f_N(x) = \sum_{i=0}^N p_i b_{(i,N)}, \text{ where } b_{(i,N)} := \binom{N}{i} x^i (1-x)^{N-i},$$

- Laurent series:

$$f_N(x) = \sum_{i=1}^N p_i x^{-4+\sum_{j=1}^i (-1)^j(j-1)},$$

- Sums of power-law functions:

$$f_N(x) = \sum_{i=1}^N p_{2i} x^{-p_{2i+1}},$$

⁹⁹⁷ where for all k , the p_k are a set of floating parameters in the fit.

⁹⁹⁸ Twice difference in the negative log-likelihood (NLL) between the N^{th} and the $(N+1)^{th}$ order of
⁹⁹⁹ the same polynomial ($\Delta NLL = 2 \times (NLL_N - NLL_{N+1})$) is expected to follow a χ^2 distribution
¹⁰⁰⁰ with M degrees of freedom, where M is the increase in degrees of freedom when going from N^{th} to
¹⁰⁰¹ $(N+1)^{th}$. This can be shown with the help of the Wilks' theorem [65].

¹⁰⁰² Starting from the lowest order possible, the best choice of order, for each family, is determined when
¹⁰⁰³ a increase in the order of the polynomial, does not brings a significant improvement in the quality
¹⁰⁰⁴ of the fit. Since a model with more fit parameters (higher order polynomials) will always perform,
¹⁰⁰⁵ if not the same, better than a simpler one, an optimal choice of the polynomial order, will be the
¹⁰⁰⁶ one right before the model becomes too flexible for the data.

1007 Consider a p -value defined as:

$$\begin{aligned} p\text{-value} &= \int_{\Delta NLL}^{\infty} \chi_M^2(\Delta) d\Delta \\ &= P(\chi_M^2 > \Delta NLL), \end{aligned} \quad (4.5)$$

1008 In the same spirit as the Wilks' theorem, this is the p -value for a likelihood ratio test between a
 1009 null hypotheses and an alternative model, where the null hypotheses is the N^{th} order and $(N+1)^{th}$
 1010 order is the alternative one.

$$\begin{aligned} \Delta NLL &= 2 \times (NLL_N - NLL_{N+1}) \\ &= -2 \times \log\left(\frac{\mathcal{L}_N}{\mathcal{L}_{N+1}}\right), \end{aligned} \quad (4.6)$$

1011 where \mathcal{L}_N is the likelihood for the N^{th} polynomial order.

1012 The alternative will present a statistically significant improvement, with respect to the null hypothe-
 1013 ses, if the p -value is smaller than 0.05, since the probability of obtaining, by chance, considering
 1014 the null hypotheses is true, a even higher ΔNLL is less than 5%. This will give support to chose
 1015 $(N+1)^{th}$ over N^{th} .

1016 If the p -value is greater than 0.05 a higher order is not supported, since the probability of obtaining
 1017 a ΔNLL greater than the one observed is statistically significant (more than 5%). A higher ΔNLL
 1018 means that another data sample, collected and analyzed with strictly the same conditions, would
 1019 have a probability of more than 5% of giving a better fit improvement than the one observed,
 1020 again assuming that the null hypotheses is true. This is an indication of overfitting, since the
 1021 improvements are likely to come from just statistical fluctuations. When testing the $(N+1)^{th}$ order
 1022 and this condition is reached, the optimal order should be the N^{th} .

1023 At first, before any fit to data, the 2-Dimensional model is composed by the five components, as
 1024 described in Table 4.6 (in which the $m_{\mu\mu\gamma}$ modeling for the Full Combinatorial Background and the
 1025 Υ combinatorial are shared), then, the statistical test described before is ran for each family. It is
 1026 important to stress that before the statistical test all the other fitting parameters have been fixed.
 1027 This leaves only the normalizations of the model components and the polynomial coefficients free
 1028 to float.

1029 Once the optimal order for each pdf family is obtained, the composed pdf with each choice from
 1030 statistical test is saved in the same model, providing a discrete variable that indexes the different
 1031 polynomial pdf families. This method is called Discrete Profiling (or "*Envelope Method*") and it
 1032 allows the analysis algorithm to treat the choice of the pdf as a systematics and incorporate its
 1033 effect in the extracted upper limits. This model, with different choices of polynomial families is
 1034 called envelope.

1035 The implementation, used in the analysis, of the statistical test and the Discrete Profiling is based
 1036 on the same algorithm used by the $H \rightarrow \gamma\gamma$ Run II analysis. An extensive documentation on these
 1037 methods can be found in $H \rightarrow \gamma\gamma$ analysis note and physics analysis summary [66, 67] and in the
 1038 specific reference of the Discrete Profiling [64]. The figures 4.55 and 4.56 show the projection for
 1039 the $\mu\mu$ and $\mu\mu\gamma$ distribution after the statistical test.

1040 For the $H \rightarrow \Upsilon(1S, 2S, 3S) + \gamma$ analysis, the same procedure is implemented, except for the peaking
 1041 background modeling. Since the MC prediction for the contribution of the background is too small,

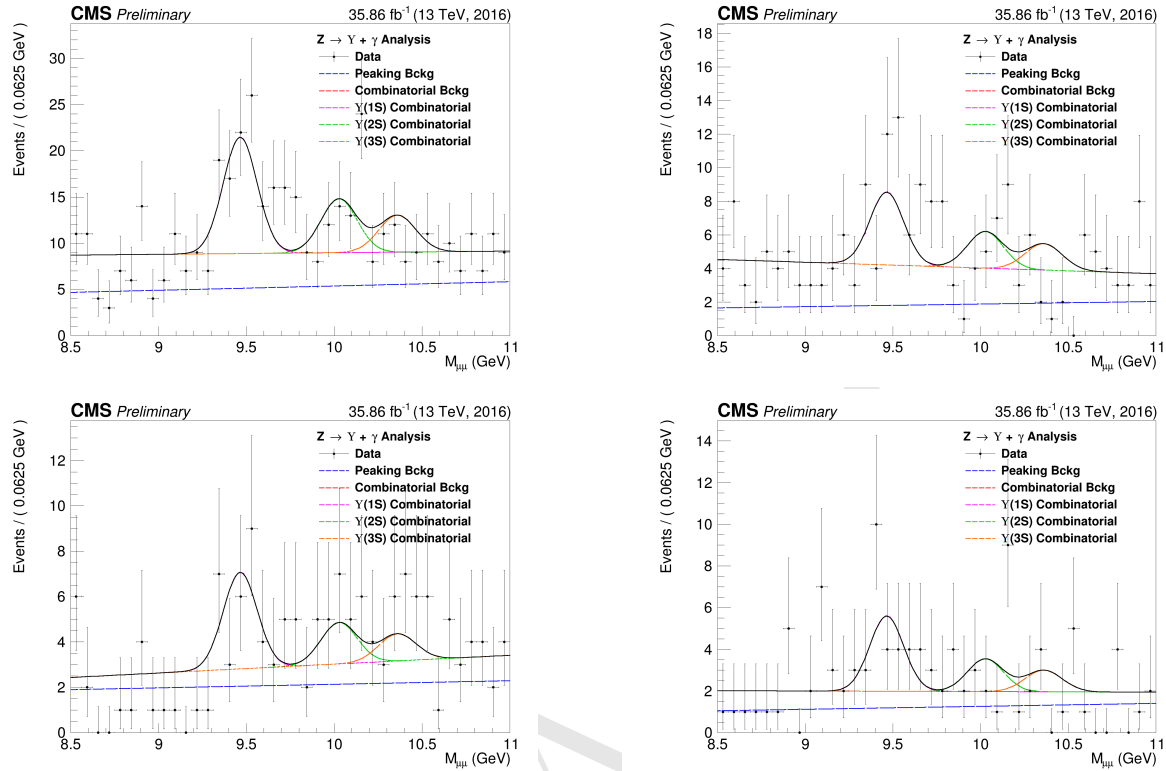


Figure 4.55: $Z \rightarrow \Upsilon(1S, 2S, 3S) + \gamma$ Background Modeling: $\mu\mu$ distribution. Inclusive (top left); EB High R9 (top right), EB Low R9 (bottom left), EE (bottom right). The pdfs projections are plotted with respect to the overall best choice of the statistica test.

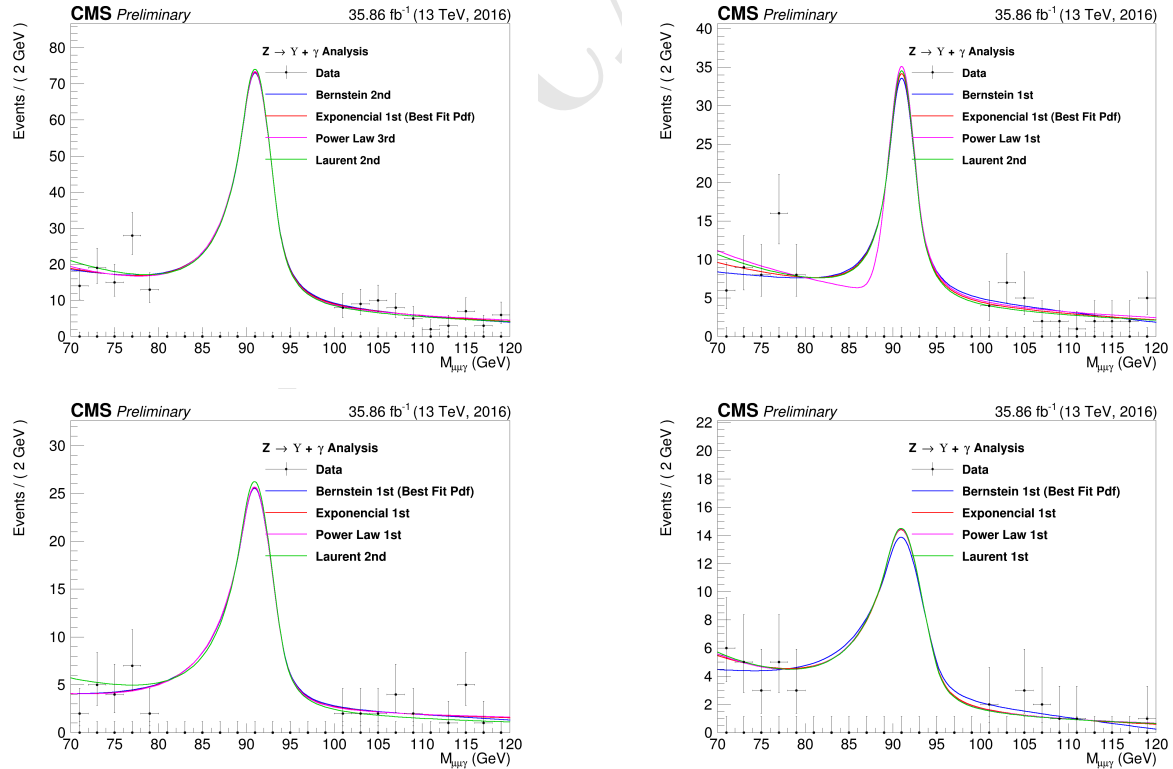


Figure 4.56: $Z \rightarrow \Upsilon(1S, 2S, 3S) + \gamma$ Background Modeling: $\mu\mu\gamma$ distribution. Inclusive (top left); EB High R9 (top right), EB Low R9 (bottom left), EE (bottom right). The plotted pdfs corresponds to the best choice by the statistical test for each family. The signal region, from 80 GeV to 100 GeV was blinded.

according to the comparison between the final selected events for data and the Higgs Dalitz Decay sample, in order to avoid fitting over statistical fluctuations of the data sample, the Peaking Background, for the Higgs channel, is fully modeled from the MC sample, including its normalization, as shown in figure 4.57, hence it is not included the the statistical test, neither in the final background modeling envelope.

The results of the background modeling for the Full Combinatorial and Υ Combinatorial, can be found at Figures 4.58 and 4.59, for the $\mu\mu$ and $\mu\mu\gamma$ distribution, respectively. It is worth to remember that, for the Higgs channel, we are not implementing any categorization.

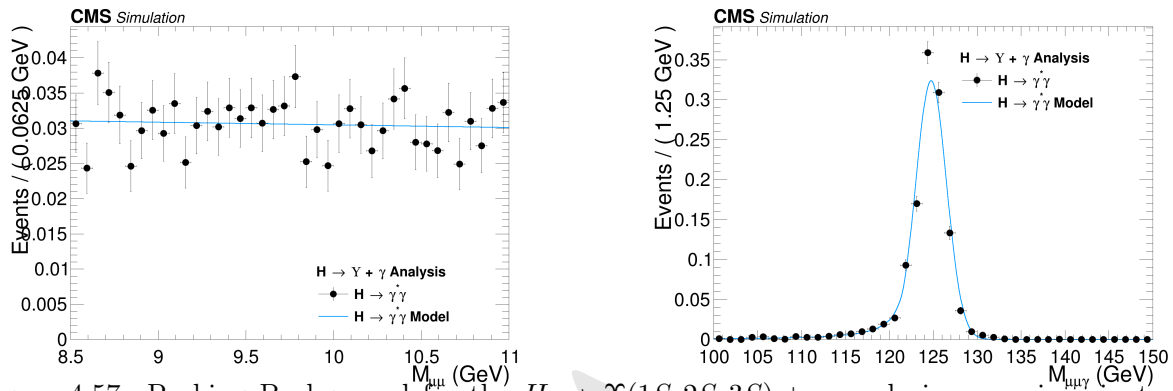


Figure 4.57: Peaking Background for the $H \rightarrow \Upsilon(1S, 2S, 3S) + \gamma$ analysis. $m_{\mu\mu}$ invariant mass distribution (left) and $m_{\mu\mu\gamma}$ invariant mass distribution (right).

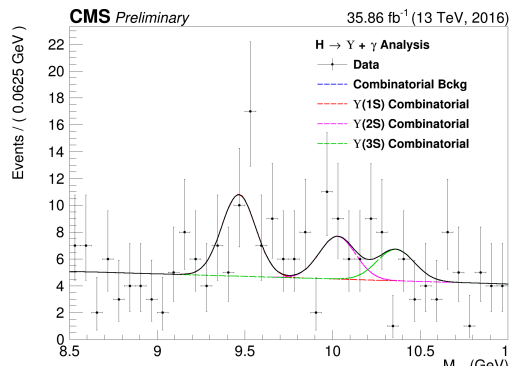


Figure 4.58: $H \rightarrow \Upsilon(1S, 2S, 3S) + \gamma$ Background Modeling: $m_{\mu\mu}$ distribution. The $pdfs$ projections are plotted with respect to the overall best choice of the statistical test.

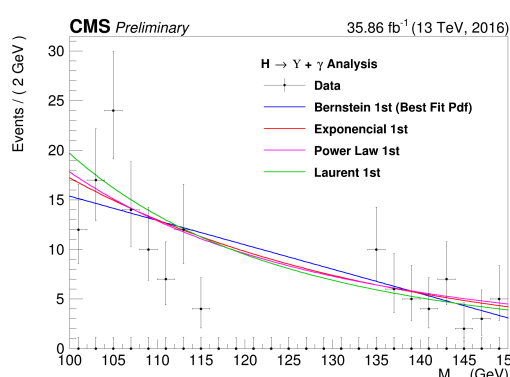


Figure 4.59: $H \rightarrow \Upsilon(1S, 2S, 3S) + \gamma$ Background Modeling: $\mu\mu\gamma$ distribution. The plotted $pdfs$ corresponds to the best choice by the statistical test for each family. The signal region, from 115 GeV to 135 GeV was blinded.

1050 **4.9 Signal modeling**

1051 Along the same lines as the background modeling (Section 4.8), the signal modeling is implemented
 1052 as a two dimensional unbinned maximum likelihood fit on the $m_{\mu\mu}$ and the $m_{\mu\mu\gamma}$ invariant masses
 1053 distributions, but this time, only using the signal simulated MC samples 4.1.2. Since, for the two
 1054 spectra, it is expected a peak-like distribution, one centered in the Z (or Higgs) boson mass and the
 1055 other centered in the Υ mass, two also peak-like analytics *pdfs* were chosen to compose the signal
 1056 model. The modeling is summarized in table 4.7.

Table 4.7: Modeling for each signal source and mass component.

| | $m_{\mu\mu}$ | $m_{\mu\mu\gamma}$ |
|---|---------------------|--|
| $Z \rightarrow \Upsilon(1S, 2S, 3S) + \gamma$ | Double Crystal Ball | Double Crystal Ball |
| $H \rightarrow \Upsilon(1S, 2S, 3S) + \gamma$ | Double Crystal Ball | Crystal Ball + Gaussian with the same mean |

1057 The projections of the modeling for the Z boson decay channel analysis can be found at figures 4.60,
 1058 4.61, 4.62 and 4.63, for Inclusive, EB High R9, EB Low R9 and EE, respectively. The projection
 1059 on the modeling for the Higgs boson signal can be found at Figure 4.64. A deeper discussion on the
 1060 systematics uncertainties associated to them, will be presented in the next section.

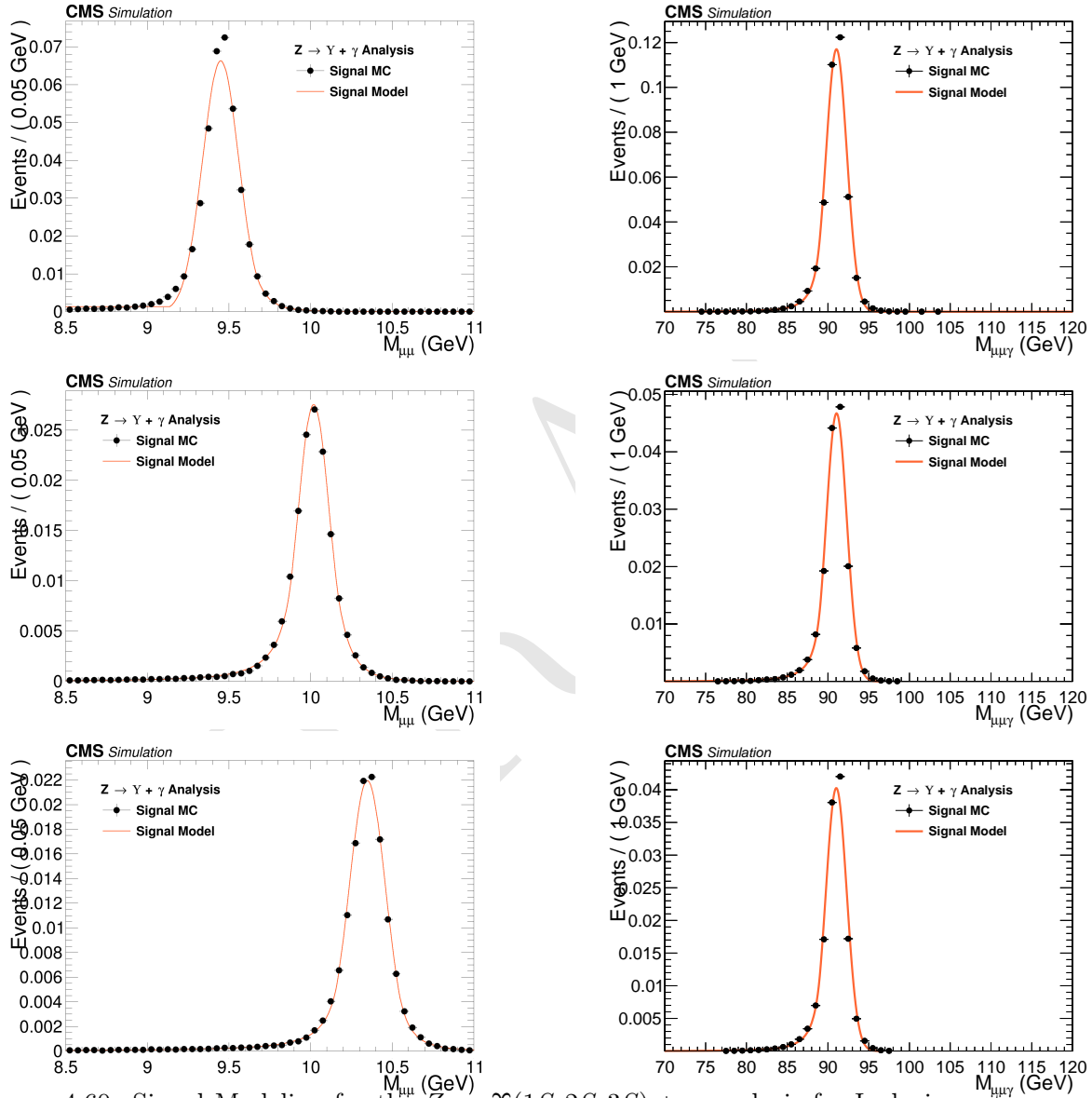


Figure 4.60: Signal Modeling for the $Z \rightarrow \Upsilon(1S, 2S, 3S) + \gamma$ analysis for Inclusive category. $m_{\mu\mu}$ mass distribution (left) and $m_{\mu\mu\gamma}$ mass distribution (right). From top to bottom: $\Upsilon(1S)$, $\Upsilon(2S)$, $\Upsilon(3S)$.

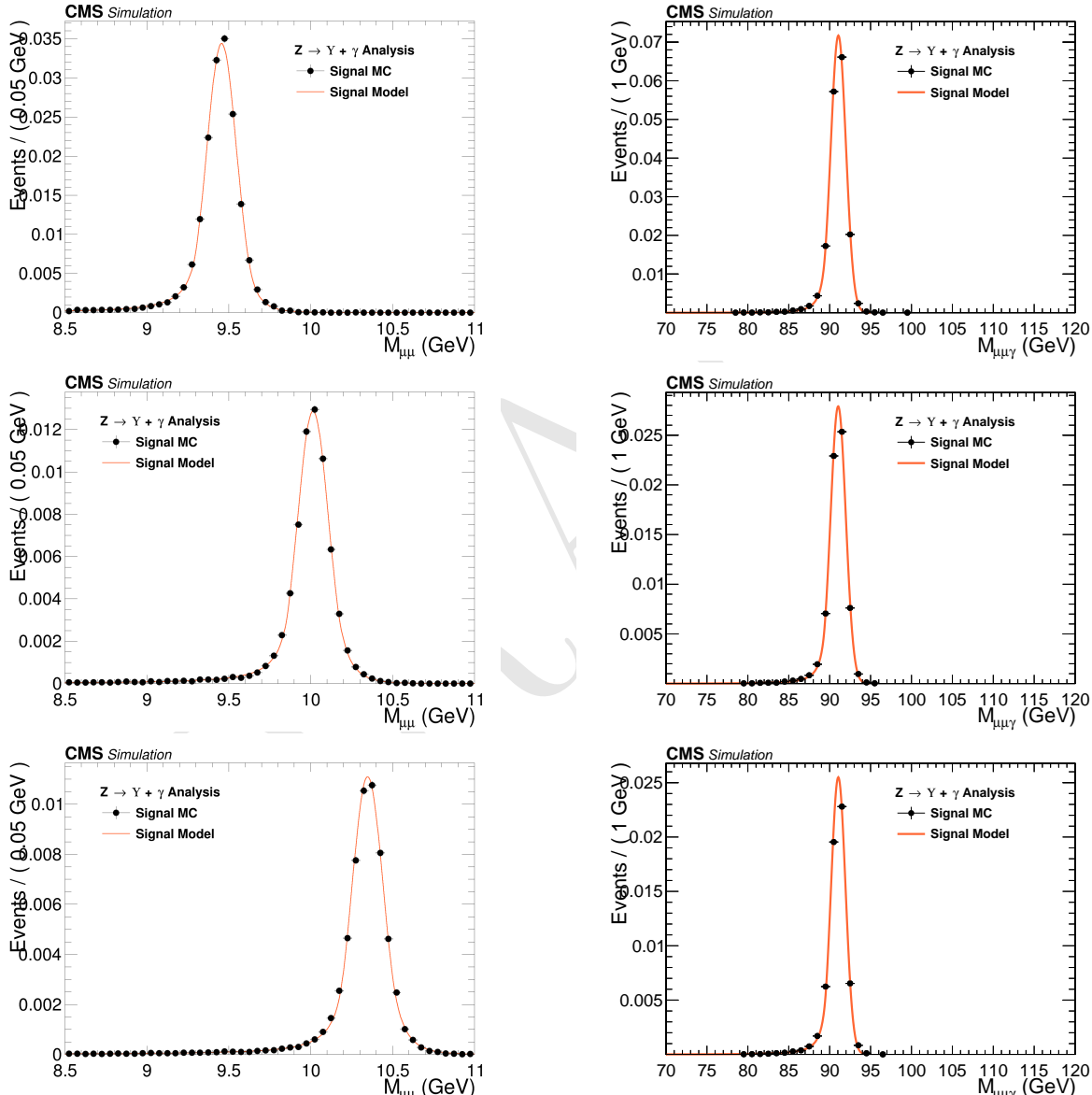


Figure 4.61: Signal Modeling for the $Z \rightarrow \Upsilon(1S, 2S, 3S) + \gamma$ analysis for EB High R9 category. $m_{\mu\mu}$ mass distribution (left) and $m_{\mu\mu\gamma}$ mass distribution (right). From top to bottom: $\Upsilon(1S)$, $\Upsilon(2S)$, $\Upsilon(3S)$.

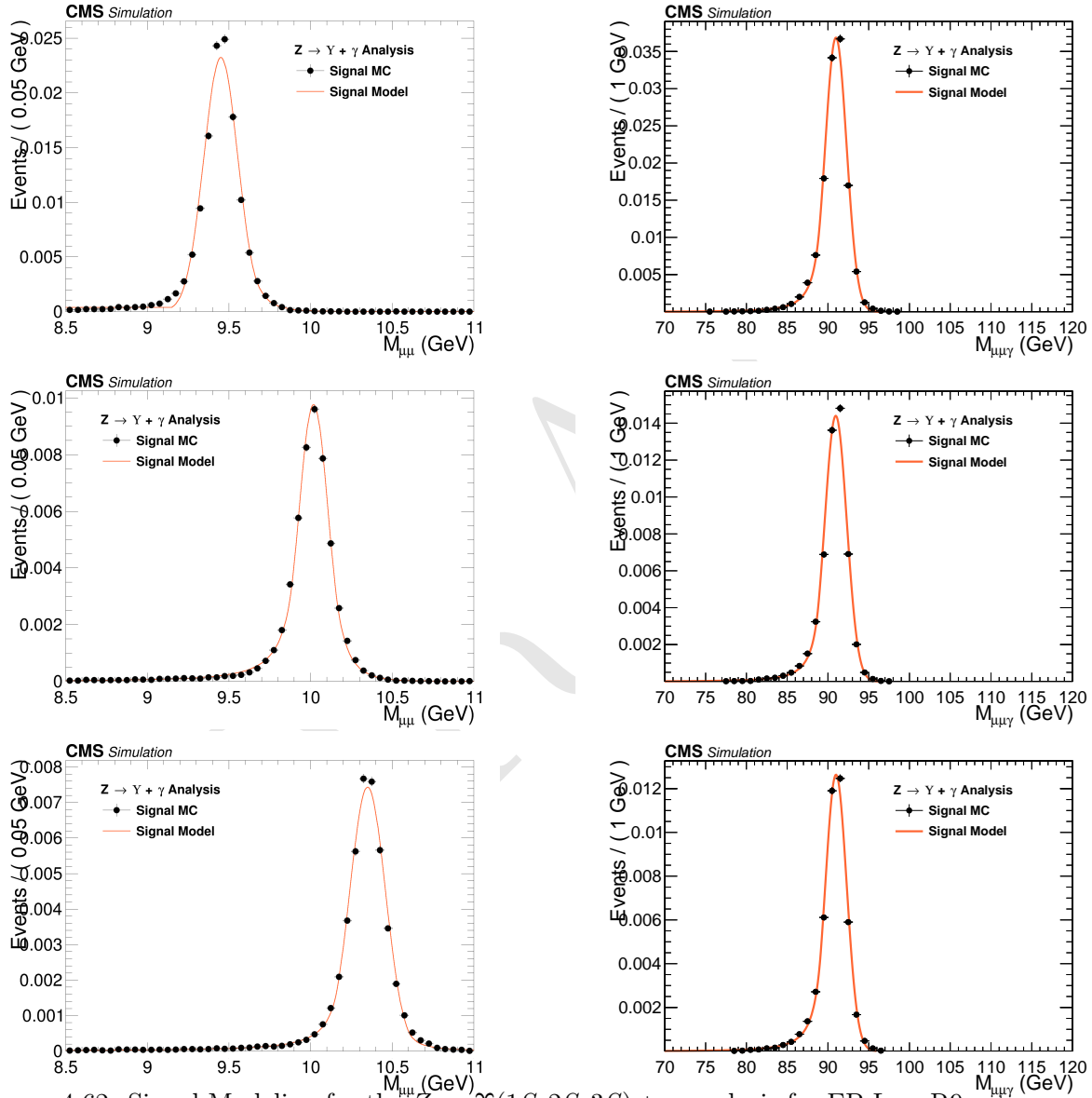


Figure 4.62: Signal Modeling for the $Z \rightarrow \Upsilon(1S, 2S, 3S) + \gamma$ analysis for EB Low R9 category. $m_{\mu\mu}$ mass distribution (left) and $m_{\mu\mu\gamma}$ mass distribution (right). From top to bottom: $\Upsilon(1S)$, $\Upsilon(2S)$, $\Upsilon(3S)$.

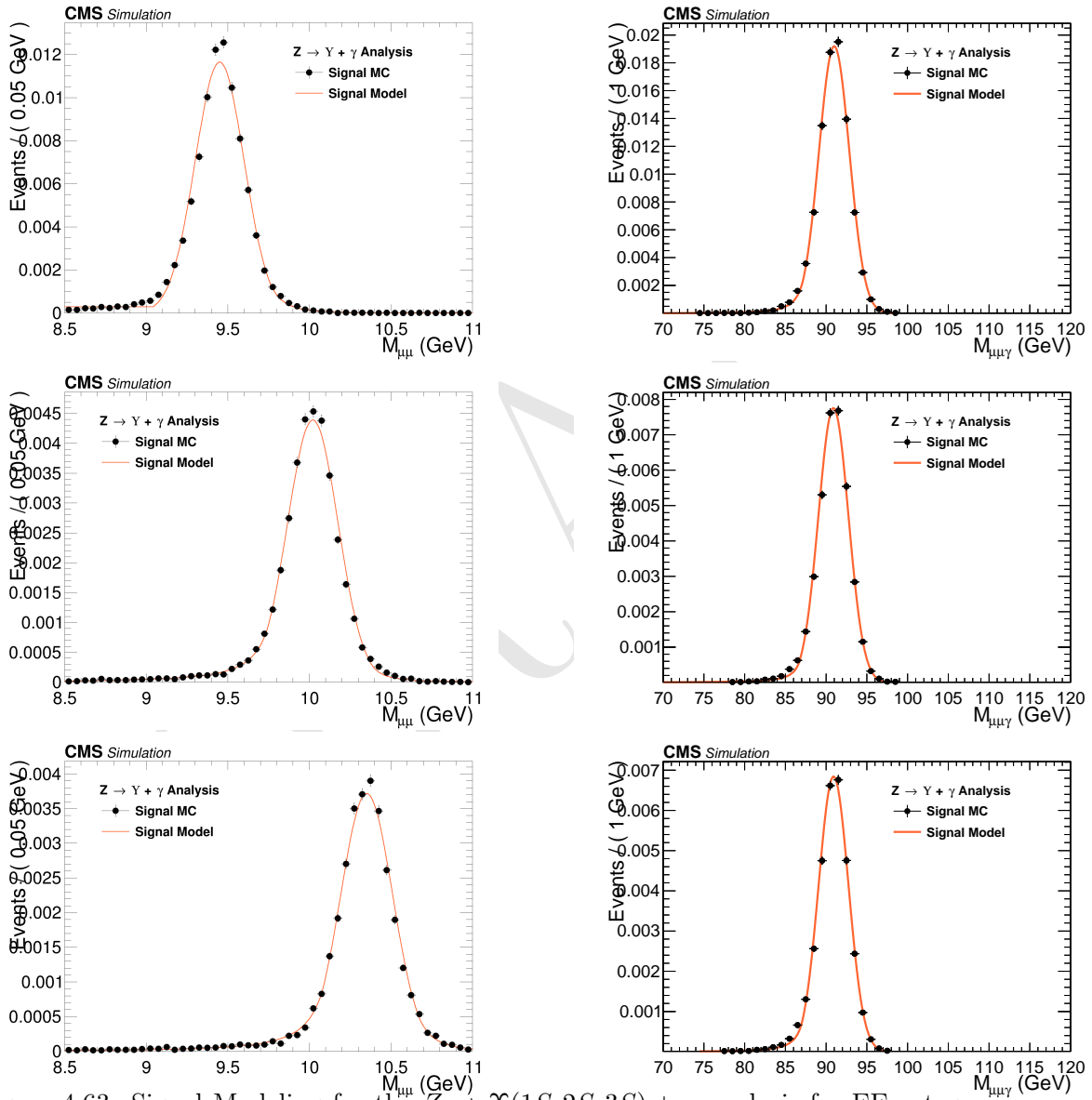


Figure 4.63: Signal Modeling for the $Z \rightarrow \Upsilon(1S, 2S, 3S) + \gamma$ analysis for EE category. $m_{\mu\mu}$ mass distribution (left) and $m_{\mu\mu\gamma}$ mass distribution (right). From top to bottom: $\Upsilon(1S)$, $\Upsilon(2S)$, $\Upsilon(3S)$.

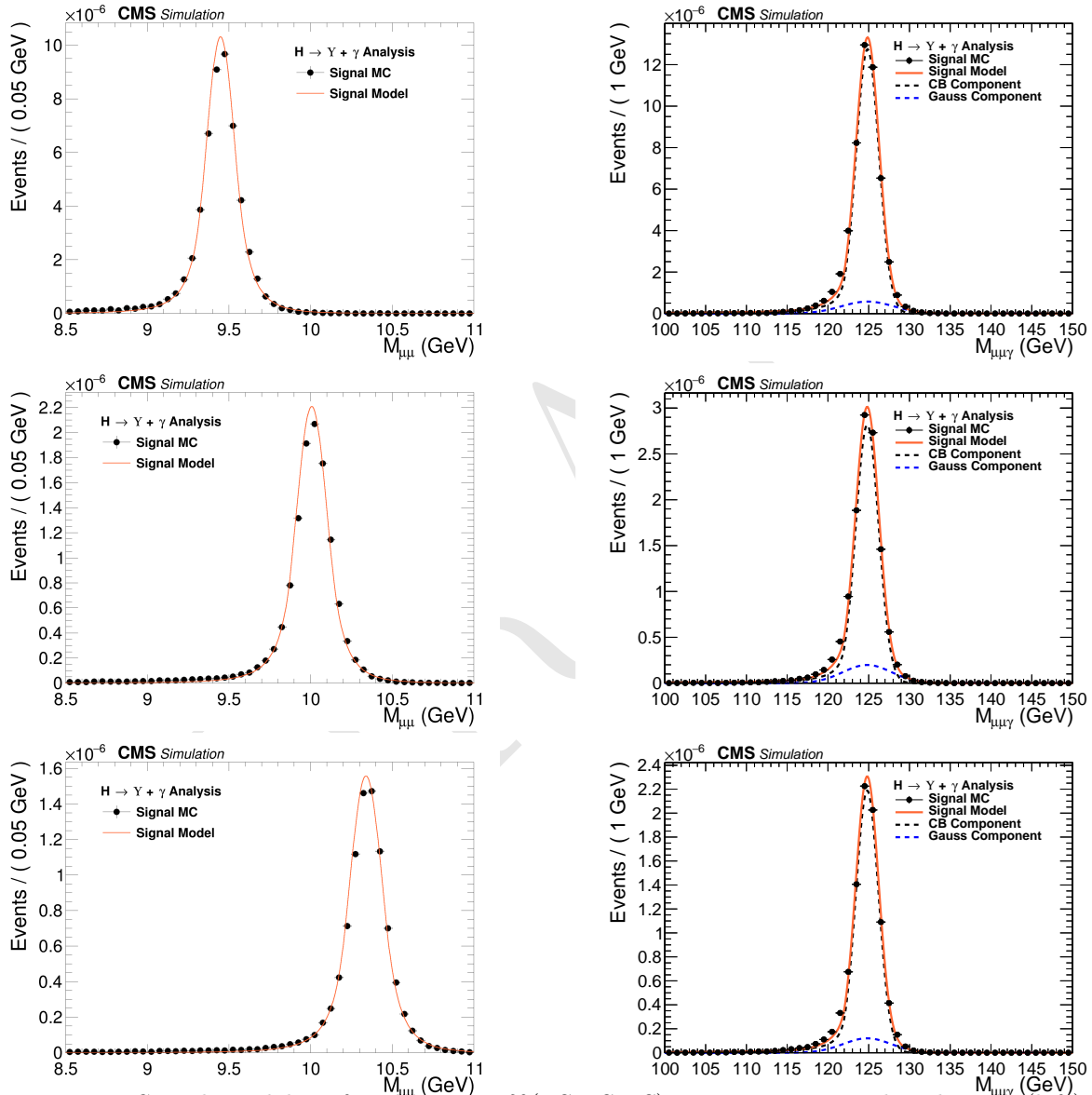


Figure 4.64: Signal Modeling for the $H \rightarrow \Upsilon(1S, 2S, 3S) + \gamma$. $m_{\mu\mu}$ mass distribution (left) and $m_{\mu\mu\gamma}$ mass distribution (right). From top to bottom: $\Upsilon(1S)$, $\Upsilon(2S)$, $\Upsilon(3S)$.

1061 4.10 Systematic uncertainties

- 1062 Two sources of systematics are considered: the ones that affect the predicted yields⁸ and the ones
 1063 that affect the shape of the pdfs used to compose the signal and background model.
- 1064 Those that affect the predicted yields, presented in Section 4.7.2, it is considered integrated lumi-
 1065 nosity measurement [39], the pile-up description in the Monte-Carlo simulations, the corrections
 1066 applied to the simulated events in order to compensate for the differences in performance of the
 1067 some selection criteria, such as trigger, object reconstruction and identification, the Υ polarization
 1068 and the theoretical uncertainties, such as the effects of the *parton density functions* (PDF) to the
 1069 signal cross section [9, 48, 68], the variations of the renormalization and factorization scales [69–73],
 1070 and the prediction of the decay branching ratios.
- 1071 For the systematics on the signal modeling, it is considered possible imprecisions of the momentum
 1072 scale and resolution. They are measured on how they affect the mean (μ) and the standard deviation
 1073 (σ) of the signal model. For the background modeling, since it is derived from data, the choice of
 1074 the *pdf* (Probability distribution function) is the only systematic uncertainties considered. It is
 1075 treated by the Discrete Profiling method, as described in section 4.8.
- 1076 The two kinds of systematics uncertainties are described in details below.

1077 4.10.1 Uncertainties on the predicted yields

- 1078 The theoretical sources of uncertainties includes: parton distribution functions uncertainties, strong
 1079 coupling constant (α_s) uncertainty and uncertainty on the $H \rightarrow \gamma\gamma$ branching fraction (used to derive
 1080 the Higgs Dalitz Decays cross-section). The values for these theoretical uncertainties are taken from
 1081 the Higgs Combination Group [51] and also from [72, 74].
- 1082 An uncertainty value of 2.5% is used on the integrated luminosity of the data samples, as recom-
 1083 mended by CMS [39]. To evaluate the impact of the pile-up reweighting in the final result, the
 1084 The total inelastic cross section of 69.2 mb is varied by $\pm 4.6\%$ and the analysis is ran with these
 1085 extreme values. The systematic uncertainty quoted is the maximum difference in the yields with
 1086 respect to nominal value, as recommended by CMS.
- 1087 The impact of the trigger scale factor is evaluated by running this analysis with $\pm 1\sigma$ on the
 1088 Trigger Efficiency Scale factors (section 4.5.1). The systematic uncertainty quoted is the maximum
 1089 difference in the yields with respect to nominal value.
- 1090 For the final state object identification and isolation associated uncertainty, the scale factors, pro-
 1091 vided by CMS, to match the performance of MC and Data samples are varied in $\pm 1\sigma$. The
 1092 systematic uncertainty quoted is the maximum difference in the yields with respect to nominal
 1093 value. This procedure is applied on the scale factors for the Photon MVA ID and the Electron Veto
 1094 (section 4.5.3) and for Muon Identification and Isolation(section 4.5.2).
- 1095 Finally, the Υ Polarization is assessed applying the extremes scenarios of the Υ polarization (Trans-
 1096 verse and Longitudinal Polarization to the signal samples (section 4.2). The systematic uncertainty
 1097 quoted is the maximum difference in the yields with respect to nominal (Unpolarized) yield. This
 1098 procedure is applied only for the Z decay. For the Higgs decay, the only polarization considered is
 1099 the transverse polarization.
- 1100 The effect of all systematic uncertainties in the signal and peaking background yields are summarized
 1101 on table 4.8, for the Z decay and table 4.9, for the Higgs decay. Clearly, the main contribution to the

⁸Number of events, per process, after full selection and corrected by the expected SM cross sections.

systematics uncertainties on the yields is Polarization of the $\Upsilon(nS)$ (only for the Z decay), around 15%.

4.10.2 Uncertainties that affect the signal fits

Smearing and scaling corrections are applied on simulated events since the resolution of Monte Carlo is better than that on data and the detector might not catch all the possible differences in the detector performance, with respect to the data observation. They need to be estimated and included on the systematics. The corrections are:

- **Muon Momentum Scale and Resolution:** extracted by running the analysis with different setups of the official CMS Muon scaling and smearing package [75]. The deviations, with respect to the default correction are summed in quadrature. Once the nominal parameters (mean or sigma) are obtained, the default corrections are shifted by $\pm 1\sigma$ and the fits are re-done, with the parameters of interest free to float and all others fixed. The systematic uncertainty quoted is the maximum difference of the parameter with respect to nominal value.
- **Photon Energy Scale and Resolution:** extracted by running the analysis with different sets of corrections, provided by the CMS ⁹. Once the nominal mean is obtained, the sets are changed and the fits are re-done, with the mean free to float and all others parameters fixed. The corrections are shifted by $\pm 1\sigma$ on each source of systematics (following standard CMS recommendations). The quoted as systematic uncertainty is the quadrature sum of the maximum deviation within each set.

The effective systematic uncertainty associated with the scale and resolution are the quadrature sum of the muon and photon contributions. The effect of all systematic uncertainties in the Signal fits are summarized on table 4.10, for the Z and Higgs decay.

⁹CMS has not published, yet, a paper on the Run2 performance of the Photon reconstruction (This document is under internal review process.). Just as a reference, we cite the Run1 paper [76].

Table 4.8: A summary table of systematic uncertainties in the Z boson decaying in $\Upsilon(1S, 2S, 3S) + \gamma$, affecting the final yields of the MC samples.

| Source | Uncertainty | | | |
|---|------------------------------------|------------------------------------|------------------------------------|------------------------------------|
| | Signal | | Peaking Background | |
| | $Z \rightarrow \Upsilon(1S)\gamma$ | $Z \rightarrow \Upsilon(2S)\gamma$ | $Z \rightarrow \Upsilon(3S)\gamma$ | $Z \rightarrow \mu\mu\gamma_{FSR}$ |
| Integrated luminosity | | | | |
| All Categories | 2.5% | | | |
| SM Z boson σ (scale) | | | | |
| All Categories | 3.5% | | 5.0% | |
| SM Z boson σ (PDF + α_s) | | | | |
| All Categories | 1.73% | | 5.0% | |
| Pileup Reweighting | | | | |
| Inclusive | 0.65% | 0.68% | 0.71% | 0.62% |
| EB High R9 | 1.01% | 1.1% | 1.04% | 1.06% |
| EB Low R9 | 0.17% | 0.08% | 0.13% | 0.11% |
| EE | 1.07% | 0.98% | 1.26% | 0.78% |
| Trigger | | | | |
| Inclusive | 4.45% | 4.46% | 4.49% | 4.71% |
| EB High R9 | 3.5% | 3.5% | 3.52% | 3.71% |
| EB Low R9 | 3.55% | 3.54% | 3.58% | 3.72% |
| EE | 7.52% | 7.58% | 7.56% | 8.13% |
| Muon Identification | | | | |
| Inclusive | 4.82% | 4.81% | 4.8% | 4.52% |
| EB High R9 | 4.45% | 4.45% | 4.44% | 4.2% |
| EB Low R9 | 4.65% | 4.62% | 4.63% | 4.32% |
| EE | 5.75% | 5.75% | 5.74% | 5.44% |
| Photon Identification | | | | |
| Inclusive | 1.1% | 1.1% | 1.09% | 1.09% |
| EB High R9 | 1.1% | 1.09% | 1.09% | 1.11% |
| EB Low R9 | 1.1% | 1.1% | 1.09% | 1.08% |
| EE | 1.1% | 1.1% | 1.1% | 1.09% |
| Electron Veto | | | | |
| Inclusive | 1.02% | 1.02% | 1.02% | 1.03% |
| EB High R9 | 1.2% | 1.2% | 1.2% | 1.2% |
| EB Low R9 | 1.2% | 1.2% | 1.2% | 1.2% |
| EE | 0.45% | 0.45% | 0.45% | 0.45% |
| Polarization | | | | |
| Inclusive | 15.36% | 14.78% | 14.84% | - |
| EB High R9 | 15.6% | 14.88% | 14.87% | - |
| EB Low R9 | 15.01% | 14.31% | 14.4% | - |
| EE | 15.39% | 15.27% | 15.39% | - |

Table 4.9: A summary table of systematic uncertainties in the Higgs boson decaying in $\Upsilon(1S, 2S, 3S) + \gamma$, affecting the final yields of the MC samples.

| Source | Uncertainty | | | |
|---------------------------------------|------------------------------------|------------------------------------|------------------------------------|--------------------------------|
| | Signal | | | Peaking Background |
| | $H \rightarrow \Upsilon(1S)\gamma$ | $H \rightarrow \Upsilon(2S)\gamma$ | $H \rightarrow \Upsilon(3S)\gamma$ | $H \rightarrow \gamma\gamma^*$ |
| Integrated luminosity | | | 2.5% | |
| SM Higgs σ (scale) | | | +4.6% / -6.7% | |
| SM Higgs σ (PDF + α_s) | | | 3.2% | |
| SM BR $H \rightarrow \gamma\gamma^*$ | | - | | 6.0% |
| Pileup Reweighting | 0.61% | 0.68% | 0.56% | 0.9% |
| Trigger | 5.61% | 5.47% | 5.5% | 6.12% |
| Muon Identification | 4.39% | 4.36% | 4.34% | 4.33% |
| Photon Identification | 1.21% | 1.22% | 1.22% | 1.2% |
| Electron Veto | 1.04% | 1.04% | 1.04% | 1.04% |

Table 4.10: A summary table of systematic uncertainties in the Z (H) decaying in $\Upsilon(1S, 2S, 3S) + \gamma$, affecting the signal fits.

| | Z $\rightarrow \Upsilon(nS) + \gamma$ | | | | H $\rightarrow \Upsilon(nS) + \gamma$ |
|---------------------------|---------------------------------------|------------|-----------|-------|---------------------------------------|
| | Inclusive | EB High R9 | EB Low R9 | EE | Inclusive |
| Mean - Scale | | | | | |
| $\Upsilon(1S)$ | Muon Unc. | 0.06% | 0.05% | 0.06% | 0.11% |
| | Photon Unc. | 0.21% | 0.13% | 0.19% | 0.26% |
| | Total Unc. | 0.22% | 0.14% | 0.2% | 0.28% |
| Sigma - Resolution | | | | | |
| | Muon Unc. | 1.12% | 0.84% | 1.55% | 1.14% |
| | Photon Unc. | 2.14% | 2.48% | 1.95% | 2.79% |
| | Total Unc. | 2.42% | 2.61% | 2.49% | 3.01% |
| Mean - Scale | | | | | |
| $\Upsilon(2S)$ | Muon Unc. | 0.07% | 0.05% | 0.06% | 0.13% |
| | Photon Unc. | 0.25% | 0.11% | 0.2% | 0.19% |
| | Total Unc. | 0.26% | 0.12% | 0.21% | 0.23% |
| Sigma - Resolution | | | | | |
| | Muon Unc. | 1.21% | 1.54% | 2.65% | 1.66% |
| | Photon Unc. | 1.85% | 2.67% | 3.56% | 3.6% |
| | Total Unc. | 2.21% | 3.08% | 4.44% | 3.97% |
| Mean - Scale | | | | | |
| $\Upsilon(3S)$ | Muon Unc. | 0.06% | 0.06% | 0.06% | 0.09% |
| | Photon Unc. | 0.22% | 0.14% | 0.25% | 0.17% |
| | Total Unc. | 0.23% | 0.15% | 0.26% | 0.19% |
| Sigma - Resolution | | | | | |
| | Muon Unc. | 1.78% | 2.38% | 2.1% | 2.25% |
| | Photon Unc. | 2.51% | 4.14% | 2.23% | 4.08% |
| | Total Unc. | 3.08% | 4.77% | 3.07% | 4.66% |

4.11 Modeling Cross checks

In order to test the applicability of the statistical (signal and background) modeling proposed in this study, a cross-check procedure is performed by generating a set of pseudo-experiments (toys datasets) based on the signal plus background model, for each decay channel ($H/Z \rightarrow \Upsilon(1S, 2S, 3S,) + \gamma$) with some signal injected.

The procedure consists of resample from the signal plus background a number of events, including some extra (injected signal). The amount of injected signal is controlled by the μ_{true} variable, where $\mu_{true} = X$ means inject X times the expected signal.

Once generated, the toy dataset is refitted to the signal plus background model and the signal strength (μ_{fit}) and its error σ_{fit} are extracted. This procedure is repeated 10000 times and only for the inclusive category. Figures 4.66, 4.65, 4.68 and 4.67 show examples of those fits for the Higgs and Z decay.

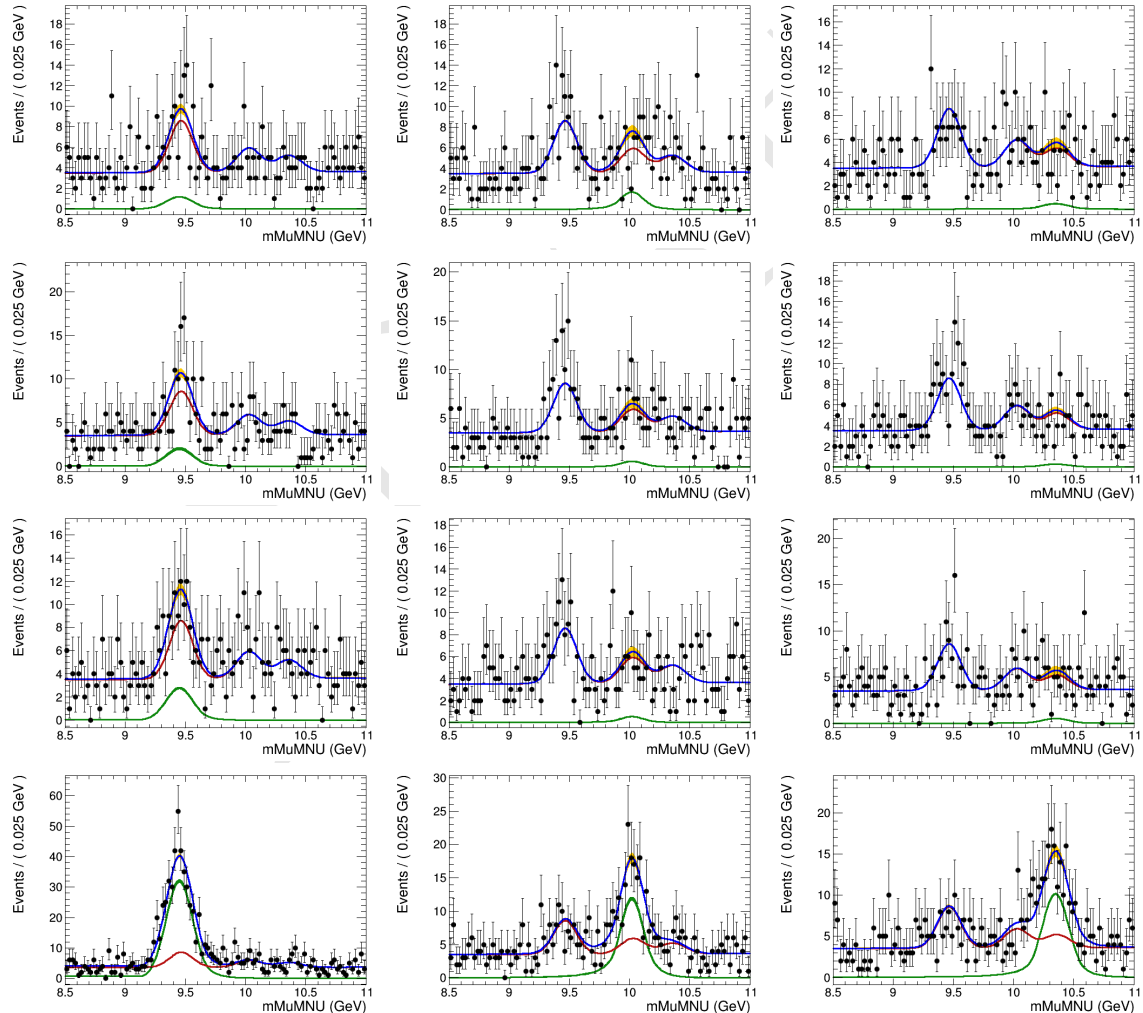


Figure 4.65: Examples of the toy datasets fit ($M_{\mu\mu}$), for the Z decay analysis, after the toy dataset refit, for 1S, 2S and 3S (left to right), with μ_{true} equals to 20, 50, 100, 1000 (top to bottom). The red lines corresponds to the background model (B), the green lines to signal model (S), the blue lines to the total (S+B) and the dots is the toy dataset.

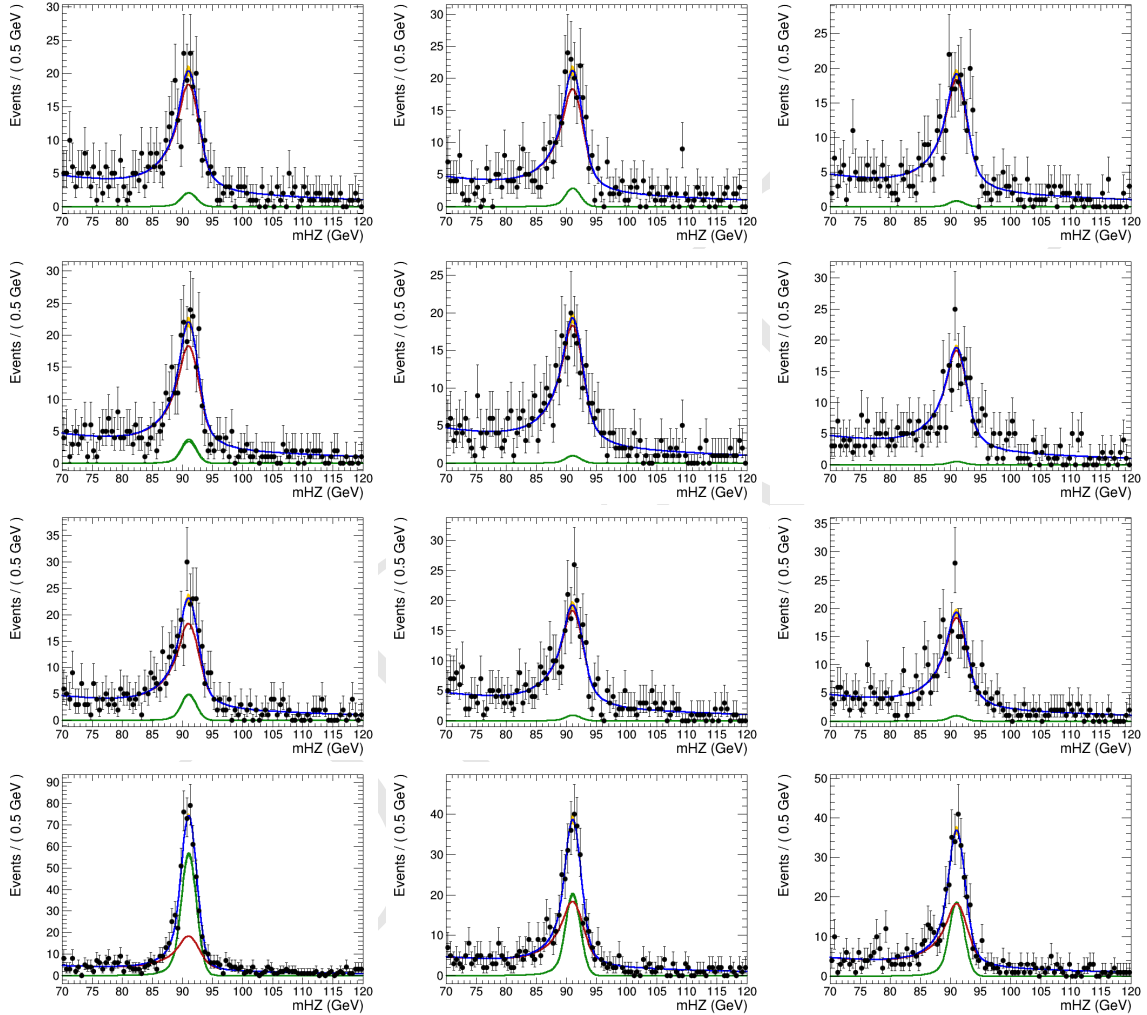


Figure 4.66: Examples of the toy datasets fit ($M_{\mu\mu\gamma}$), for the Z decay analysis, after the toy dataset refit, for 1S, 2S and 3S (left to right), with μ_{true} equals to 20, 50, 100, 1000 (top to bottom). The red lines corresponds to the background model (B), the green lines to signal model (S), the blue lines to the total (S+B) and the dots is the toy dataset.

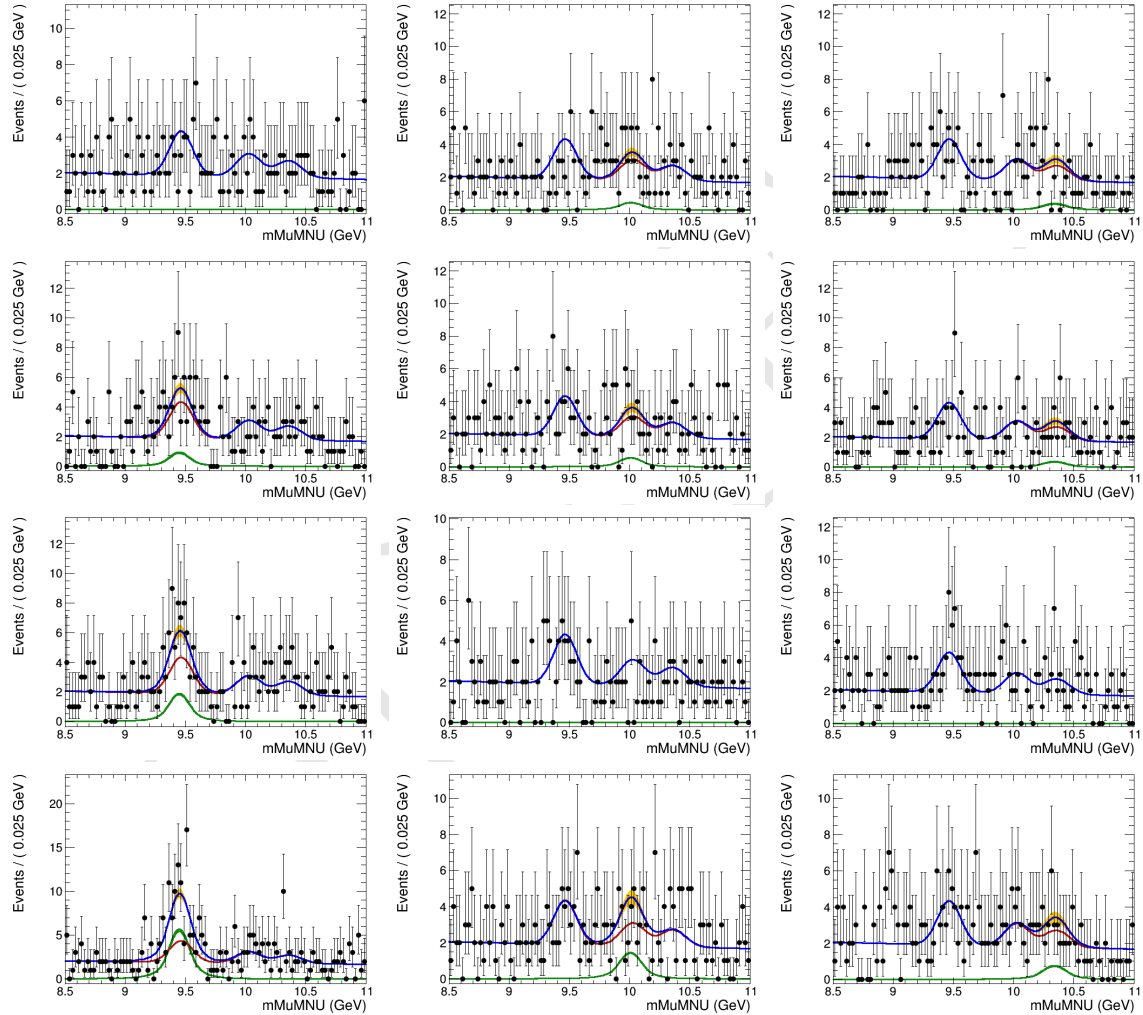


Figure 4.67: Examples of the toy datasets fit ($M_{\mu\mu}$), for the Higgs decay analysis, after the toy dataset refit, for 1S, 2S and 3S (left to right), with μ_{true} equals to 100000, 200000, 300000, 1000000 (top to bottom). The red lines corresponds to the background model (B), the green lines to signal model (S), the blue lines to the total (S+B) and the dots is the toy dataset.

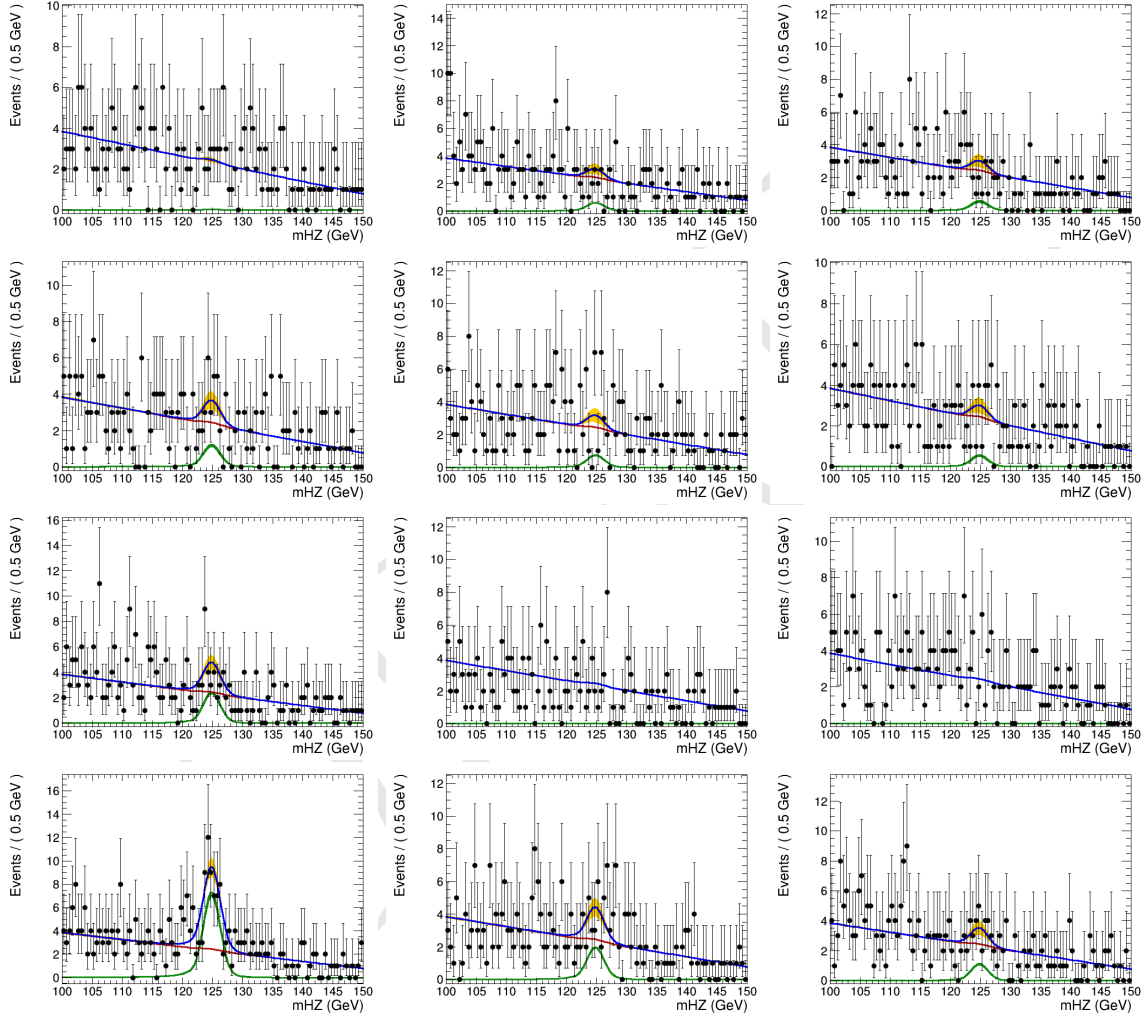


Figure 4.68: Examples of the toy datasets fit ($M_{\mu\mu\gamma}$), for the Higgs decay analysis, after the toy dataset refit, for 1S, 2S and 3S (left to right), with μ_{true} equals to 100000, 200000, 300000, 1000000 (top to bottom). The red lines corresponds to the background model (B), the green lines to signal model (S), the blue lines to the total (S+B) and the dots is the toy dataset.

1136 It is expected that the pulls distribution for the fitted signal strength ($\frac{\mu_{fit} - \mu_{true}}{\sigma_{fit}}$) should follow a
 1137 Gaussian distribution centered in 0 and with σ around 1. Figures 4.69 and 4.70 present those pulls
 1138 distributions for the Z and Higgs decays, respectively.

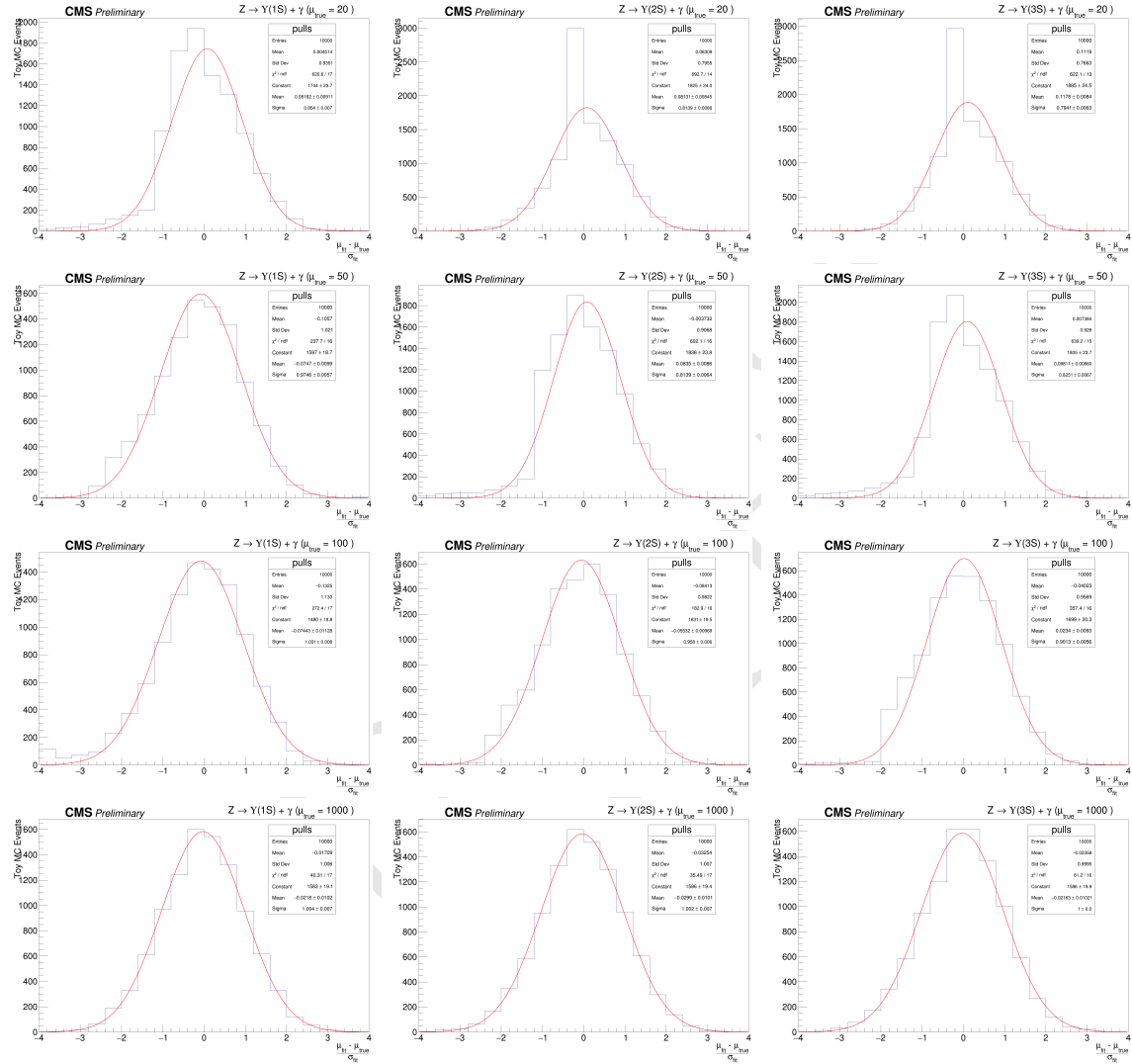


Figure 4.69: Distribution of pulls ($\frac{\mu_{fit} - \mu_{true}}{\sigma_{fit}}$), for the Z decay analysis, after the toy dataset refit, for 1S, 2S and 3S (left to right), with μ_{true} equals to 20, 50, 100, 1000 (top to bottom).

1139 As a general conclusion on this cross check, as long as the toy MC generation is able to inject enough
 1140 signal to be fit, the final modeling of this analysis is able to recover a Gaussian pulls distribution.
 1141 This, of course, depends on the Υ state to be considered. For the Z decay, between $\mu_{true} = 50$
 1142 and $\mu_{true} = 100$ (around a hundred of events passing full selection), while for the Higgs decay, it
 1143 is needed only a few events after full selection, even though it means hundreds of thousands times
 1144 the expected signal, since the very small cross sections for the decay, as shown in Table 4.1.

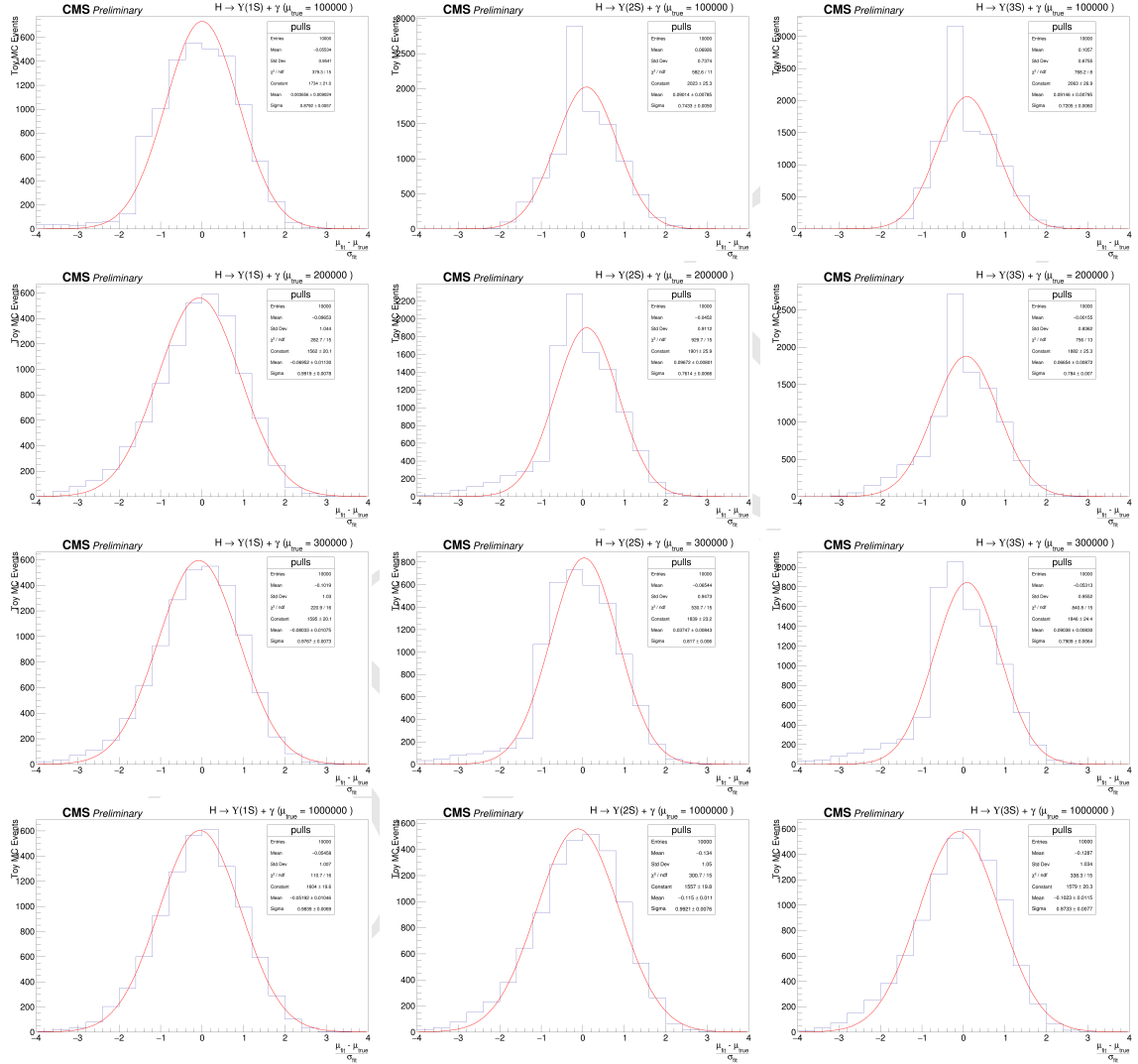


Figure 4.70: Distribution of pulls ($\frac{\mu_{fit} - \mu_{true}}{\sigma_{fit}}$), for the Higgs decay analysis, after the toy dataset refit, for 1S, 2S and 3S (left to right), with μ_{true} equals to 100000, 200000, 300000, 1000000 (top to bottom).

1145 5 Results and conclusion

1146 A two-dimensional (2D) unbinned maximum-likelihood fit to the $m_{\mu^+\mu^-\gamma}$ and $m_{\mu^+\mu^-}$ distributions
1147 was used to compare the data with background and signal predictions. Search has been performed for
1148 a SM Higgs and Z boson decaying into a $\Upsilon(1S, 2S, 3S)\gamma$, with $\Upsilon(1S, 2S, 3S)$ subsequently decaying
1149 into $\mu^+\mu^-$ using data obtained from 35.9 fb^{-1} of pp collisions at $\sqrt{s} = 13 \text{ TeV}$.
1150 Since no excess has been observed above the background, the CL_s formalism is applied, in order to
1151 establish an upper limit in the branching fractions for each channel.

1152 5.1 The CL_s formalism for upper limits setting at CMS

1153 The CL_s formalism [77] consist in a modified frequentist approach to obtain an upper limit for a
1154 certain parameter of a model, with respect to the data, when there is no significant excess that could
1155 justify an observation. It is based on the profile-likelihood-ratio test statistic [78] and asymptotic
1156 approximations [79]. It is a standard upper limit setting procedure for the LHC experiments [80].
1157 When searching for non-observed phenomena, it is often usual to derive the results as a function of
1158 the signal strength modifier μ , which is a free parameter of the full model (signal + background).
1159 It can be define such as, the expectation value for the number of events in a bin ¹ is:

$$E[n] = \mu s + b, \quad (5.1)$$

1160 where, s and b are the expected number of signal e background events, respectively.

1161 The Neyman–Pearson lemma [78] states the likelihood ratio is the optimal test between a null
1162 hypothesis and an alternative one (i.e. background-only and signal-plus-background models). On
1163 top on this, one could build a likelihood ratio test as:

$$q(\mu) = -2 \ln \left(\frac{\mathcal{L}(\text{data}|\mu s + b)}{\mathcal{L}(\text{data}|b)} \right), \quad (5.2)$$

1164 where the denominator and numerator defines the likelihoods for the background-only and signal-
1165 plus-background models, respectively. The was the hypothesis test used by LEP and Tevatron
1166 experiments (the former one, with some modifications to include the nuisances effects).

1167 With these two models, i.e. their *pdfs*, one can throw toy MC events in order to construct a
1168 distribution of $q(\mu)$, namely $f(q(\mu)|\mu)$. The *p*-value of $f(q(\mu)|\mu)$, as below, can be used to chose
1169 between each model.

$$p_\mu = \int_{q(\mu)_{\text{data}}}^{\infty} f(q(\mu)|\mu) dq(\mu), \quad (5.3)$$

1170 where $q(\mu)_{\text{data}}$ is the observed value of $q(\mu)$ on data, for a given μ .

¹A set of common analysis criteria.

If p_μ is less than α (usually 0.05 or 0.1) the background-only model can be excluded in favor of the signal-plus-background model. For the propose of a confidence interval estimation, the argument can be reversed and one could look for all the values of μ that would not be excluded with Confidence Level (CL) $1 - \alpha$.

The problem with this definition is that, when the expected signal strength is very small, e.g. a invariant mass distribution in the TeV scale, the null hypothesis and the alternative one are almost indistinguishable. In this situation, a downward fluctuation of the background might lead us to exclude the alternative hypothesis (signal) in a region of low experimental sensitivity region. Putting in number, if we expect 50 background events and 2 signal events, but we observe 40 events, the signal would be easily excluded.

In order to take this effect into account, a modified frequentist approach for upper limits setting, the CL_s was proposed during the Higgs search era at LEP. Lets start by considering a profile likelihood ratio [81] as below:

$$\lambda(\mu) = \frac{\mathcal{L}(\text{data}|\mu, \hat{\theta})}{\mathcal{L}(\text{data}|\hat{\mu}, \hat{\theta})}, \quad (5.4)$$

where, $\mathcal{L}(\text{data}|\mu, \hat{\theta})$ is the profile likelihood function.

Defining μ and the investigated signal strength, $\hat{\theta}$ is the nuisances that maximizes the likelihood for a given μ (fixed) while $\hat{\mu}$ and $\hat{\theta}$ are the signal strength and nuisances that, overall, maximizes the likelihood. The advantage of the

CMS and ATLAS have a common set of statistical guidelines [82] to ensure the compatibility of the published results. Following these recommendations, the statistics test based on 5.4 is:

$$\tilde{q}_\mu = -2\ln[\lambda(\mu)], \text{ with } 0 \leq \hat{\mu} \leq \mu. \quad (5.5)$$

The left side restriction ($0 \leq \hat{\mu}$) ensure us the proper physical interpretation of μ as a positive define signal strength, i.e., the observation a process would, for a given bin, increase the number of events. The right side restriction $\hat{\mu} \leq \mu$ secure the interpretation of \tilde{q}_μ 's p -value as a one-sided confidence interval. This is required for a upper limit definition.

The advantage of using the profile likelihood ratio is that, even though it takes into account the effect of nuisances in the likelihood, it is possible to prove that, with the use of Wilk's Theorem [65], that a statistic test defined as \tilde{q}_μ , asymptotically follows a chi-square distribution with one degree of freedom (the signal strength) [79]. Thus, \tilde{q}_μ is said to be approximately independent of any nuisance and allow a fast computation of its p -value without the need of toy MC strategies (which can computationally demanding, depending on the complexity of the models), event though this is not the standard CMS/ATLAS recommendation.

Based on \tilde{q}_μ , defined at 5.5, one should compute the $\tilde{q}_\mu^{\text{obs}}$, also the $\hat{\theta}_\mu^{\text{obs}}$ and $\hat{\theta}_{\mu=0}^{\text{obs}}$, which corresponds to the observed value of \tilde{q}_μ on data, the maximum likelihood estimator for the nuisances assuming some signal strength μ and assuming a background-only model, respectively. Then, the distributions of $f(\tilde{q}_\mu|\mu, \hat{\theta}_\mu^{\text{obs}})$ and $f(\tilde{q}_\mu|\mu = 0, \hat{\theta}_{\mu=0}^{\text{obs}})$ are generated tossing pseudo-random toy MC. Figure 5.1 presents an example of these two distributions.

The CL_s value is defined as:

$$CL_s(\mu) = \frac{p_{s+b}(\mu)}{1 - p_b}, \quad (5.6)$$

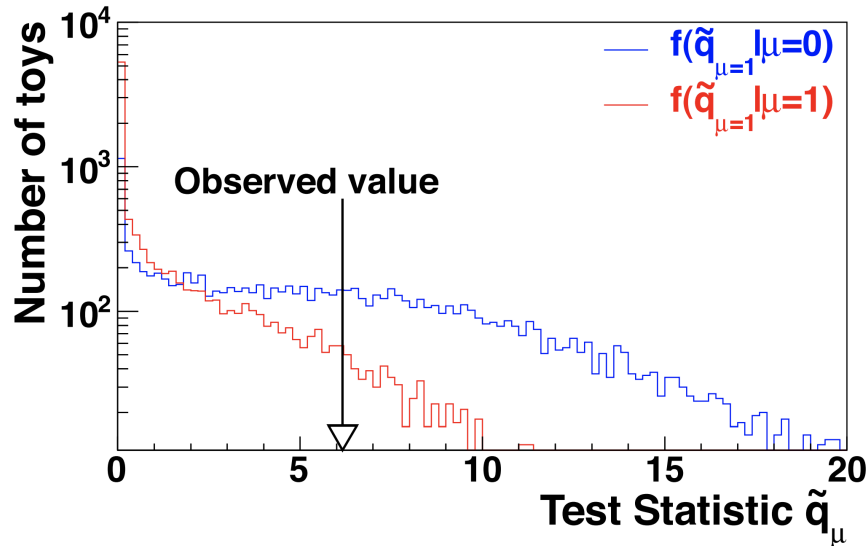


Figure 5.1: Example of $f(\tilde{q}_\mu | \mu, \hat{\theta}_\mu^{\text{obs}})$ $f(\tilde{q}_\mu | \mu = 0, \hat{\theta}_{\mu=0}^{\text{obs}})$ distributions generated with toy MC.
Source: [82].

1207 where:

$$p_{s+b}(\mu) = \int_{\tilde{q}_\mu^{\text{obs}}}^{\infty} f(\tilde{q}_\mu | \mu, \hat{\theta}_\mu^{\text{obs}}) d\tilde{q}_\mu \quad (5.7)$$

and

$$p_b = \int_{-\infty}^{\tilde{q}_\mu^{\text{obs}}} f(\tilde{q}_\mu | \mu = 0, \hat{\theta}_{\mu=0}^{\text{obs}}) d\tilde{q}_\mu \quad (5.8)$$

1208 Scanning different values of μ , within $0 \leq \hat{\mu} \leq \mu$, one would exclude the ones which $CL_s < \alpha$. CMS
1209 and ATLAS recommends a CL level $(1 - \alpha)$ of 95%.

1210 The main advantage of the CL_s approach is that the presence of the denominator $1 - p_b$ in 5.6
1211 penalizes the exclusion of regions in which the experiment is no sensitive. Figure 5.2 helps to
1212 illustrate this. One can notice that a small value of p_{s+b} (yellow area) is balanced by large value
1213 of p_b (green area). When the experimental sensitivity is higher, the two distributions tend to be
1214 far away from each other. Thus leading to a smaller compensation factor (p_b) and enhancing the
1215 chance of a exclusive CL_s value.

1216 The expected expected upper limit and its $\pm 1\sigma$ and $\pm 2\sigma$ are determined by generating a large
1217 number of toy mc events, for the background-only model ($\mu = 0$), with nuisances free to float,
1218 and for each simulation finding $\mu_{95\%}$, which defines the confidence level. Once enough samples are
1219 generated, one should scan, from left to right, the cumulative distribution of $\mu_{95\%}$. The median
1220 defines the expected value and the quantiles for 16%, 84% and 2.5%, 97.5% defines the $\pm 1\sigma$ and
1221 $\pm 2\sigma$, respectively.

1222 5.2 Branching fraction upper limits

1223 The result are summarized on table 5.1.

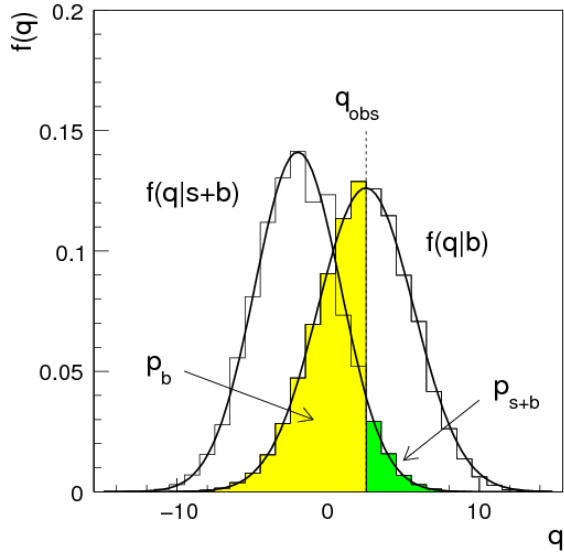


Figure 5.2: Example of $f(\tilde{q}_\mu|\mu, \hat{\theta}_\mu^{\text{obs}})$ $f(\tilde{q}_\mu|\mu = 0, \hat{\theta}_{\mu=0}^{\text{obs}})$ distributions generated with toy MC. In the figure, q must be read as \tilde{q} . The green area shows the p_{s+b} defined in 5.7, while the yellow one shows p_b defined in 5.8. Source: [79].

1224 The observed(expected) exclusion limit at 95% confidence level on the $\mathcal{B}(Z \rightarrow \Upsilon(1S, 2S, 3S)\gamma) =$
 1225 $2.9, 2.7, 1.4 (1.6^{+0.8}_{-0.5}, 2.0^{+1.0}_{-0.6}, 1.8^{+1.0}_{-0.6}) \times 10^{-6}$, and on the $\mathcal{B}(H \rightarrow \Upsilon(1S, 2S, 3S)\gamma) = 6.9, 7.4, 5.8$
 1226 $(7.3^{+4.0}_{-2.4}, 8.1^{+4.6}_{-2.8}, 6.8^{+3.9}_{-2.3}) \times 10^{-4}$.

1227 As stated before, this analysis was done, for the Z decay, taking into account a mutually exclusive
 1228 categorization of events, based on the reconstructed photon properties (η_{SC} and R9 value), as
 1229 described in section 4.7.

1230 At table 5.2 we present the results obtained when there is no categorization of events (Inclusive
 1231 category).

1232 It is worth to remember that the categorization takes places only for the Z decay. For the Higgs
 1233 decay, no categorization is imposed.

1234 By taking, or not, into account any categorization, the numbers presented in both tables (5.1 and
 1235 5.2), are compatible within themselves and with the results published by the ATLAS collabora-
 1236 tion [83].

Table 5.1: Summary table for the limits on branching ratio of $Z \rightarrow \Upsilon(1S, 2S, 3S)\gamma$ and $H \rightarrow \Upsilon(1S, 2S, 3S)\gamma$ decays.

| 95% C.L. Upper Limit | | | |
|------------------------------------|--|---------------------|---------------------|
| | $\mathcal{B}(Z \rightarrow \Upsilon\gamma) [\times 10^{-6}]$ | | |
| | $\Upsilon(1S)$ | $\Upsilon(2S)$ | $\Upsilon(3S)$ |
| Expected | $1.6^{+0.8}_{-0.5}$ | $2.0^{+1.0}_{-0.6}$ | $1.8^{+1.0}_{-0.6}$ |
| Observed | 2.9 | 2.7 | 1.4 |
| SM Prediction [$\times 10^{-8}$] | 4.8 | 2.4 | 1.9 |
| | | | |
| | $\mathcal{B}(H \rightarrow \Upsilon\gamma) [\times 10^{-4}]$ | | |
| | $\Upsilon(1S)$ | $\Upsilon(2S)$ | $\Upsilon(3S)$ |
| Expected | $7.3^{+4.0}_{-2.4}$ | $8.1^{+4.6}_{-2.8}$ | $6.8^{+3.9}_{-2.3}$ |
| Observed | 6.9 | 7.4 | 5.8 |
| SM Prediction [$\times 10^{-9}$] | 5.2 | 1.4 | 0.9 |

Table 5.2: Summary table for the limits on branching ratio of $Z \rightarrow \Upsilon(1S, 2S, 3S)\gamma$, for the two possible categorization scenarios.

| 95% C.L. Upper Limit - $\mathcal{B}(Z \rightarrow \Upsilon\gamma) [\times 10^{-6}]$ | | | |
|---|------------------------|---------------------|---------------------|
| | without categorization | | |
| | $\Upsilon(1S)$ | $\Upsilon(2S)$ | $\Upsilon(3S)$ |
| Expected | $1.7^{+0.9}_{-0.5}$ | $2.1^{+1.1}_{-0.7}$ | $1.9^{+1.0}_{-0.6}$ |
| Observed | 2.6 | 2.3 | 1.2 |
| | | | |
| | with categorization | | |
| | $\Upsilon(1S)$ | $\Upsilon(2S)$ | $\Upsilon(3S)$ |
| Expected | $1.6^{+0.8}_{-0.5}$ | $2.0^{+1.0}_{-0.6}$ | $1.8^{+1.0}_{-0.6}$ |
| Observed | 2.9 | 2.7 | 1.4 |

DRAFT

1237 6 CMS Resistive Plate Chambers - RPC

- 1238 In the course of this PhD study, there were a lot of opportunities to work for the RPC project, in
1239 the context of the CMS Collaboration. The main activities consists of shifts for the RPC operation
1240 and data certification, upgrade and maintenance of the online software, R&D activities for the RPC
1241 upgrade and detector maintenance during the LHC Long Shutdown 2 (2019 to 2020).
- 1242 In this chapter, it is presented a summary of the Resistive Plate Chamber technology and the
1243 contributions to the RPC project at CMS.

1244 6.1 Resistive Plate Chambers

- 1245 The seminal paper on the Resistive Plate Chamber (RPC) technology was presented by R. Santonico
1246 and R. Cardarelli, in which they described a "dc operated particle detector (...) whose constituent
1247 elements are two parallel electrode Bakelite plates between" [84]. The key idea behind the RPC,
1248 with respect to other similar gaseous detectors, is the use of two resistive plates as anode and
1249 cathode, which makes possible to have a small localized region of dead time, achieving very good
1250 time resolution.
- 1251 The working principle for RPCs relies on the idea that an ionizing particle crossing the detector, tends
1252 to interact with the gap between the two plates (filled with some specific gas mixture) and form a
1253 ionizing cascade process, in which the produced charged particles are driven by the strong uniform
1254 electrical field produced by the two plates.
- 1255 The gas mixture is a key component of a RPC. Even though the first RPCs were produced with
1256 a mixture of argon and butane, nowadays RPCs use a mixture of gases that would enhance an
1257 ionization caused by the incident particle and quench secondary (background) effects.
- 1258 Another feature of the RPCs is its construction simplicity and low cost. This allows the use of RPC to
1259 cover larger areas at a reasonable cost.
- 1260 An extensive review of the RPC technology and its applications can be found at [85].

1261 6.1.1 Principles and operation modes

- 1262 The core of a RPC chamber is a gap made with two parallel high resistivity plates, separated
1263 by some regular distance (typically millimeters), filled with a proper gas mixture and under
1264 appropriate high voltage (HV) applied on the plates (electrodes, from here on). When an ionizing
1265 particle crosses the gap, there is a high enough chance the the particle will interact with the gas
1266 and produce a newly created positive ion and an electron. This pair will travel in opposite directions,
1267 according to the electric field from the electrodes. During this process, the electron will gain kinetic
1268 energy and inelastically interact with other neighboring atoms/molecules, creating excitations in their
1269 energy levels and, potentially, also ionizing them. The secondary ionization electrons will also follow
1270 the same course, creating an **Avalanche** of positive and negative particles/ions traveling towards the

electrodes. This process is proportional to the applied electric field. Figure 6.1 illustrates the avalanche production.

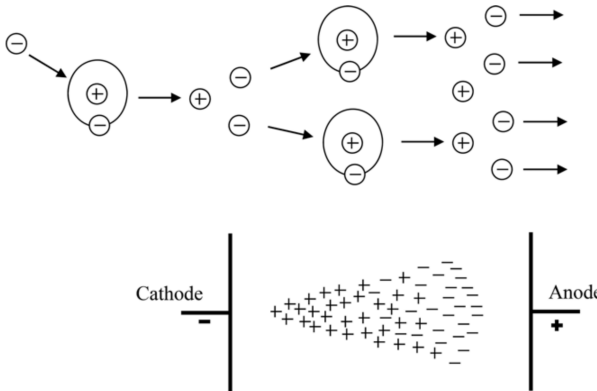


Figure 6.1: The Avalanche production process inside a RPC gap. (Top) The initial process and the secondary electron/ion generation. (Bottom) The overall charge distribution of an Avalanche between the electrodes. Source: [86].

The number of particle composing the avalanche can be expressed as (assuming constant pressure) [86]:

$$n_e = n_0 e^{\alpha d} = n_0 A, \quad (6.1)$$

where n_0 is the number of initial electrons initiating the avalanche, A is the *gas gain*, or *multiplication factor* and d is the distance since the avalanche creation. This is also known as Townsend theory for discharges and α is the first Townsend coefficient.

When the positive ions bunch reaches the cathode, under certain conditions (if the first ionization energy of the ion is greater than the work function of the cathode), the recombination of the ion with the electrode material might release electrons which will also follow the electric field. The relative probability (with respect to the primary electron emission) of this emission to happen (γ_+) is called the the second Townsend coefficient.

$$n_+ = n_0 A \gamma_+. \quad (6.2)$$

Another process which can occur is the secondary photoelectron productions, described by a similar equation as above: $n_{pe} = n_0 A \gamma_{ph}$. This production is mostly related to de-excitation of molecules and atoms in vicinity of the avalanche. The produced photons might initiate new ionization process.

As an alternative to the Townsend theory, Raether, Meek, and Loeb, proposed the *streamer-leader theory* [87]. This theory is valid when there is a high enough concentration of ions produced. This critical value is called Raether limit.

$$n_0 A > 10^8 \text{ electrons} \quad (6.3)$$

In this limit, the electric field created by the space distribution is high enough to be same order of the external field. In the vicinity of the head (or tail) of the avalanche the field gets disturbed and intensified. The intensification of the field enhances the ionization effect and give rise to secondary avalanches (photoelectrons). The intensified field also makes the photoelectrons produced travel towards the head (positive ions). Their antikuaption generates more UV radiation and more

secondary avalanches. This whole process is called **Streamer**. If no quenching is imposed, the streamer might evolve to a spark, fully discharging on the electrodes. If the concentration of electrons is high enough, the avalanche tail (electrons) might also give rise to a streamer (namely, negative streamer). Figure 6.2 illustrates the different subprocess related to streamer production.

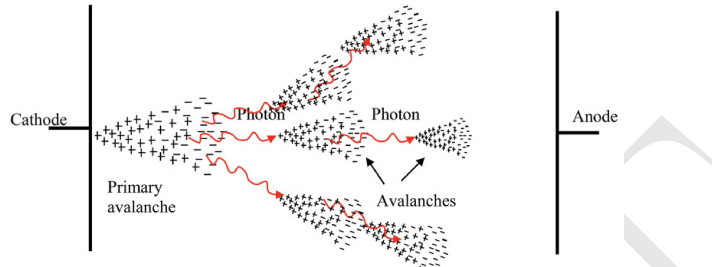


Figure 6.2: Streamer formation process. The distorted electric field around the high positive charge concentration enhances the ionization process, initiating secondary avalanches. Source: [86].

A RPC where most of the charge multiplication process happens in the form of a streamer is said to be working in **Streamer Mode**. The advantage of the streamer mode is the high induced charge which is easily caught by non-sensitive readout electronics. On the other hand, the streamer mode, because of its highly associated charge, will have an impact in the rate capability of the detector (the local dead time will be higher).

Because of the high background environment of LHC, the CMS RPC operates in **Avalanche Mode**, where discharge is highly quenched and very well localized. On the other hand, a very sensitive readout electronics is required to cope with the high rate demanded.

A good review of electrical discharge on gases can be found at [86].

6.2 CMS Resistive Plate Chambers

At CMS, the Resistive Plate Chamber are installed in both the barrel and endcap region, forming a redundant system with the DT (barrel) and CSC (endcap). As described in the CMS Muon Technical Design Report (Muon-TDR) [88], the RPC are composed of 423 Endcap chambers and 633 barrel chambers. Figure 6.3 presents a picture of the CMS RPCs installed on station RE+4 of the Endcap.

Each chamber consists of two gas gaps (double gap), 2 mm tick each, made of Bakelite (phenolic resin) with bulk resistivity of $10^{10} - 10^{11} \Omega m$. The choice of the bulk resistivity of the electrode has high impact on the rate capability of the detector.

Each gap has its external surface is coated with a thin layer of graphite paint, which acts as conductive material, distributing the applied high-voltage (HV). On top of the graphite a PET film is used for isolation. A sheet of copper strips is sandwiched between the gaps. Everything is wrapped in aluminum case.

The double gap configuration increases the efficiency of the chamber, since the signal is picked up from the OR combination of the two gaps. A chamber with only one gap working, loses around 15% of efficiency, even though, this can be recovered by increasing the HV applied during operation mode (working point - WP).

A characteristic that differentiate the CMS RPC from previous RPC application in HEP is the operation mode. A RPC at CMS, operates in avalanche mode, while previous experiments used

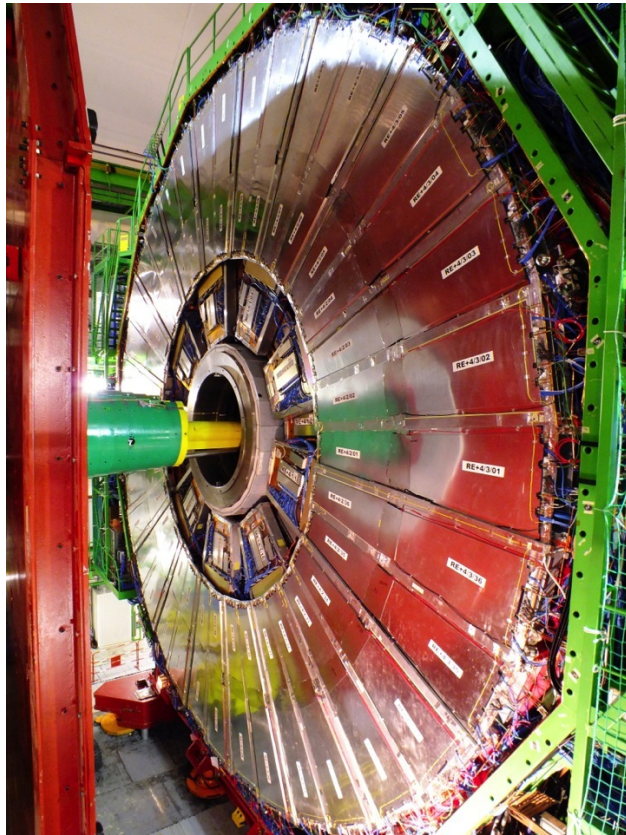


Figure 6.3: RPC chamber on installed on station RE+4 of CMS Endcap. Source: [89].

1326 the streamer mode. Both modes are related to the applied HV, in commitment with the strength of
 1327 the generated signal, and are capable of generate a well localized signal, which can be picked up by
 1328 the readout electronics, but the avalanche mode offer a higher rate capability around 1 kHz/cm^2 ,
 1329 while the streamer mode goes up to 100 Hz/cm^2 . The high rate capability is a key factor in order
 1330 to cope with requirements of the LHC luminosity, specially in the high background regions.

1331 Besides the rate capability, the key factors that driven the CMS RPC design were: high efficiency ($>$
 1332 95%), low cluster size (> 2) for better spatial resolution (this reflects in the momentum resolution)
 1333 and good timing in order to do the readout of the signal within the 25 ns of a LHC bunch cross
 1334 (BX) and provide it to the CMS trigger system. These requirements have implications in the choice
 1335 of material, dimensions, electronics and gas mixture.

1336 In the barrel, along the radial direction, there are 4 muon layers (called stations), MB1 to MB4.
 1337 MB1 and MB2 is composed of a DT chamber sandwiched between two RPC chambers (RB1 and
 1338 RB2) with rectangular shape. The stations MB3 and MB4 have only one RPC (RB3 and RB4) are
 1339 composed by two RPC chambers (named - and + chambers with the increase of ϕ) attached to one
 1340 DT chamber, except in sector 9 and 11, where there is only one RPC. RE4, sector 10 is a special
 1341 case, since it is composed of four chambers (-, -, + and ++). These stations are replicated along
 1342 the z direction in five different wheels of the CMS (W-2, W-1, W0, W+1 and W+2) and in twelve
 1343 azimuthally distributed sectors (S1 to S12). Figure 6.4 show the different barrel stations and wheel.

1344 In the endcap, the RPC chambers have a trapezoidal shape and are distributed in four disks (or
 1345 stations) each side (RE \pm 4, RE \pm 3, RE \pm 2, RE \pm 1), each one with 72 chambers. CMS split up its
 1346 disks in 3 rings, along the radial direction, and 36 sector in the azimuthal angle. RPCs are present
 1347 in the two outer rings (R2 and R3), in all 36 sectors. The RE \pm 4 are special cases, since these
 1348 chambers were installed only in 2014, a design choice was made the mechanically attached R2 and

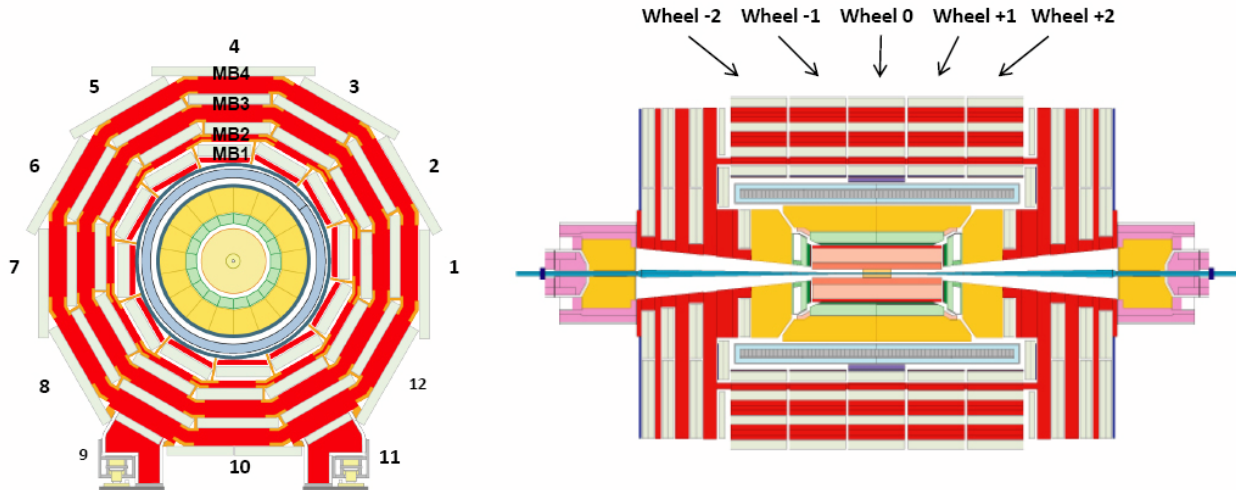


Figure 6.4: R- ϕ (left) and R-Z (right) projections of the barrel Muon System.

1349 R3 chambers, each sector, in what is called, a super-module. Figure 6.5 show the different endcap
 1350 disks.

1351 The length of the strips is chosen, for both barrel and endcap, in such a way to control the area of
 1352 each strip, in order to reduce the fake muons, due to random coincidence. This has to do with the
 1353 time-of-flight and signal propagation along the strip. In the barrel, each chamber readout is divided
 1354 in two regions (rolls), called forward and backward (along increasing $|\eta|$)¹. In the endcap, the strips
 1355 are divided in 3 regions, called partitions A, B and C (from inside the detector to outside).

1356 The gas mixture used in the CMS RPCs is composed by C2H2F4 (Freon R-134a, tetrafluoroethane),
 1357 C4H10 (isobutane), SF6 (sulphur hexafluoride) (95.2 : 4.5 : 0.3 ratio) and with controlled humidity
 1358 of 40% at 20-22 °C. The Freon is used to enhance the ionization and charge multiplication that
 1359 characterizes the avalanche, while the isobutane is introduced for quenching proposes, in order to
 1360 reduce the secondary ionizations that could lead to formation of streamers and the SF6 is used
 1361 to reduce the electron background. The choice of Freon over other gases, i.e. argon-based and
 1362 helium-based, was motivated by previous studies [90, 91].

1363 Since its R&D, the RPC have shown good performance over aging. This is even historical over
 1364 previous RPC experiments [92–98]. Even the most recent studies of aging, taking into account
 1365 future LHC conditions (High-Luminosity LHC - HL-LHC) plus a safety margin of 3 times the
 1366 expected background (600 Hz/cm^2) have shown good aging hardness [99].

1367 6.2.1 Performance

1368 The RPCs, for the CMS experiment, contribute mainly with triggering inputs, due to its very good
 1369 time resolution. The important parameters which are monitored to evaluate the RPC performance
 1370 are the efficiency and cluster size. The former is related to the ratio of the registered hits over the
 1371 number of muons that passed through the chamber, while the former one is the number adjacent
 1372 strip (minimal readout unit) that were fired (activated) per hit. Figures 6.6 and 6.7 present the
 1373 historical distribution of efficiency and cluster size as a function of the integrated luminosity collect
 1374 during Run2.

¹Some chamber are divided in three rolls, forward, middle and backward, for trigger propose.

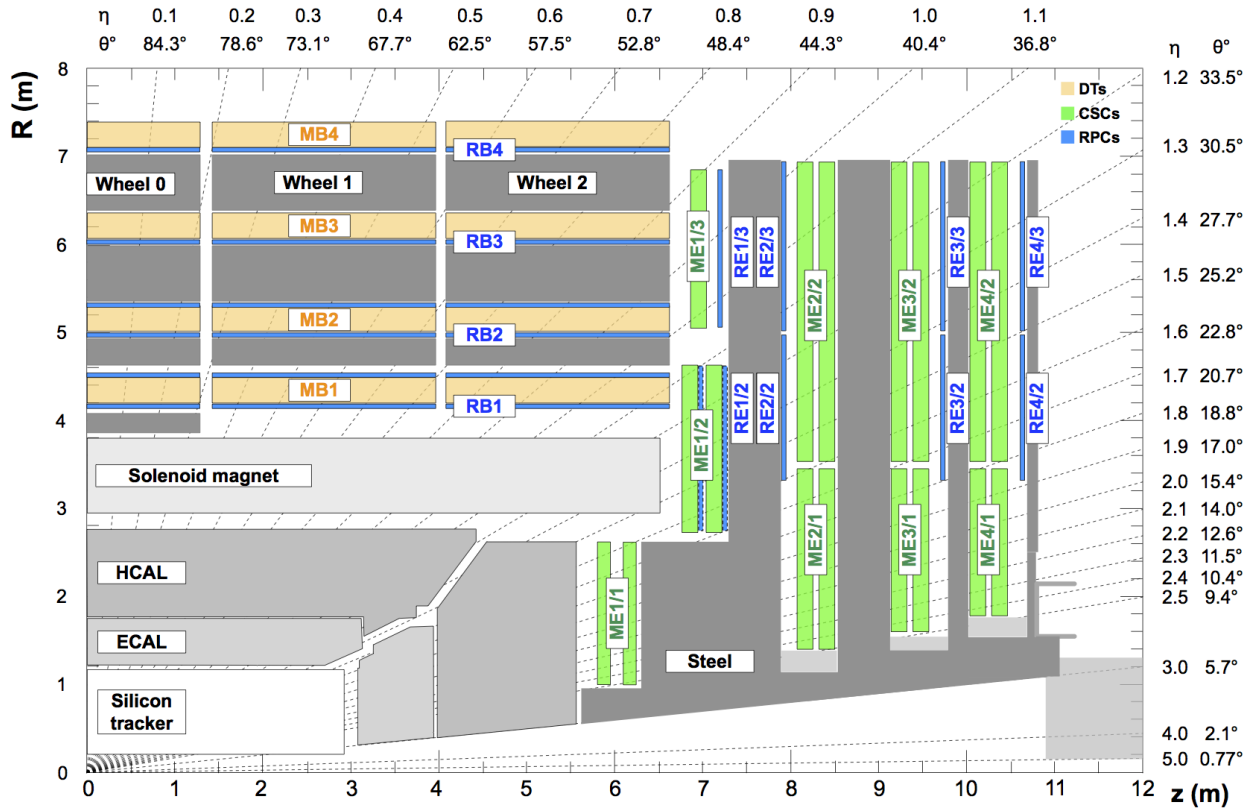


Figure 6.5: R-Z projections of the endcap Muon System (positive Z side). This is the same configuration for the 36 ϕ sectors.

1375 In general, the RPC system operates with efficiency above 95% and cluster size smaller than 3
 1376 (a good parameter established during the design phase). The importance of the efficiency is a
 1377 less complicated concept to catch, on the other hand, the cluster size might not be so straight
 1378 forward. The optimal regime of RPCs operation at CMS is the avalanche mode, in which the
 1379 electrical discharge is constrained in a millimeter level size region. Another operation mode is the
 1380 streamer mode, in which the initial discharge might trigger secondary ones, e.g. by the emission of
 1381 unquenched photons. A streamer discharge is capable of fire neighbor strips, increasing the cluster
 1382 size. Operating in avalanche mode is fundamental to keep the RPCs capable of dealing with the
 1383 high background environment of CMS.

1384 To keep the mean cluster size under control (< 3) is important to guarantees enough spatial reso-
 1385 lution for the measurements (the geometrical position of a hit is the midpoint of the cluster) and
 1386 ensures that the system has enough rate capability to operate, since a RPC with a high sensitive
 1387 front-end electronics (necessary for the avalanche mode operation) could be degraded by pileup of
 1388 dead time on many channels, including electronics noise, streamers, darks counts and other sources
 1389 of background.

1390 A third important parameter to be measured and controlled in a RPC system, under the LHC
 1391 conditions, is the current due to the high voltage applied. This current is known to be proportional
 1392 to the total charge released in each electrical discharges and to the hit rate on the chamber. The
 1393 voltage applied is divided, as in a series circuit, between the electrodes and the gap. At increasing
 1394 background, the current also increases and, since the applied voltage is constant, the voltage across
 1395 the gap is reduced in favor of the voltage across the electrodes. This reduction of effective voltage
 1396 on the gas, might have an impact on its gain, imposing a reduction on the detector sensitivity.

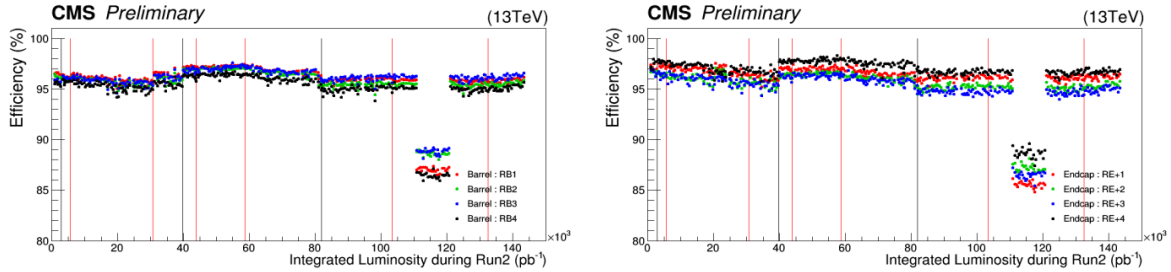


Figure 6.6: RPC efficiencies (per chamber) over Run2 Integrated Luminosity for Barrel (left) and Endcap (right). Red lines indicates technical stops (TS) while grey ones indicates Year-End-Technical stops (YETS). The drop in the efficiency around 110 pb^{-1} is related to a known operation mistake. Source: [100].

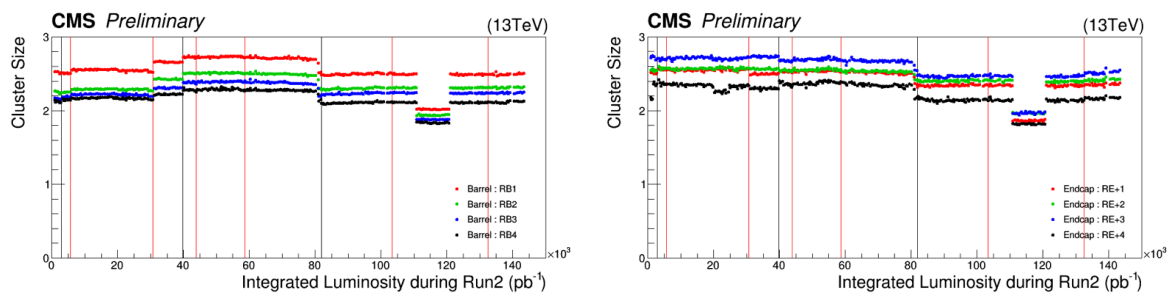


Figure 6.7: RPC cluster size (CLS - per chamber) over Run2 Integrated Luminosity for Barrel (left) and Endcap (right). Red lines indicates technical stops (TS) while grey ones indicates Year-End-Technical stops (YETS). The drop in the cluster size around 110 pb^{-1} is related to a known operation mistake. Source: [100].

Figure 6.8 presents the ohmic currents ² in different regions of the detector, from 16th of April, 2018 to 2nd of December, 2018. It is clear how the stations subjected to higher background ($RE \pm 4 - 40 \text{ Hz/cm}^2$) are subjected to a degrading factor that increases with the luminosity (background rate) and decreases when the detector is powered off. This effect is supposed to be related with the Hydrogen Fluoride (HF) production inside the gap, due to the electrical discharges. HF is a conductivity molecule, which can potentially attach to the internal surface of the gap, reducing the overall resistivity. The HF production can be controlled by properly tuning the gas flow as a function of the background that the chamber is subjected. HF concentration can also lead to permanent degradation of the gap, due to its chemical properties. Keeping the currents levels as low as possible is important for aging proposes.

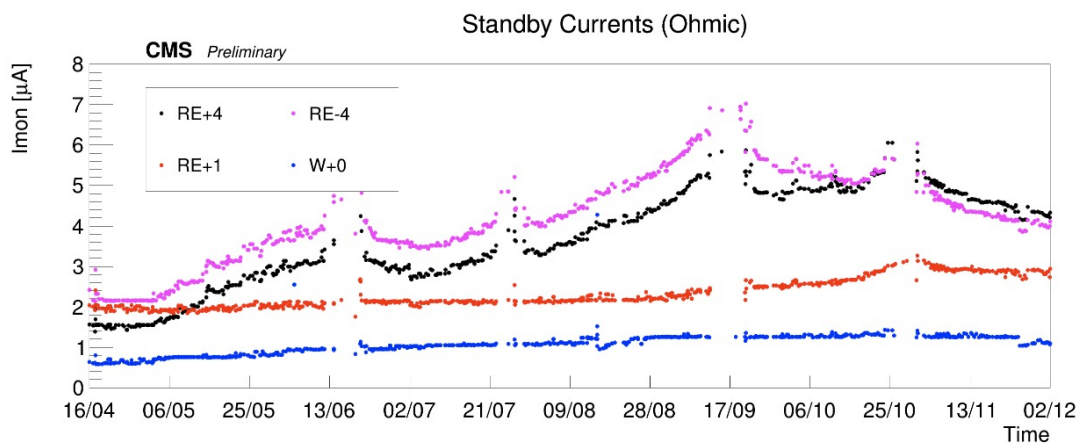


Figure 6.8: Ohmic current history of W+0, RE+1, RE+4 and RE-4. The blank regions, from time to time, corresponds to technical stops (TS), when the detector is off. Source: [100].

A review of the RPC performance during Run2 can be found at [100].

6.3 Contribution to the CMS RPC project

During the course of this study, a head collaboration of our research group and the CMS RPC project was established. Many contributions were given to the project as part of the graduation as a experimental particle physicist, with focus on getting acquaintance with a subsystem technology and give a meaningful collaboration to the detector operation. Those are considered by the community important steps on the student graduation.

Bellow it is described the contributions given to the CMS RPC project.

6.3.1 RPC Operation - Shifts and Data Certification

The first activities done for the CMS RPC project were shifts for data certification of data taken. This certification is done by specialized people for different CMS subsystems and physics objects groups ³.

²Current at 6500 V, which is below the typical working point of a CMS RPC (around 9500 V). In this region, no charge multiplication effect take place and chamber current is governed only by Ohm's Law.

³Groups of reconstruction and performance experts for different high-level reconstructed objects from CMS, i.e. muons, taus, jets/MET, electrons/photons

- 1419 This certification is done in order to ensure the quality of the date recorded based on the well
 1420 functionality of each system during the data taking and the reconstruction of the physics objects in
 1421 the expected matter. A certain collection of data (run) is said certificate when all subsystems and
 1422 object experts agrees on this.
- 1423 Figure 6.9 shows, as an example of the luminosity delivered by the LHC, recorded one by CMS and
 1424 the certified (validated), from the 22nd of April, 2016 to the 27th of October, 2016. Only certified
 1425 data is available for physics analysis.
- 1426 Shifts are a continuous weekly activity (specially during the data taking period), performed in a
 1427 weekly basis, in order to ensure the availability of certified data, as soon as possible.

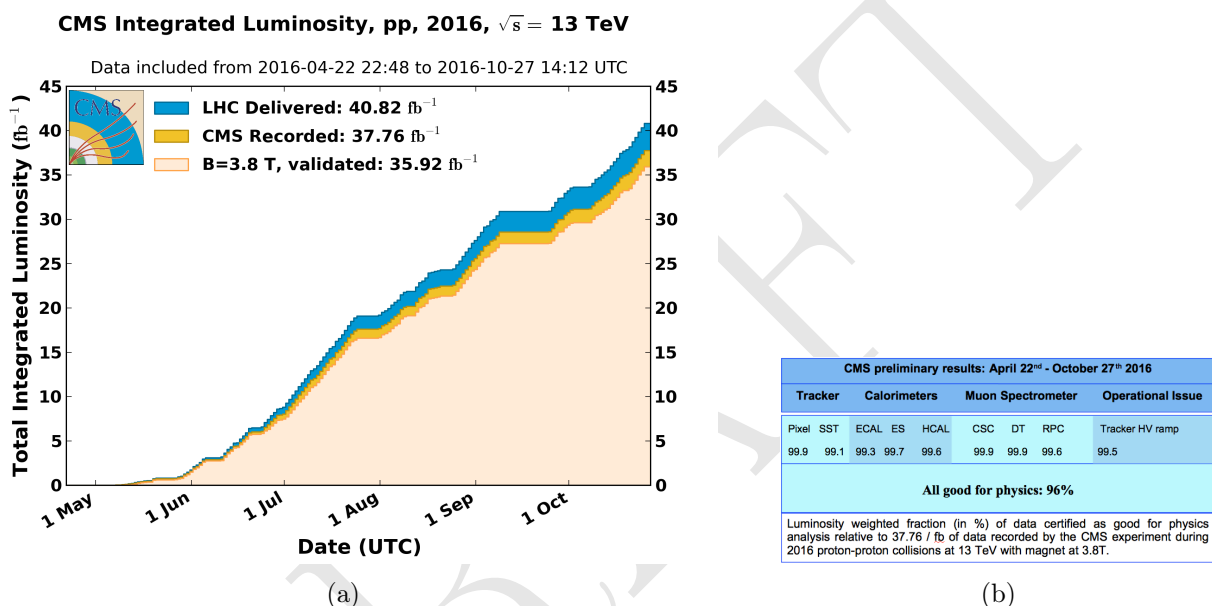


Figure 6.9: (a) Luminosity delivered by the LHC, recorded one by CMS and the certified (validated), from the 22nd of April, 2016 to the 27th of October, 2016. (b) Efficiency of the certification process for each subsystem, from the 22nd of April, 2016 to the 27th of October, 2016. Total CMS efficiency is above 90%. Source: [101]

1428 6.4 RPC Online Software

- 1429 On what concerns the Online Software (OS) of the CMS RPC system, the main contribution given
 1430 was the upgrade of the Trigger Supervisor libraries.
- 1431 The Trigger Supervisor is a web-based software, which run over the xDAQ backend and provides,
 1432 through a modules organized in a tree system, called cells, a standard interface for the operation and
 1433 monitoring of different system at CMS. In principle only systems which contribute directly to the
 1434 L1 trigger should have a Trigger Supervisor implementation. This was the case for the RPC during
 1435 the Run1. Since Run2, RPC contributes to the trigger indirectly, by providing data to the muon
 1436 processors (CPPF, OMTF and TwinMux). The Trigger Supervisor implementation is a legacy from
 1437 that period.
- 1438 Each subsystem is responsible for its own implementation of the Trigger Supervisor, based on the
 1439 functionalities that it wants to have (requirements). The xDAQ [102] is a middleware, developed by
 1440 CERN and widely used at CMS, as a tool for control and monitoring of data acquisition system in

1441 a distributed environment. It is capable of providing a software layer for direct access of hardware
 1442 functionalities and monitoring.

1443 The upgrade made (figure 6.10), consists in upgrade the higher level of the RPC online software.
 1444 In summary, up to 2017, the online software, was using Scientific Linux 6 as operational system,
 1445 which executed xDAQ 12, in turn, servers as backend for Trigger Supervisor 2. A upgrade of
 1446 the operational system to Centos 7, demanded the upgrade to xDAQ 14. On top of that, Trigger
 1447 Supervisor 2 would not work and had to be updated to Trigger Supervisor 5 in order to be functional
 1448 in 2018.

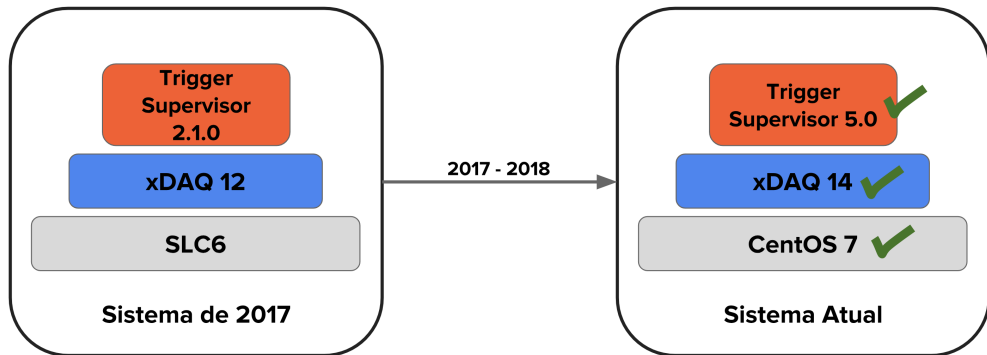


Figure 6.10: Upgrade of the RPC online software.

1449 Between versions 2 and 5 of Trigger Supervisor, part of the source-code had to be reworked, keep
 1450 the majority of the code structures. Most of the changes were made in the front-end of the system.
 1451 The standard JavaScript library Dojo [103], used in version2, was deprecated in favor of Google's
 1452 Polymer[104]. The main reason for this change was to isolate C++ code from HTML, which
 1453 was impossible with Dojo. This implied to rewrite all the screen of the RPC Trigger Supervisor
 1454 implementation, as in figure 6.11.

1455 The upgrade was done in time to ensure the control and operation of the RPC for 2018 data taking.

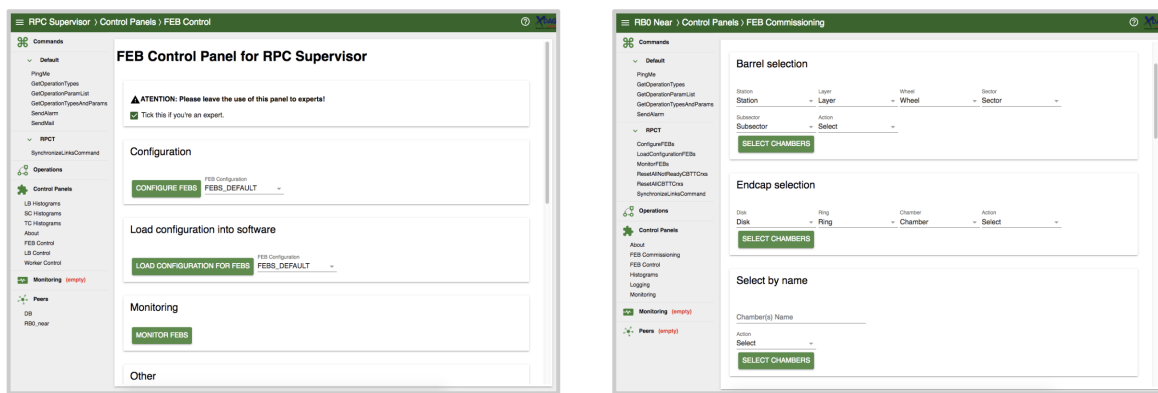


Figure 6.11: Example of the updated screens, using Trigger Supervisor 5.

1456 6.4.1 iRPC R&D

1457 For the next 4 year of CMS activities it is foreseen the upgrade of the the Muon Systems [88].
 1458 These upgrades are planed in order to extend the pseudorapidity coverage (η) and to guarantee the
 1459 operation conditions of the present system in the HL-LHC (High Luminosity LHC) era. The RPC
 1460 (Resistive Plate Chambers) [88] subsystem, it will have maintenance of the present chambers and

1461 installation of new chambers in the region of $|\eta| < 1, 8$ para $|\eta| < 2, 4$ [105]. These new chambers
 1462 (iRPC) will be added in the most internal part of the muon spectrometer, RE3/1 e RE4/1, as in
 1463 Figure 6.12.

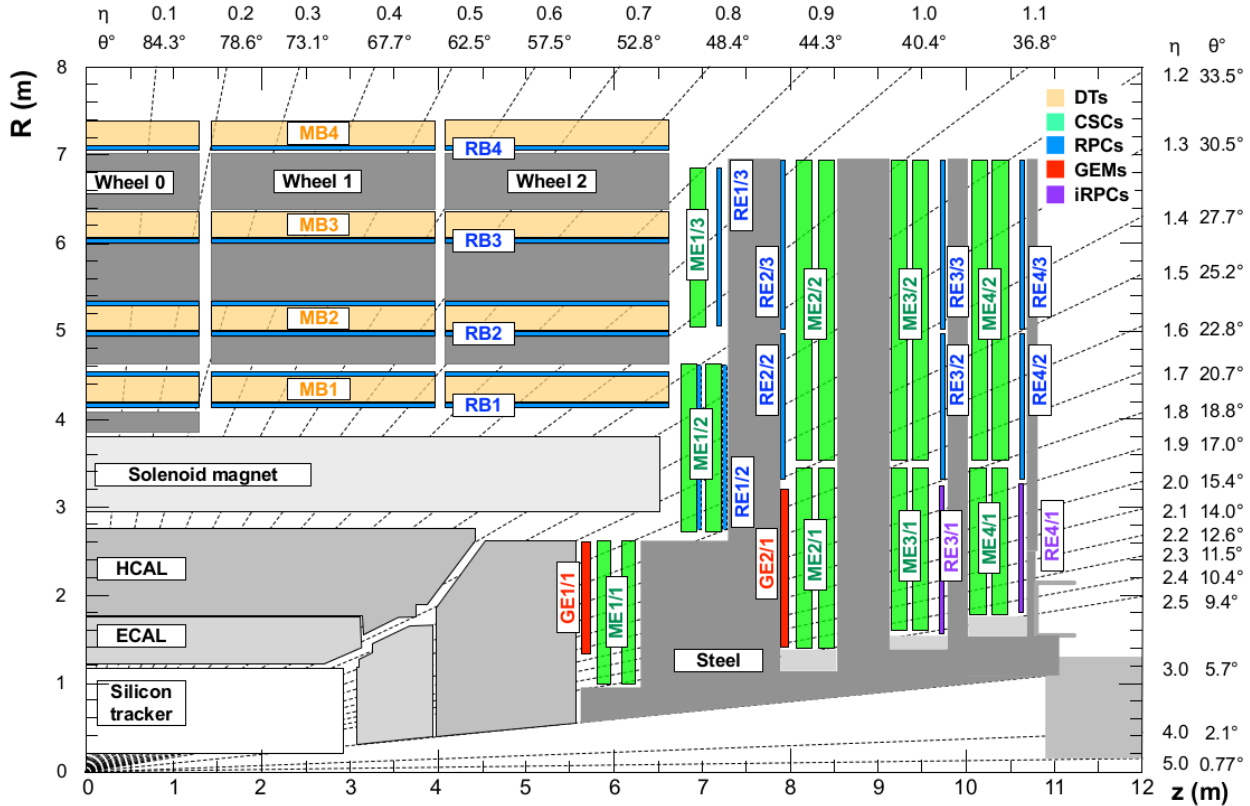


Figure 6.12: η projection of the Muon System subdetectors. In purple, is labeled the iRPCS to be installed during the CMS upgrade.

1464 Even thought this region is covered by the CSC detectors CSC (Cathode Strip Chambers), there
 1465 are some loss of efficiency due the the system geometry. The installation of additional chambers will
 1466 mitigate this problem and potentially increase the global efficiency of the muon system. The new
 1467 chamber, called iRPC (*improved RPC*), will be different them the present one. For a luminosity of
 1468 $5 \times 10^{34} \text{ cm}^{-2} \text{s}^{-1}$ the neutrons, photons, electrons and positrons background in the high $|\eta|$ region
 1469 is expected to be around 700 Hz/cm^2 (for the chambers in RE3-4/1). Applying a safety factor
 1470 of 3, the new chambers should support up to 2 Hz/cm^2 of gamma radiation and still keep more
 1471 than 95% of efficiency. Studies indicate, so far, that the use of High Pressure Laminates (HPL) for
 1472 the double gap chambers is the most suitable choice. In order to reduce the aging and increase the
 1473 rate capability, the electrodes and the gap size should be reduced in comparison with the present
 1474 system.

1475 One of the challenges for the R&D of the iRPC chambers is measuring the their performance in
 1476 a high radiation environment, as the one for HL-LHC. For this, the CMS RPC project uses the
 1477 Gamma Irradiation Facility (GIF++) [106], at CERN. The GIF++ is located at the H4 beam line
 1478 in EHN1 providing high energy charged particle beams (mainly muon beam with momentum up to
 1479 100 GeV/c), combined with a 14 TBq 137-Cesium source. In the GIFF++ it is possible to achieve
 1480 the HL-LHC total dose in a much reasonable amount of time. With the shutdown of LHC, the
 1481 muon beam source is also off and will stay like this for 3 years. This means that the only muon
 1482 sources for studies in GIF++ are cosmic muons.

In order to create a trigger system for iRPC R&D, the usual procedure is to use scintillators, on the top and on the bottom of the chamber. This is effective, but in a high gamma radiation environment, scintillators can be very sensitive which could lead to an undesirable amount of fake triggers which can degrade the measurements. Also, if one wants to covers a large area with scintillators, this can be expensive and they will not provide any means of tracking to measuring not only the global, but also the local chamber performance.

To provide a solution, the CMS RPC got in agreement with the LHCb [107] Muon Project to use their Multiwire Proportional Chambers (MWPC) [108], which were removed from LHCb, to be replaced by new chambers, and use them as trigger and/or tracking system at GIF++. This chambers, by design, have relatively low gamma sensitivity, already have some 1-dimensional resolution ($O(cm)$) and, the biggest advantage, with respect to any other gaseous particle detector option: LHCb has hundreds of vacant chambers. Any other detector would have to be build.

Not going in details of the MWPC technology nor the LHCb chamber construction [109], these chambers have a total active area of $968 \times 200 mm^2$ divided 2 layers (top and bottom) of 24 wire pads ($40 \times 200 mm^2$) composed of around 25 wires/channel, grouped by construction. Each chamber is equipped with 3 FEBs (Front-End Boards) with 16 pads each.

A channel is a logical combination of a top layer (pads) and a bottom layer readout. These readouts can be combined in AND or OR logics. One can have 8 channels per FEB, each channel being a logical combination of top and bottom pads. In this mode they are called AND2 and OR2. It is also possible to have the FEB configured in a 2 channels mode, each one corresponding to one sixth of the total readout pads. In this mode, all the pads can be combined in OR (called OR8) or they can be AND'ed in top and bottom pads and then group in OR (called OR4AND2). Figures 6.13 and 6.14 presents a logical diagram for each readout mode.

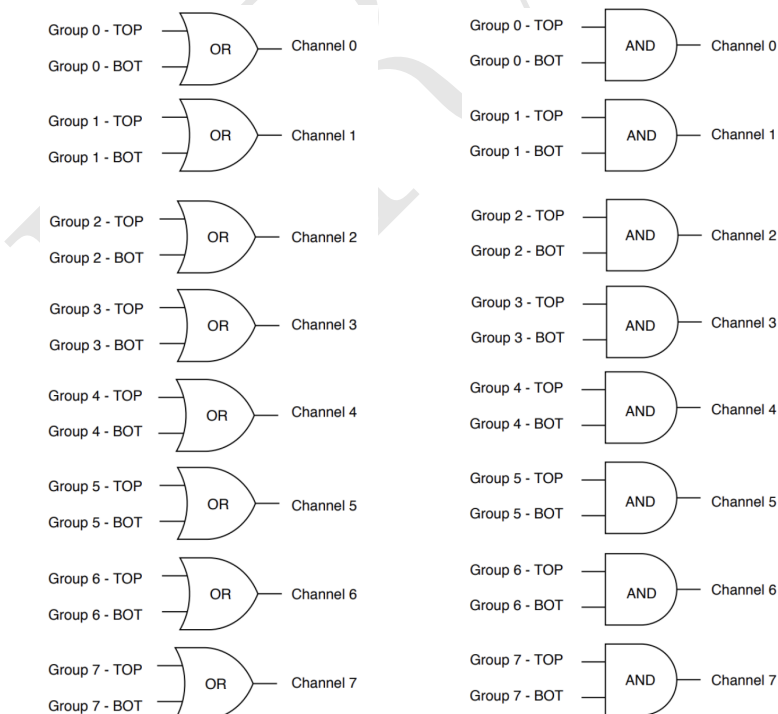


Figure 6.13: FEB configured 8 channels modes. Group should be understood as wire pad. Left: Logical diagram for OR2. Right: Logical diagram for AND2.

The nominal gas mixture for these chambers is Ar/CO₂/CF₄ (40:55:5). For a matter of simplicity, it was used an already available similar gas line in the same building, used by CMS CSC (Cathode

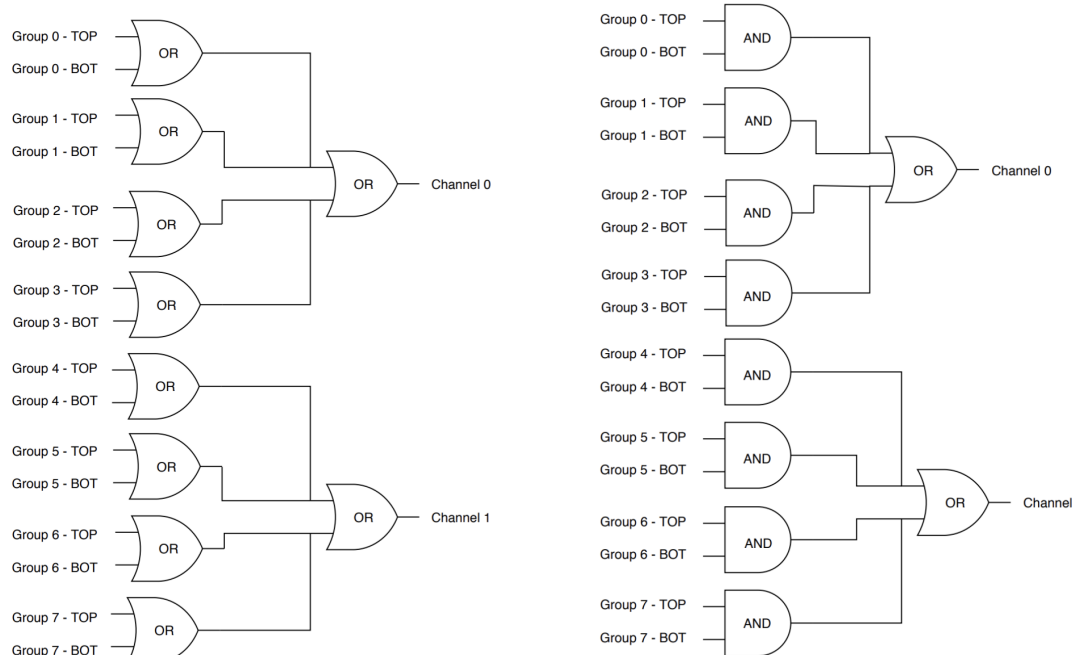


Figure 6.14: FEB configured 2 channels modes. Left: Logical diagram for OR8. Group should be understood as wire pad. Right: Logical diagram for OR4AND2.

1508 Strip Chamber) [88], which has a similar composition (40:50:10). Optimal conditions are obtained
1509 with 2 to 4 liters/hour of gas flux and 2.65 kV of applied voltage.

1510 Figure 6.15 shows the setup that was prepared for commissioning of this chambers. It was mounted
1511 two chambers on top of another (chambers A and B) above an RPC R&D chamber and two other
1512 chambers on the bottom (chambers C and D). These four MWPC will be used as telescope for
1513 the RPC chamber. All the services were mounted in rack, as in Figure 6.15. This includes power
1514 supply (low voltage and high voltage), distribution panel, VME crate and boards for FEB control,
1515 computer for control (high voltage, and FEB control) and NIM crate and boards for LVDS to NIM
1516 signal conversion, logics and counting.

1517 Due to the short amount of time available for the commissioning, only two measurements mea-
1518 surements were made with these chambers. They were meant to be a proof of concept for future
1519 activities.

1520 The first measurement was to measure the coincidence rate of two chambers as a function of the
1521 distance between the two top planes (Figure 6.16). This measurements were done with nominal
1522 working point, with one FEB configured in 2 channels mode with 7 pC threshold, in (160 mm x
1523 160 mm) area per chamber. One can observe that, if we go for a telescope trigger in the order of
1524 1 meter of separation between the chamber, the logical combination chosen has negligible effect in
1525 the coincidence rate. Also, the fits can be used to estimate the rate in a configuration with chamber
1526 on the roof and under the floor. This could be the case of a universal trigger, to be mounted in
1527 GIF++ with these chamber.

1528 The second measurement consist on evaluate the impact of γ background by placing a small Cs-137
1529 source on top of the chamber A (Figure 6.17). For this measurement, the distance between top
1530 planes of each pair of chamber (A to B and C to D) is 65 mm, while the distance between the top
1531 planes of A and C is 570 mm. It is clear the the γ source has an impact on chamber A rate, but
1532 this is negligible when we take into account the coincidence between two chambers.

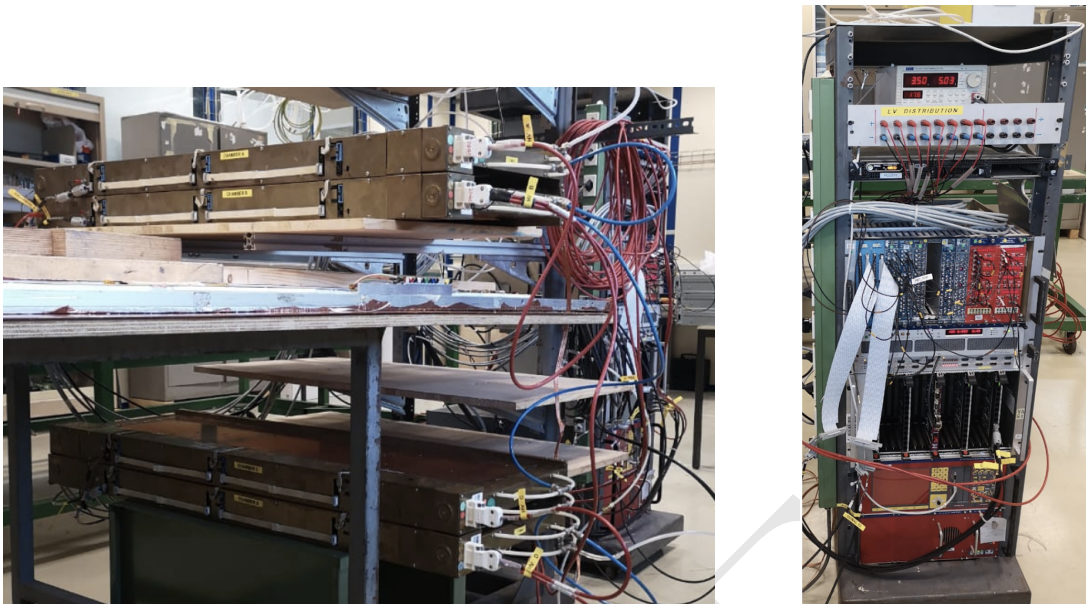


Figure 6.15: Left: Setup mounted for commissioning. Two MWPC chamber on the top (chambers A and B) and two (chambers C and D) on the bottom with a RPC R&D in the middle. Right: Rack with all the services for the operation of these chambers.

1533 This two measurements were enough to validate this chambers as possible trigger pro RPC R&D
 1534 with cosmic muons in the laboratory and at GIF++. The next steps would be use this MWPC
 1535 chamber to implement a tracking system from triggering. This would demand some developments,
 1536 since, due to bandwidth restrictions, the signal from each FEB would have to go to a programmable
 1537 fast electronics, i.e. a FPGA, which would reconstruct muon tracks and provide the trigger to the
 1538 DAQ system. This can be done by placing the two pair of chambers (AB and CD) in orthogonal
 1539 configuration and read the signal in a CAEN V2495 board [110].

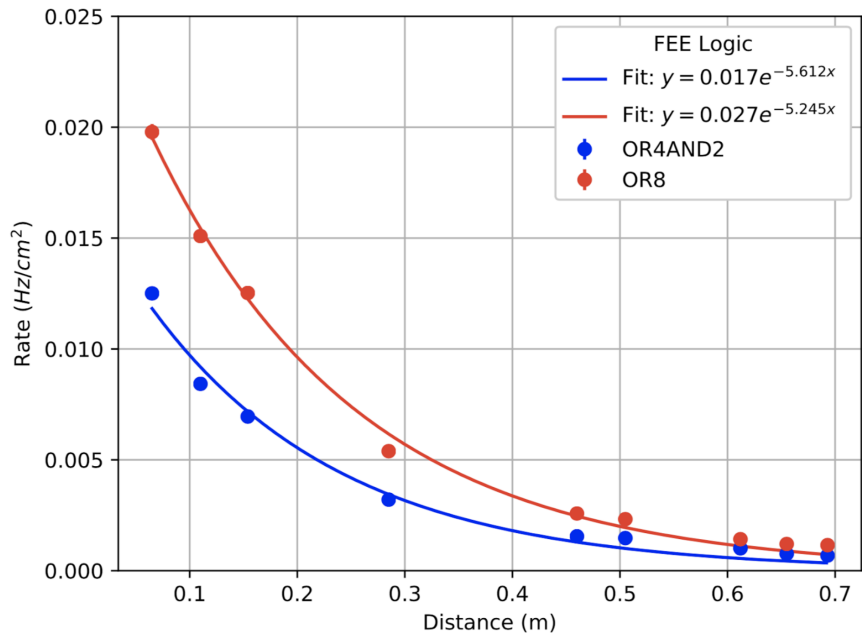


Figure 6.16: Coincidence rate of two chambers with respect to an arbitrary distance between the two top planes. Measured in 10 minutes, for 2 logical combinations (OR8 and OR4AND2). Applied high voltage: 2.65 kV. Threshold: 7 pC. Active area: readout of 160 mm x 160 mm per chamber.

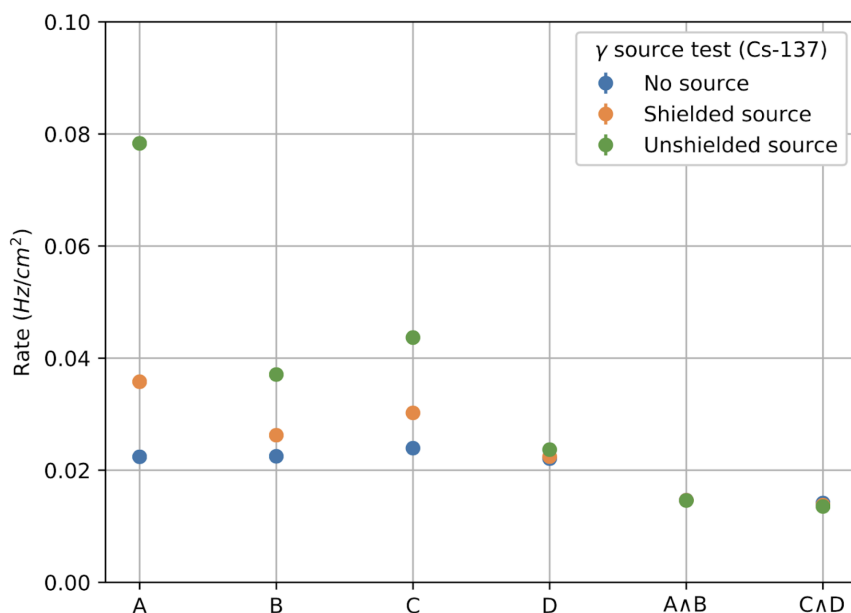


Figure 6.17: Individual rates (chambers A, B, C and D) and coincidence rates for two chambers (A AND B, C AND D), for without γ source (blue), a shielded γ source (orange) and an unshielded γ source (green). Source sitting on top of chamber A. Applied high voltage: 2.65 kV. Threshold: 7 pC. Active area: readout of 160 mm x 320 mm per chamber. Logical combination: AND2

1540 6.4.2 LS2 and the RPC Standard Maintenance

1541 In December 2018, the LS2 (Long Shutdown 2) was started. This a period in which the LHC and
 1542 its detectors (CMS included) stop their operation for maintenance and upgrade. The LS2 will go
 1543 up to 2021, when LHC and CMS restart the data taking with the Run3.

1544 During the LS2 it is being installed services for the new chambers (gas pipes, low voltage (LV), cables,
 1545 signal and control optical fibers, high voltage (HV) cable and support equipment, and HV/LV power
 1546 supplies), as well as continuity to the to the RPC R&D studies, besides the reparation of broken
 1547 elements of the present system, i.e. chamber in the barrel region which present gas leak problems,
 1548 maintenance of the LV and HV connectivity and power system, maintenance of the control system
 1549 of problematic chambers (Front-Ends boards, cabling and Distribution Boards) and the dismount
 1550 and reinstallation of four stations in the endcap (RE4) on both sides of CMS [111].

1551 What concerns the standard maintenance of the present RPC system, the main LS2 activities in
 1552 which the student was involved, can be divided in three main tasks: (a) HV maintenance, (b) LV
 1553 and control maintenance and (c) detector commissioning.

1554 HV maintenance

1555 A key factor of and RPC performance is the applied high voltage (HV). The CMS RPC achieve
 1556 their optimal performance with, around, 9.5 kV applied in each gap. This voltage is in the range
 1557 of the dielectric breakdown of many gases, which could lead to potential current leakages, if some
 1558 part of the system is damaged, poorly operated or badly installed. If the currents are high enough
 1559 this can make impossible the operation of the chamber. In cases like this, during the operation
 1560 period (data taking), the problematic HV channel is identified and turned off (each chamber has
 1561 two channels, one for each layer of gaps). Chambers in this situation are said to be operating in
 1562 single gap mode (SG).

1563 The goal for the HV maintenance is to, now that the CMS is off and the chambers are accessible,
 1564 identify which part of the HV supply system is causing the current leak and fix it the best way
 1565 possible. Usually the problem is beyond the power supply, very often connectors or the gap itself
 1566 are damaged.

1567 The CMS RPCs uses two kind of HV connectors, monopolar and tripolar connector. The monopolar
 1568 are used to connect the chamber to the power supply. If mounted properly, rarely they present
 1569 problems. The connection to the chamber is made by tripolar connectors, in which the ground and
 1570 the HV for both gaps arrives to the chamber in a single connector, for simplicity and to save space in
 1571 the patch panel. Unfortunately these connectors are relatively fragile, and they could be a potential
 1572 source of leak, specially if they were poorly mounted, badly operated or with aging itself. Also,
 1573 since this was a connector made exclusively for the CMS RPC system, some design choices had to
 1574 be improved after the installation of other chamber. Those installed with old batches of tripolar
 1575 connectors are sensitive ones. The reparation of this connectors consists in isolate the connector
 1576 from the chamber and power it up to 15 kV (maximum voltage allowed by the system). If the tested
 1577 connector is broken one will observe a very fast increase in the current of the HV channel. The only
 1578 solution to this kind of problem is to replace the connector.

1579 On the other hand, if the connector is powered isolated and pass the test, the problem beyond
 1580 the connector (assuming that the power system have already been tested), i.e. inside the chamber.
 1581 When a chamber is in SG mode it means that a full layer is off, but not necessarily all the gaps
 1582 in that layer are bad (a RPC can have up to three per layer). In this situation, the procedure
 1583 consists in cutting the cables that comes from the gaps to the chamber side connector one by one
 1584 and identify which gap of the problematic layer is the broken by powering it. Once identified, this

1585 gap should be isolated and the other ones reconnected. The broken gap is unrecoverable, since it is
 1586 inside the chamber, but 5% to 10 % of efficiency can be retaken, without changing the applied HV
 1587 and increasing the longevity of the chamber.

1588 Another contribution to the HV maintenance was the proposal of a procedure to replace the prob-
 1589 lematic tripolar connector by a monopolar (also called jupiter) connector, which are known for being
 1590 much more stable and reliable. The figure 6.18 (left) show the designed adapter for the chamber
 1591 patch panel which would make this change possible. Figure 6.18 (right) shows a tryout of a cham-
 1592 ber in which this procedure was tested. The proposal was presented to the RPC community and
 1593 approved to be used from now on. Technical drawings and instructions were provided.

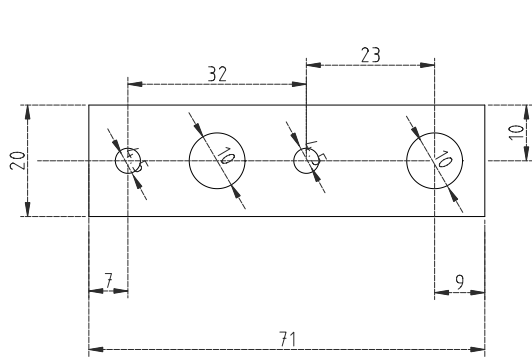


Figure 6.18: Left: Proposed adapter for the chamber patch panel which makes it possible to replace a tripolar by a jupiter HV connector. Right: Tryout of the proposed HV connector replacement.

1594 LV and control maintenance

1595 The low voltage (LV) and control maintenance consists in making sure that the Front-End Boards
 1596 (FEBs) are powered and configurable, which means that the LV power system is working from
 1597 supply board to the cable, that the signal cables are in good state and properly connected to the
 1598 chamber and to the link boards and that the on-detector electronics (FEBs and Distribution Boards
 1599 - DBs) are working fine.

1600 Usually, this system is very reliable. The weak point, in most of the cases, is the detector electronics.
 1601 When a FEB [112] (as in Figure 6.19) is problematic it can present regions of very high noise or no
 1602 signal at all (silent), which can not be recovered by the threshold control. In cases like this, when
 1603 the FEB is accessible, it can be replaced in order to recover efficiency in the problematic chamber.
 1604 This procedure is done by extracting the chamber from inside the detector (only for barrel chamber)
 1605 and opening its cover to have access to the problematic component. Removed boards are sent back
 1606 to production labs for refurbishment.

1607 The most usual problem is a chamber in which the threshold control was lost. For those chambers,
 1608 most probably, the problem is in the distribution board of the chamber, which is a piece of hardware
 1609 responsible for distributing the LV power to the FEBs (3 to 6 per chamber) and sending the threshold
 1610 control signal to the FEBs via I2C line. If a chamber has no threshold control, it means that the
 1611 RPC operation has no control over the signal selection, which can potentially induce performance
 1612 issues.

1613 For the barrel this maintenance happens concomitantly with the gas leak reparations on the barrel
 1614 chamber, since both demands the chamber extraction, which is a complex procedure in terms of
 1615 operation and demands specialized equipment and manpower. For technical reasons, the gas leak
 1616 extractions have precedence over LV ones.

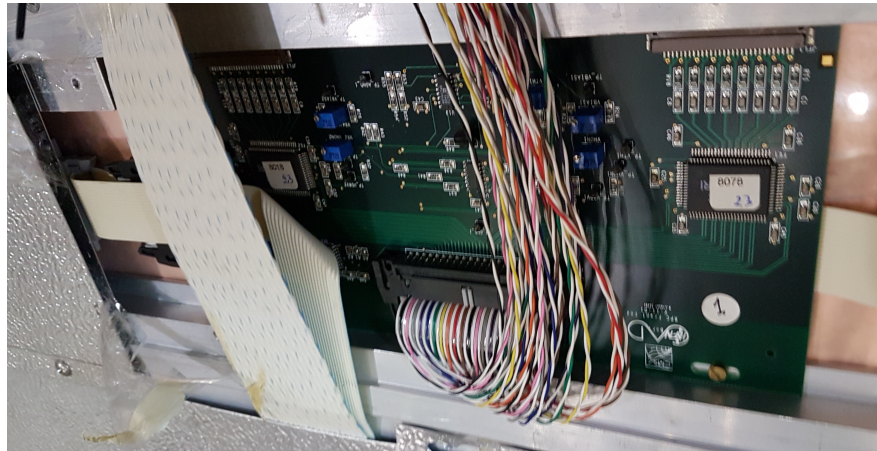


Figure 6.19: RPC Front-end board (FEB) used in the barrel chambers.

1617 Detector commissioning

1618 All the LS2 activities demands uncabling of the chamber to be repaired and possibly some neighbor
 1619 chambers. Also, it can involve the replacement of components of the chamber. To avoid damage to
 1620 the system a compromising procedure is needed after all this activities. Given the responsibilities
 1621 of the commissioning it was necessary to: (a) make sure that the the RPC system keep tracks of all
 1622 the interventions, (b) maintain all the algorithms used in the commissioning procedure, (c) together
 1623 with the RPC Coordination, define a pool of people and a schedule to the commissioning of the
 1624 system and (d) follow-up, with other CMS RPC experts, the availability of materials and resources
 1625 for the commissioning operations.

1626 Besides the organizational tasks, the commissioning demanded to establish procedures to ensure the
 1627 connectivity and functionality of HV and LV connections. For the HV, it is needed to make sure
 1628 that the chambers are properly connected, without miscabling⁴ and that the currents at stand-by
 1629 HV and working point HV are compatible with the ones in the end of last data-taking (end of
 1630 2018). This activity will start in November/2019, when the CMS RPC Standard Gas Mixture will
 1631 be available again.

1632 For the LV point of view, the LV power cable and signal cables should also be properly connected,
 1633 and presenting a noise profile compatible with last data-taking. One key point for this task is to
 1634 make sure that that there are no miscabling of signal cable. One RPC chamber can have from 6
 1635 to 18 signal cable, which are connected very close one to another. There is a good chance that a
 1636 chamber, after reparation, have its signal cables mixed. In order to diagnose situations like this, it
 1637 was validated a algorithm present in the RPC Online Software, but never used since LS1, which,
 1638 by changing the threshold of each component of the RPC system, from very high to very low values
 1639 (component by component), can spot miscabled chambers. Since the control line is independent of
 1640 the signal line, a misclabeled will present a different noise from what is expected.

1641 Besides the validation of this algorithm, it was also implemented a web system (Figure 6.20),
 1642 developed in Flask [113] wich automatize the execution of the algorithm, making transparent to the
 1643 shifter (or the one performing the commissioning) the procedure to get miscabling report.

1644 The LV commissioning is ongoing, since it happens, as much as possible, right after the chamber
 1645 reparation.

⁴Mixed cable connections.

FEB Connectivity Test - Analysis

| Worker | Date (YY-MM-DD) | Time (HH:MM:SS) | Hash | |
|-----------|-----------------|-----------------|-----------|------------------------------|
| RBP2_Far | 2019-06-20 | 23:43:19 | 387534dst | Run Analyzer |
| RBP1_Far | 2019-06-20 | 20:12:20 | 458306dst | Run Analyzer |
| RBP1_Far | 2019-06-20 | 20:04:46 | 336162dst | Run Analyzer |
| RBP1_Near | 2019-06-20 | 19:02:00 | 377863dst | Run Analyzer |
| RBP1_Near | 2019-06-19 | 18:59:00 | 858950dst | Run Analyzer |
| RBP1_Far | 2019-06-19 | 18:58:26 | 994787dst | Run Analyzer |
| YEN3_Far | 2019-05-07 | 10:28:23 | 176278dst | Run Analyzer |
| YEN3_Near | 2019-05-07 | 10:28:08 | 347504dst | Run Analyzer |
| YEN1_Far | 2018-12-07 | 15:03:24 | 575561 | Run Analyzer |
| RBO_Far | 2018-12-07 | 14:45:42 | 101463 | Run Analyzer |
| RBP1_Far | 2018-12-07 | 09:12:00 | 477689 | Run Analyzer |

Figure 6.20: RPC FEB Commissioning Analyzer.

DRAFT

1646 Bibliography

- 1647 [1] Wikimedia Commons. *Standard Model*. 2020. URL: https://en.wikipedia.org/wiki/File:Standard_Model_of_Elementary_Particles.svg.
- 1648 [2] C. Patrignani et al. “Review of Particle Physics”. In: *Chin. Phys.* C40.10 (2016), p. 100001. DOI: 10.1088/1674-1137/40/10/100001.
- 1649 [3] A. Salam and J. C. Ward. “On a gauge theory of elementary interactions”. In: *Il Nuovo Cimento (1955-1965)* 19.1 (1961), pp. 165–170. DOI: 10.1007/BF02812723. URL: <https://doi.org/10.1007/BF02812723>.
- 1650 [4] F. Abe et al. “Observation of top quark production in $\bar{p}p$ collisions”. In: *Phys. Rev. Lett.* 74 (1995), pp. 2626–2631. DOI: 10.1103/PhysRevLett.74.2626. arXiv: hep-ex/9503002.
- 1651 [5] S. Abachi et al. “Observation of the top quark”. In: *Phys. Rev. Lett.* 74 (1995), pp. 2632–2637. DOI: 10.1103/PhysRevLett.74.2632. arXiv: hep-ex/9503003.
- 1652 [6] Serguei Chatrchyan et al. “Observation of a new boson at a mass of 125 GeV with the CMS experiment at the LHC”. In: *Phys. Lett.* B716 (2012), pp. 30–61. DOI: 10.1016/j.physletb.2012.08.021. arXiv: 1207.7235 [hep-ex].
- 1653 [7] G. Aad et al. “Observation of a new particle in the search for the Standard Model Higgs boson with the ATLAS detector at the LHC”. In: *Physics Letters B* 716.1 (2012), pp. 1–29. ISSN: 0370-2693. DOI: <https://doi.org/10.1016/j.physletb.2012.08.020>. URL: <http://www.sciencedirect.com/science/article/pii/S037026931200857X>.
- 1654 [8] CMS Collaboration. *Summary of the cross section measurements of Standard Model processes*. 2020. URL: <https://twiki.cern.ch/twiki/bin/view/CMSPublic/PhysicsResultsCombined> (visited on 08/21/2020).
- 1655 [9] D. de Florian et al. “Handbook of LHC Higgs Cross Sections: 4. Deciphering the Nature of the Higgs Sector”. In: (2016). DOI: 10.23731/CYRM-2017-002. arXiv: 1610.07922 [hep-ph].
- 1656 [10] “Combined Higgs boson production and decay measurements with up to 137 fb⁻¹ of proton-proton collision data at $\sqrt{s} = 13$ TeV”. In: (Jan. 2020).
- 1657 [11] “Measurement of Higgs boson decay to a pair of muons in proton-proton collisions at $\sqrt{s} = 13$ TeV”. In: (July 2020).
- 1658 [12] Geoffrey Bodwin et al. “Higgs boson decays to quarkonia and the $H\bar{c}c$ coupling”. In: *Phys. Rev. D* 88 (5 Sept. 2013), p. 053003. DOI: 10.1103/PhysRevD.88.053003. URL: <https://link.aps.org/doi/10.1103/PhysRevD.88.053003>.
- 1659 [13] Geoffrey T. Bodwin et al. “Relativistic corrections to Higgs boson decays to quarkonia”. In: *Phys. Rev. D* 90 (11 Dec. 2014), p. 113010. DOI: 10.1103/PhysRevD.90.113010. URL: <https://link.aps.org/doi/10.1103/PhysRevD.90.113010>.
- 1660 [14] G. Aad, B. Abbott, et al. “Combined Measurement of the Higgs Boson Mass in pp Collisions at $\sqrt{s} = 7$ and 8 TeV with the ATLAS and CMS Experiments”. In: *Phys. Rev. Lett.* 114 (19 May 2015), p. 191803. DOI: 10.1103/PhysRevLett.114.191803. URL: <https://link.aps.org/doi/10.1103/PhysRevLett.114.191803>.
- 1661 [15] Cédric Delaunay et al. “Enhanced Higgs boson coupling to charm pairs”. In: *Phys. Rev. D* 89 (3 Feb. 2014), p. 033014. DOI: 10.1103/PhysRevD.89.033014. URL: <https://link.aps.org/doi/10.1103/PhysRevD.89.033014>.

- [16] M. A. PÉREZ, G. TAVARES-VELASCO, and J. J. TOSCANO. “NEW PHYSICS EFFECTS IN RARE Z DECAYS”. In: *International Journal of Modern Physics A* 19.02 (2004), pp. 159–178. DOI: 10.1142/S0217751X04017100.
- [17] Grossman, Yuval and König, Matthias and Neubert, Matthias. “Exclusive radiative decays of W and Z bosons in QCD factorization”. In: *Journal of High Energy Physics* 2015.4 (Apr. 2015), p. 101. ISSN: 1029-8479. DOI: 10.1007/JHEP04(2015)101. URL: [https://doi.org/10.1007/JHEP04\(2015\)101](https://doi.org/10.1007/JHEP04(2015)101).
- [18] Geoffrey T. Bodwin et al. “Z-boson decays to a vector quarkonium plus a photon”. In: *Phys. Rev. D* 97 (1 Jan. 2018), p. 016009. DOI: 10.1103/PhysRevD.97.016009. URL: <https://link.aps.org/doi/10.1103/PhysRevD.97.016009>.
- [19] Geoffrey T. Bodwin et al. “Addendum: New approach to the resummation of logarithms in Higgs-boson decays to a vector quarkonium plus a photon [Phys. Rev. D 95, 054018 (2017)]”. In: *Phys. Rev. D* 96 (11 Dec. 2017), p. 116014. DOI: 10.1103/PhysRevD.96.116014. URL: <https://link.aps.org/doi/10.1103/PhysRevD.96.116014>.
- [20] Gino Isidori, Aneesh V. Manohar, and Michael Trott. “Probing the nature of the Higgs-like boson via $h \rightarrow Vf$ decays”. In: *Physics Letters B* 728 (2014), pp. 131–135. ISSN: 0370-2693. DOI: <https://doi.org/10.1016/j.physletb.2013.11.054>. URL: <http://www.sciencedirect.com/science/article/pii/S037026931300960X>.
- [21] Alexander L. Kagan et al. “Exclusive Window onto Higgs Yukawa Couplings”. In: *Phys. Rev. Lett.* 114 (10 Mar. 2015), p. 101802. DOI: 10.1103/PhysRevLett.114.101802. URL: <https://link.aps.org/doi/10.1103/PhysRevLett.114.101802>.
- [22] Dao-Neng Gao. “A note on Higgs decays into Z boson and $J/\psi(\Upsilon)$ ”. In: *Physics Letters B* 737 (2014), pp. 366–368. ISSN: 0370-2693. DOI: <https://doi.org/10.1016/j.physletb.2014.09.019>. URL: <http://www.sciencedirect.com/science/article/pii/S0370269314006698>.
- [23] A. M. Sirunyan et al. “Observation of Higgs Boson Decay to Bottom Quarks”. In: *Phys. Rev. Lett.* 121 (12 Sept. 2018), p. 121801. DOI: 10.1103/PhysRevLett.121.121801. URL: <https://link.aps.org/doi/10.1103/PhysRevLett.121.121801>.
- [24] G Apolinari et al. *High-Luminosity Large Hadron Collider (HL-LHC): Preliminary Design Report*. CERN Yellow Reports: Monographs. Geneva: CERN, 2015. DOI: 10.5170/CERN-2015-005. URL: <https://cds.cern.ch/record/2116337>.
- [25] The ATLAS Collaboration et al. “The ATLAS Experiment at the CERN Large Hadron Collider”. In: *Journal of Instrumentation* 3.08 (Aug. 2008), S08003–S08003. DOI: 10.1088/1748-0221/3/08/s08003. URL: <https://doi.org/10.1088%2F1748-0221%2F3%2F08%2Fs08003>.
- [26] G. Aad et al. “Search for Higgs and Z Boson Decays to $J/\psi\gamma$ and $\Upsilon(nS)\gamma$ with the ATLAS Detector”. In: *Phys. Rev. Lett.* 114 (12 Mar. 2015), p. 121801. DOI: 10.1103/PhysRevLett.114.121801. URL: <https://link.aps.org/doi/10.1103/PhysRevLett.114.121801>.
- [27] Morad Aaboud et al. “Searches for exclusive Higgs and Z boson decays into $J/\psi\gamma$, $\psi(2S)\gamma$, and $\Upsilon(nS)\gamma$ at $\sqrt{s} = 13$ TeV with the ATLAS detector”. In: *Phys. Lett. B* 786 (2018), pp. 134–155. DOI: 10.1016/j.physletb.2018.09.024. arXiv: 1807.00802 [hep-ex].
- [28] S. Chatrchyan et al. “The CMS experiment at the CERN LHC”. In: *JINST* 3 (2008), S08004. DOI: 10.1088/1748-0221/3/08/S08004.
- [29] Albert M Sirunyan et al. “Search for rare decays of Z and Higgs bosons to J/ψ and a photon in proton-proton collisions at $\sqrt{s} = 13$ TeV”. In: *Eur. Phys. J.* C79.2 (2019), p. 94. DOI: 10.1140/epjc/s10052-019-6562-5. arXiv: 1810.10056 [hep-ex].
- [30] Albert M Sirunyan et al. “Search for Higgs and Z boson decays to J/ψ or Υ pairs in proton-proton collisions at $\sqrt{s} = 13$ TeV”. In: *Phys. Lett. B* 797.arXiv:1905.10408. CMS-HIG-18-025-003 (May 2019). All figures and tables can be found at <http://cms-results.web.cern.ch/cms-results/public-results/publications/HIG-18-025> (CMS Public Pages), 134811. 31 p. DOI: 10.1016/j.physletb.2019.134811. URL: <https://cds.cern.ch/record/2676242>.

- [31] Albert M. Sirunyan et al. “Observation of the $Z \rightarrow \psi\ell^+\ell^-$ decay in pp collisions at $\sqrt{s} = 13$ TeV”. In: *Phys. Rev. Lett.* 121.arXiv:1806.04213. CMS-BPH-16-001-003 (June 2018). Submitted to Phys.Rev.Lett., 141801. 17 p. DOI: 10.1103/PhysRevLett.121.141801. URL: <https://cds.cern.ch/record/2623687>.
- [32] Albert M Sirunyan et al. “Search for decays of the 125 GeV Higgs boson into a Z boson and a ρ or ϕ meson”. In: (July 2020). DOI: 10.3204/PUBDB-2020-02812. arXiv: 2007.05122 [hep-ex].
- [33] S. Chatrchyan et al. “The CMS experiment at the CERN LHC”. In: *JINST* 3 (2008), S08004. DOI: 10.1088/1748-0221/3/08/S08004.
- [34] Serguei Chatrchyan et al. “Description and performance of track and primary-vertex reconstruction with the CMS tracker”. In: *JINST* 9 (2014), P10009. DOI: 10.1088/1748-0221/9/10/P10009. arXiv: 1405.6569 [physics.ins-det].
- [35] Vardan Khachatryan et al. “Performance of electron reconstruction and selection with the CMS detector in proton-proton collisions at $\sqrt{s} = 8$ TeV”. In: *JINST* 10 (2015), P06005. DOI: 10.1088/1748-0221/10/06/P06005. arXiv: 1502.02701 [physics.ins-det].
- [36] Vardan Khachatryan et al. “Performance of photon reconstruction and identification with the CMS detector in proton-proton collisions at $\sqrt{s} = 8$ TeV”. In: *JINST* 10 (2015), P08010. DOI: 10.1088/1748-0221/10/08/P08010. arXiv: 1502.02702 [physics.ins-det].
- [37] A M Sirunyan et al. “Performance of the CMS muon detector and muon reconstruction with proton-proton collisions at $\sqrt{s} = 13$ TeV”. In: *JINST* 13 (2018), P06015. DOI: 10.1088/1748-0221/13/06/P06015. arXiv: 1804.04528 [physics.ins-det].
- [38] Vardan Khachatryan et al. “The CMS trigger system”. In: *JINST* 12 (2017), P01020. DOI: 10.1088/1748-0221/12/01/P01020. arXiv: 1609.02366 [physics.ins-det].
- [39] *CMS Luminosity Measurements for the 2016 Data Taking Period*. Tech. rep. CMS-PAS-LUM-17-001. Geneva: CERN, 2017. URL: <https://cds.cern.ch/record/2257069>.
- [40] S. Agostinelli et al. “GEANT4—a simulation toolkit”. In: A506 (2003), pp. 250–303. DOI: 10.1016/S0168-9002(03)01368-8.
- [41] Paolo Nason. “A New method for combining NLO QCD with shower Monte Carlo algorithms”. In: *JHEP* 11 (2004), p. 040. DOI: 10.1088/1126-6708/2004/11/040. arXiv: hep-ph/0409146 [hep-ph].
- [42] Stefano Frixione, Paolo Nason, and Carlo Oleari. “Matching NLO QCD computations with Parton Shower simulations: the POWHEG method”. In: *JHEP* 11 (2007), p. 070. DOI: 10.1088/1126-6708/2007/11/070. arXiv: 0709.2092 [hep-ph].
- [43] Simone Alioli et al. “A general framework for implementing NLO calculations in shower Monte Carlo programs: the POWHEG BOX”. In: *JHEP* 06 (2010), p. 043. DOI: 10.1007/JHEP06(2010)043. arXiv: 1002.2581 [hep-ph].
- [44] Abdelhak Djouadi. “The anatomy of electroweak symmetry breaking: Tome I: The Higgs boson in the Standard Model”. In: *Physics Reports* 457.1 (2008), pp. 1–216. ISSN: 0370-1573. DOI: <https://doi.org/10.1016/j.physrep.2007.10.004>. URL: <http://www.sciencedirect.com/science/article/pii/S0370157307004334>.
- [45] Torbjörn Sjöstrand, Stephen Mrenna, and Peter Skands. “A brief introduction to PYTHIA 8.1”. In: *Computer Physics Communications* 178.11 (2008), pp. 852–867. ISSN: 0010-4655. DOI: <https://doi.org/10.1016/j.cpc.2008.01.036>. URL: <http://www.sciencedirect.com/science/article/pii/S0010465508000441>.
- [46] Torbjörn Sjöstrand et al. “An Introduction to PYTHIA 8.2”. In: *Comput. Phys. Commun.* 191 (2015), pp. 159–177. DOI: 10.1016/j.cpc.2015.01.024. arXiv: 1410.3012 [hep-ph].
- [47] Vardan Khachatryan et al. “Event generator tunes obtained from underlying event and multiparton scattering measurements”. In: *Eur. Phys. J. C* 76.3 (2016), p. 155. DOI: 10.1140/epjc/s10052-016-3988-x. arXiv: 1512.00815 [hep-ex].

- [48] The NNPDF collaboration et al. “Parton distributions for the LHC run II”. In: *Journal of High Energy Physics* 2015.4 (Apr. 2015), p. 40. ISSN: 1029-8479. DOI: 10.1007/JHEP04(2015)040. URL: [https://doi.org/10.1007/JHEP04\(2015\)040](https://doi.org/10.1007/JHEP04(2015)040).
- [49] J. Alwall et al. “The automated computation of tree-level and next-to-leading order differential cross sections, and their matching to parton shower simulations”. In: *Journal of High Energy Physics* 2014.7 (July 2014), p. 79. ISSN: 1029-8479. DOI: 10.1007/JHEP07(2014)079. URL: [https://doi.org/10.1007/JHEP07\(2014\)079](https://doi.org/10.1007/JHEP07(2014)079).
- [50] Ali Abbasabadi et al. “Radiative Higgs boson decays $H \rightarrow f\bar{f}\gamma$ ”. In: *Phys. Rev. D* 55 (9 May 1997), pp. 5647–5656. DOI: 10.1103/PhysRevD.55.5647. URL: <https://link.aps.org/doi/10.1103/PhysRevD.55.5647>.
- [51] D. de Florian et al. *Handbook of LHC Higgs Cross Sections: 4. Deciphering the Nature of the Higgs Sector*. CERN Yellow Reports: Monographs. 869 pages, 295 figures, 248 tables and 1645 citations. Working Group web page: <https://twiki.cern.ch/twiki/bin/view/LHCPhysics/LHCHXSWG>. Oct. 2016. DOI: 10.23731/CYRM-2017-002. URL: <https://cds.cern.ch/record/2227475>.
- [52] Ye Li and Frank Petriello. “Combining QCD and electroweak corrections to dilepton production in the framework of the FEWZ simulation code”. In: *Phys. Rev. D* 86 (9 Nov. 2012), p. 094034. DOI: 10.1103/PhysRevD.86.094034. URL: <https://link.aps.org/doi/10.1103/PhysRevD.86.094034>.
- [53] John M. Campbell and R.K. Ellis. “MCFM for the Tevatron and the LHC”. In: *Nuclear Physics B - Proceedings Supplements* 205–206 (2010). Loops and Legs in Quantum Field Theory, pp. 10–15. ISSN: 0920-5632. DOI: <https://doi.org/10.1016/j.nuclphysbps.2010.08.011>. URL: <http://www.sciencedirect.com/science/article/pii/S0920563210001945>.
- [54] Vardan Khachatryan et al. “Search for a Higgs boson decaying into $\gamma^*\gamma \rightarrow \ell\ell\gamma$ with low dilepton mass in pp collisions at $\sqrt{s} = 8$ TeV”. In: *Phys. Lett. B* 753 (2016), pp. 341–362. DOI: 10.1016/j.physletb.2015.12.039. arXiv: 1507.03031 [hep-ex].
- [55] N. Brambilla, S. Eidelman, B.K. Heltsley, et al. “Heavy quarkonium: progress, puzzles, and opportunities”. In: *The European Physical Journal C* 71.2 (Feb. 2011), p. 1534. ISSN: 1434-6052. DOI: 10.1140/epjc/s10052-010-1534-9. URL: <https://doi.org/10.1140/epjc/s10052-010-1534-9>.
- [56] Sandro Palestini. “Angular distribution and rotations of frame in vector meson decays into lepton pairs”. In: *Phys. Rev. D* 83 (3 Feb. 2011), p. 031503. DOI: 10.1103/PhysRevD.83.031503. URL: <https://link.aps.org/doi/10.1103/PhysRevD.83.031503>.
- [57] A.M. Sirunyan et al. “Particle-flow reconstruction and global event description with the CMS detector”. In: *Journal of Instrumentation* 12.10 (2017), P10003. URL: <http://stacks.iop.org/1748-0221/12/i=10/a=P10003>.
- [58] Matteo Cacciari, Gavin P. Salam, and Gregory Soyez. “The anti- k_t jet clustering algorithm”. In: *JHEP* 04 (2008), p. 063. DOI: 10.1088/1126-6708/2008/04/063. arXiv: 0802.1189 [hep-ex].
- [59] Matteo Cacciari, Gavin P. Salam, and Gregory Soyez. “FastJet User Manual”. In: *Eur. Phys. J.* C72 (2012), p. 1896. DOI: 10.1140/epjc/s10052-012-1896-2. arXiv: 1111.6097 [hep-ph].
- [60] Albert M Sirunyan et al. “Measurements of properties of the Higgs boson decaying into the four-lepton final state in pp collisions at $\sqrt{s} = 13$ TeV”. In: *JHEP* 11 (2017), p. 047. DOI: 10.1007/JHEP11(2017)047. arXiv: 1706.09936 [hep-ex].
- [61] V. Khachatryan et al. “Observation of the diphoton decay of the Higgs boson and measurement of its properties”. In: *The European Physical Journal C* 74.10 (Oct. 2014), p. 3076. ISSN: 1434-6052. DOI: 10.1140/epjc/s10052-014-3076-z. URL: <https://doi.org/10.1140/epjc/s10052-014-3076-z>.
- [62] S. Bernstein. “Démonstration du théorème de Weierstrass fondée sur le calcul des probabilités”. In: *Commun. Soc. Math. Kharkov* 13.1–2 (1912).

- [63] John Erthal Gaiser. “Charmonium Spectroscopy From Radiative Decays of the J/ψ and ψ'' . PhD thesis. SLAC, 1982. URL: <http://www-public.slac.stanford.edu/sciDoc/docMeta.aspx?slacPubNumber=slac-r-255.html>.
- [64] P. D. Dauncey et al. “Handling uncertainties in background shapes: the discrete profiling method”. In: *JINST* 10.04 (2015), P04015. DOI: 10.1088/1748-0221/10/04/P04015. arXiv: 1408.6865 [physics.data-an].
- [65] S. S. Wilks. “The Large-Sample Distribution of the Likelihood Ratio for Testing Composite Hypotheses”. In: *Ann. Math. Statist.* 9.1 (Mar. 1938), pp. 60–62. DOI: 10.1214/aoms/1177732360. URL: <https://doi.org/10.1214/aoms/1177732360>.
- [66] Higgs to Gamma Gamma Working Group. *Further measurement of $H \rightarrow \gamma\gamma$ at $\sqrt{s} = 13$ TeV*. CMS Note 2016/209. CERN, 2016. URL: http://cms.cern.ch/iCMS/jsp/db_notes/noteInfo.jsp?cmsnoteid=CMS%20AN-2016/209.
- [67] *Updated measurements of Higgs boson production in the diphoton decay channel at $\sqrt{s} = 13$ TeV in pp collisions at CMS*. Tech. rep. CMS-PAS-HIG-16-020. Geneva: CERN, 2016. URL: <http://cds.cern.ch/record/2205275>.
- [68] Jon Butterworth et al. “PDF4LHC recommendations for LHC Run II”. In: *J. Phys.* G43 (2016), p. 023001. DOI: 10.1088/0954-3899/43/2/023001. arXiv: 1510.03865 [hep-ph].
- [69] A. D. Martin et al. “Parton distributions for the LHC”. In: *Eur. Phys. J.* C63 (2009), pp. 189–285. DOI: 10.1140/epjc/s10052-009-1072-5. arXiv: 0901.0002 [hep-ph].
- [70] Hung-Liang Lai et al. “New parton distributions for collider physics”. In: *Phys. Rev.* D82 (2010), p. 074024. DOI: 10.1103/PhysRevD.82.074024. arXiv: 1007.2241 [hep-ph].
- [71] Sergey Alekhin et al. “The PDF4LHC Working Group Interim Report”. In: (2011). arXiv: 1101.0536 [hep-ph].
- [72] Michiel Botje et al. “The PDF4LHC Working Group Interim Recommendations”. In: (2011). arXiv: 1101.0538 [hep-ph].
- [73] Richard D. Ball et al. “Impact of Heavy Quark Masses on Parton Distributions and LHC Phenomenology”. In: *Nucl. Phys.* B849 (2011), pp. 296–363. DOI: 10.1016/j.nuclphysb.2011.03.021. arXiv: 1101.1300 [hep-ph].
- [74] Giampiero Passarino. “Higgs Boson Production and Decay: Dalitz Sector”. In: *Phys. Lett.* B727 (2013), pp. 424–431. DOI: 10.1016/j.physletb.2013.10.052. arXiv: 1308.0422 [hep-ph].
- [75] A.M. Sirunyan et al. “Performance of the CMS muon detector and muon reconstruction with proton-proton collisions at $\sqrt{s}=13$ TeV”. In: *Journal of Instrumentation* 13.06 (June 2018), P06015–P06015. DOI: 10.1088/1748-0221/13/06/p06015. URL: <https://doi.org/10.1088%2F1748-0221%2F13%2F06%2Fp06015>.
- [76] Vardan Khachatryan et al. “Performance of photon reconstruction and identification with the CMS detector in proton-proton collisions at $\sqrt{s} = 8$ TeV”. In: *JINST* 10.CMS-EGM-14-001. CMS-EGM-14-001. CERN-PH-EP-2015-006 (Feb. 2015). Comments: Submitted to JINST, P08010. 59 p. DOI: 10.1088/1748-0221/10/08/P08010. URL: <http://cds.cern.ch/record/1988093>.
- [77] A L Read. “Presentation of search results: the CL_s technique”. In: *Journal of Physics G: Nuclear and Particle Physics* 28.10 (Sept. 2002), pp. 2693–2704. DOI: 10.1088/0954-3899/28/10/313. URL: <https://doi.org/10.1088%2F0954-3899%2F28%2F10%2F313>.
- [78] J. Neyman and E. S. Pearson. “On the Problem of the Most Efficient Tests of Statistical Hypotheses”. In: *Philosophical Transactions of the Royal Society of London. Series A, Containing Papers of a Mathematical or Physical Character* 231 (1933), pp. 289–337. ISSN: 02643952. URL: <http://www.jstor.org/stable/91247>.
- [79] Glen Cowan et al. “Asymptotic formulae for likelihood-based tests of new physics”. In: *The European Physical Journal C* 71.2 (Feb. 2011), p. 1554. ISSN: 1434-6052. DOI: 10.1140/epjc/s10052-011-1554-0. URL: <https://doi.org/10.1140/epjc/s10052-011-1554-0>.

- [80] *Procedure for the LHC Higgs boson search combination in Summer 2011*. Tech. rep. CMS-NOTE-2011-005. ATL-PHYS-PUB-2011-11. Geneva: CERN, Aug. 2011. URL: <https://cds.cern.ch/record/1379837>.
- [81] David H. Annis. “Kendall’s Advanced Theory of Statistics, Vol. 1: Distribution Theory (6th ed.). Alan Stuart and J. Keith Ord; Kendall’s Advanced Theory of Statistics, Vol. 2A: Classical Inference and the Linear Model (6th ed.). Alan Stuart and J. Keith Ord, and Steven F. Arnold”. In: *Journal of the American Statistical Association* 101 (2006), pp. 1721–1721. URL: <https://EconPapers.repec.org/RePEc:bes:jnlasa:v:101:y:2006:p:1721-1721>.
- [82] *Procedure for the LHC Higgs boson search combination in Summer 2011*. Tech. rep. CMS-NOTE-2011-005. ATL-PHYS-PUB-2011-11. Geneva: CERN, Aug. 2011. URL: <https://cds.cern.ch/record/1379837>.
- [83] M. Aaboud et al. “Searches for exclusive Higgs and Z boson decays into $J/\psi\gamma$, $\psi(2S)\gamma$, and $\Upsilon(nS)\gamma$ at $\sqrt{s} = 13\text{TeV}$ with the ATLAS detector”. In: *Physics Letters B* 786 (Nov. 2018), pp. 134–155. ISSN: 0370-2693. DOI: 10.1016/j.physletb.2018.09.024. URL: <http://dx.doi.org/10.1016/j.physletb.2018.09.024>.
- [84] R. Santonico and R. Cardarelli. “Development of resistive plate counters”. In: *Nuclear Instruments and Methods in Physics Research* 187.2 (1981), pp. 377–380. ISSN: 0167-5087. DOI: [https://doi.org/10.1016/0029-554X\(81\)90363-3](https://doi.org/10.1016/0029-554X(81)90363-3). URL: <http://www.sciencedirect.com/science/article/pii/0029554X81903633>.
- [85] Marcello Abbrescia, Paulo Fonte, and Vladimir Peskov. *Resistive gaseous detectors: designs, performance, and perspectives*. Weinheim: Wiley-VCH, 2018. DOI: 10.1002/9783527698691.
- [86] A Beroual and I Fofana. “The background of air gap discharge theory”. In: *Discharge in Long Air Gaps*. 2053–2563. IOP Publishing, 2016, 2-1 to 2-22. ISBN: 978-0-7503-1236-3. DOI: 10.1088/978-0-7503-1236-3ch2. URL: <http://dx.doi.org/10.1088/978-0-7503-1236-3ch2>.
- [87] Leonard B. Loeb and John M. Meek. “The Mechanism of Spark Discharge in Air at Atmospheric Pressure. I”. In: *Journal of Applied Physics* 11.6 (1940), pp. 438–447. DOI: 10.1063/1.1712792. eprint: <https://doi.org/10.1063/1.1712792>. URL: <https://doi.org/10.1063/1.1712792>.
- [88] *The CMS muon project: Technical Design Report*. Technical Design Report CMS. Geneva: CERN, 1997. URL: <https://cds.cern.ch/record/343814>.
- [89] Dong Hyun, Kim. “Work on CMS Muon Detector (RPC) during Long Shutdown 1 (LS1) - Point 5, Cessy, CMS cavern”. CMS Collection. May 2015. URL: <https://cds.cern.ch/record/2016815>.
- [90] P. Bernardini et al. “Precise measurements of drift velocities in helium gas mixtures”. In: *Nuclear Instruments and Methods in Physics Research Section A: Accelerators, Spectrometers, Detectors and Associated Equipment* 355.2 (1995), pp. 428–433. ISSN: 0168-9002. DOI: [https://doi.org/10.1016/0168-9002\(94\)01144-3](https://doi.org/10.1016/0168-9002(94)01144-3). URL: <http://www.sciencedirect.com/science/article/pii/0168900294011443>.
- [91] E. Gorini et al. “Drift velocity measurements in C₂H₂F₄ based mixtures”. In: *Proceedings of the 4th International Workshop on Resistive Plate Chamber and Related Detectors, in Napoli, Italy, 15-16 October* (1997).
- [92] G. Bressi et al. “AN APPARATUS TO SEARCH FOR FREE NEUTRON ANTI-NEUTRON OSCILLATIONS”. In: *Nucl. Instrum. Meth. A* 261 (1987), pp. 449–461. DOI: 10.1016/0168-9002(87)90353-6.
- [93] H.L. Ge et al. “The production of residual nuclides in Pb irradiated by 400 MeV/u carbon ions”. In: *Nucl. Instrum. Meth. B* 337 (2014), pp. 34–38. DOI: 10.1016/j.nimb.2014.07.024.
- [94] M. Abbrescia et al. “A Horizontal muon telescope implemented with resistive plate chambers”. In: *Nucl. Instrum. Meth. A* 336 (1993), pp. 322–329. DOI: 10.1016/0168-9002(93)91116-5.
- [95] L. Antoniazzi et al. “The E771 RPC muon detector”. In: *Nucl. Instrum. Meth. A* 315 (1992), pp. 92–94. DOI: 10.1016/0168-9002(92)90686-X.

- 1937 [96] A. Di Ciaccio et al. “Muon tracking and hadron punchthrough measurements using resistive
1938 plate chambers”. In: *Nucl. Instrum. Meth. A* 315 (1992), pp. 102–108. DOI: 10.1016/0168-
1939 9002(92)90688-Z.
- 1940 [97] R. de Asmundis. “Performances of the RPC trigger system in the L3 experiment”. In: *3rd
1941 International Workshop on Resistive Plate Chambers and Related Detectors (RPC 95)*. 1995,
1942 pp. 139–155.
- 1943 [98] D. Boutigny et al. “BaBar technical design report”. In: (Mar. 1995).
- 1944 [99] Andrea Gelmi. *Longevity studies for the CMS-RPC system*. Tech. rep. CMS-CR-2018-136.
1945 Geneva: CERN, July 2018. URL: <https://cds.cern.ch/record/2634505>.
- 1946 [100] M.A. Shah et al. “Experiences from the RPC data taking during the CMS RUN-2”. In: *15th
1947 Workshop on Resistive Plate Chambers and Related Detectors*. May 2020. arXiv: 2005.12532
1948 [physics.ins-det].
- 1949 [101] *Public CMS Data Quality Information*. twiki.cern.ch/twiki/bin/view/CMSPublic/DataQuality.
1950 Acessado em: 20/02/2018.
- 1951 [102] Johannes Guteleber, Steven Murray, and Luciano Orsini. “Towards a homogeneous archi-
1952 tecture for high-energy physics data acquisition systems”. In: *Computer Physics Commu-
1953 nications* 153.2 (2003), pp. 155–163. ISSN: 0010-4655. DOI: [https://doi.org/10.1016/
1954 S0010-4655\(03\)00161-9](https://doi.org/10.1016/S0010-4655(03)00161-9). URL: [http://www.sciencedirect.com/science/article/pii/
1955 S0010465503001619](http://www.sciencedirect.com/science/article/pii/S0010465503001619).
- 1956 [103] *Dojo*. <https://dojotoolkit.org/>. Acessado em: 20/02/2018.
- 1957 [104] *Polymer Project*. Acessado em: 20/02/2018.
- 1958 [105] M. I. Pedraza-Morales. *RPC upgrade project for CMS Phase II*. 2018. arXiv: 1806.11503
1959 [physics.ins-det].
- 1960 [106] Dorothea Pfeiffer et al. “The radiation field in the Gamma Irradiation Facility GIF++ at
1961 CERN”. In: *Nuclear Instruments and Methods in Physics Research Section A: Accelerators,
1962 Spectrometers, Detectors and Associated Equipment* 866 (2017), pp. 91–103. ISSN: 0168-9002.
1963 DOI: <https://doi.org/10.1016/j.nima.2017.05.045>. URL: <http://www.sciencedirect.com/science/article/pii/S0168900217306113>.
- 1965 [107] A. Augusto Alves Jr. et al. “The LHCb Detector at the LHC”. In: *JINST* 3 (2008), S08005.
1966 DOI: 10.1088/1748-0221/3/08/S08005.
- 1967 [108] Georges Charpak et al. “The Use of Multiwire Proportional Counters to Select and Localize
1968 Charged Particles”. In: *Nucl. Instrum. Meth.* 62 (1968), pp. 262–268. DOI: 10.1016/0029-
1969 554X(68)90371-6.
- 1970 [109] *LHCb Muon Group Home Page*. [Online; accessed 1-October-2019]. 2019. URL: <http://lhcb-muon.web.cern.ch/lhcb-muon/>.
- 1972 [110] *CAEN Programmable Logic Unit - V2495*. [Online; accessed 1-October-2019]. 2019. URL:
1973 <https://www.caen.it/products/v2495/>.
- 1974 [111] *Resistive Plate Chambers are getting dolled up*. <https://cms.cern/news/resistive-plate-chambers-are-getting-dolled>. Acessado em: 20/09/2019.
- 1976 [112] C. Binetti et al. “A new Front-End board for RPC detector of CMS”. In: (Sept. 1999).
- 1977 [113] *Flask (web framework)*. [Online; accessed 1-October-2019]. 2019. URL: <https://palletsprojects.com/p/flask/>.